

Final Report

Reinventing the Wheel

Formula SAE Student Chapter
California Polytechnic State University, San Luis Obispo
2018

Patrick Kragen mv.pkragen@gmail.com
Ahmed Shorab ahmedshorab@gmail.com
Adam Menashe adam1719@gmail.com
Esther Unti estherunti@gmail.com



CONTENTS

Introduction	1
Background – Tire Choice.....	1
Tire Grip	1
Mass and Inertia.....	3
Transient Response	4
Requirements – Tire Choice.....	4
Performance.....	5
Cost.....	5
Operating Temperature	6
Tire Evaluation	7
Lateral Force	7
Hoosier LC0.....	8
18.0x6-10 Hoosier R25B.....	9
13x6 Hoosier R25B.....	9
Avon	9
Longitudinal Force.....	10
Normal Load Sensitivity	11
Relaxation Length	12
Vehicle Integration.....	14
Steering Effort.....	14
CG Height and Overturning.....	15
Aero	15
Kinematics and Packaging.....	15
Camber and Toe Stiffness	15
Conclusion	16
Rim Width	17
Background – Wheel Design.....	20
Composites	20
Relevant Efforts to Produce Carbon Fiber Wheels	20
Ohio State.....	20
Kansas.....	21
Cal Poly	21

TU and Joanneum Graz.....	21
Industry.....	22
Composites Manufacturing.....	23
Requirements – Wheel Design.....	24
Determining Tolerances	25
Structures.....	25
Loads.....	25
Analysis	28
Methodology.....	28
Hub Connection.....	29
Concept Designs.....	29
Detailed Design.....	32
Structural Analysis	34
Final Design.....	36
Wheel Geometry	37
Stiffness Sensitivity	37
Spoke Cross-Section	39
Spoke vs. Plate Analysis.....	41
Spoke Number	43
Barrel Shape.....	43
Number of Pieces	44
Preliminary Geometry Selection Summary.....	46
Composites	47
Detailed Stiffness Analysis	49
Detailed Strength Analysis.....	57
Post Manufacturing Trial Analysis.....	60
Detailed Analysis Summary.....	60
Valve	61
Manufacturing.....	62
Manufacturing Process Selection.....	62
Tooling.....	62
Insert Design.....	66
Post Machining	68

Center Insert Bonding	68
Manufacturing Tests	68
First Manufacturing Test	68
Geometry Changes from First Manufacturing Test.....	73
Cure Cycle and Fiber Wetting	73
Second Manufacturing Test	74
Summary of Geometry Changes.....	82
Wheel Manufacturing	83
Planned Functional and Structural Testing.....	96
Pressure Decay.....	96
Full Wheel Stiffness Test.....	96
Full Wheel Cornering Strength Test.....	97
Vehicle Test.....	98
Tire Mounting.....	98
Contingency Plan.....	99
Conclusion	100
Full Carbon Wheel.....	100
Lugged Architecture	100
Manufacturing.....	102
Appendix A: Dimensioned Drawings	103
Appendix B: Quality Function Deployment	108
Appendix C: Calculations	109
C.1 Load Distribution	109
C.2 Spoke Shape Inertia Script	113
C.3 Plate Analysis MATLAB Script	120
C.4 Spoke Analysis MATLAB Script	122
C.5 Stiffness Matrix Function.....	125
C.6 Camber Deflection Calculation.....	126
C.7 FEA Meshing	127
Appendix D: Manufacturing Trial Photos	128
D.1 First Trial.....	128
D.2 Second Trial.....	132
D.3 Mold Machining.....	135

D.4 Wheel Lamination	137
Appendix E: Works Cited	144

INTRODUCTION

The Formula SAE student design competition is an international collegiate racing class wherein single passenger vehicles compete in dynamic events including autocross, acceleration, skidpad, and endurance racing. *Reinventing the Wheel* selected tires and designed wheels for the 2018 Cal Poly, San Luis Obispo Formula SAE combustion vehicle. Points in dynamic events are awarded based on event times, so the goal of *Reinventing the Wheel* was to improve the vehicle performance at competition through the vehicle's wheels and tires. The main stakeholders in the project were the 2018 and 2019 FSAE teams, responsible for the design and manufacture of both combustion and electric vehicles. More specifically, the suspension was the subsystem most significantly affected by the tire choice and wheel design, but most other subsystems, such as aerodynamics and powertrain, were involved in some way as well. Final wheel manufacturing was unsuccessful, but we hope that future teams can benefit from the research performed and experience gathered by this project and use it to guide future outboard suspension design.

BACKGROUND – TIRE CHOICE

Tires, the most important chassis component, supply the tractive, braking, and cornering forces for maneuvering a vehicle. Tire choice is hugely important in racing and by no means a simple one. Tire performance is a balance of the grip the tire can produce, its transient response to changes in load or direction, and its weight and inertia. Tire choice for the Cal Poly FSAE vehicles must also involve consideration of cost and of the tire in the context of the high-level vehicle design, including drivability, relationship with aero, suspension packaging, etc.

Tire Grip

The tire produces forces where it contacts the ground, as a function of the tire's pressure, temperature, camber angle, slip angle, slip ratio, and normal load.

Below are definitions for a few of the terms mentioned above:

Camber: The angle between the tilted plane of a wheel and the wheel's vertical plane. Positive camber is defined as an outward tilt of the wheel so as the top of the wheel extends farther from the vehicle than the bottom of the wheel. Negative camber is defined as the opposite; the bottom of the wheel extends farther outward than the top. Inclination angle is defined as the opposite of camber.

Slip ratio: The difference, expressed as a fraction, between the surface velocity of the tire and the velocity of the vehicle. A slip ratio greater than zero means that the tire is spinning faster than the vehicle is moving forward -- this implies that there is slipping between tire and the road.

Slip angle: The difference between the direction of the heading of the wheel and the direction of the car's velocity.

Tire contact patch: the portion of the tire in contact with the ground at any given point in time.

Tires are tested to determine their force and moment producing capabilities under different operating conditions. Results from these tests can be plotted to assess and compare the steady-state behavior of tires. One of the most common tire plots, lateral force vs. slip angle, is shown below, taken from *Race Car Vehicle Dynamics*, Milliken and Milliken.

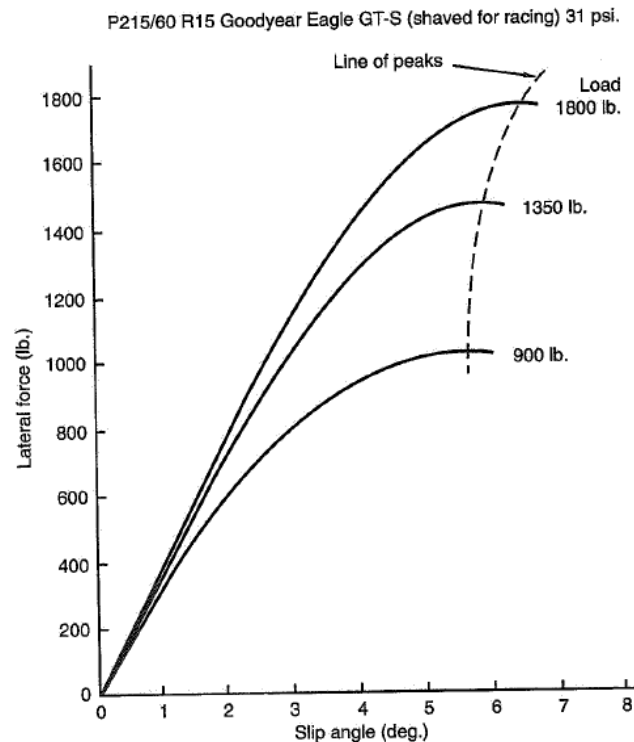


Figure 1 Example lateral force vs. slip angle plot

A higher lateral load capability means that a tire can maneuver around a corner more quickly—all other factors held constant, more grip means faster lap times. The slope of the lateral force vs. slip angle plot, particularly in the linear region at low slip angles, is called cornering stiffness. As the name suggests, the lateral force always acts perpendicular to the tire and is responsible for the vehicle's ability to maneuver around a turn. However, at non-zero slip angles, the tire is not pointed in the same direction as the vehicle's velocity, so the lateral force is not pointing exactly towards the geometric center of the turn. Instead, the effective lateral force on the tire is scaled by the cosine of the slip angle. The lost portion of the lateral force acts as drag on the vehicle. Some forms of racing, like oval track where vehicles spend a significant portion of time going sideways around constant-radius turns, prefer lower cornering stiffness because it allows for a smoother, more forgiving development of grip, so they tolerate the induced drag. The tight autocross tracks that FSAE cars run, on the other hand, favor high cornering stiffness. In turn initiation, the front tires react to a steering input, reach a slip angle, and develop a lateral force. In response, the rear tires require body slip to reach a slip angle and start developing grip. In general, with mass and inertia held constant, a tire with a higher cornering stiffness will require

less body slip and respond faster to a change in direction. Tires also produce longitudinal grip in order to accelerate and brake, although that plot is not shown here.

The lateral force produced by a tire is not evenly distributed across the contact patch. In fact, it is biased slightly rearward, meaning that the resultant lateral force acts slightly behind the centerline of the tire, as shown in Figure 2. This generates an aligning moment about the center axis of the tire which tends to return the tire to straight. This moment resists steering and as a consequence, contributes to the steering effort of the vehicle.

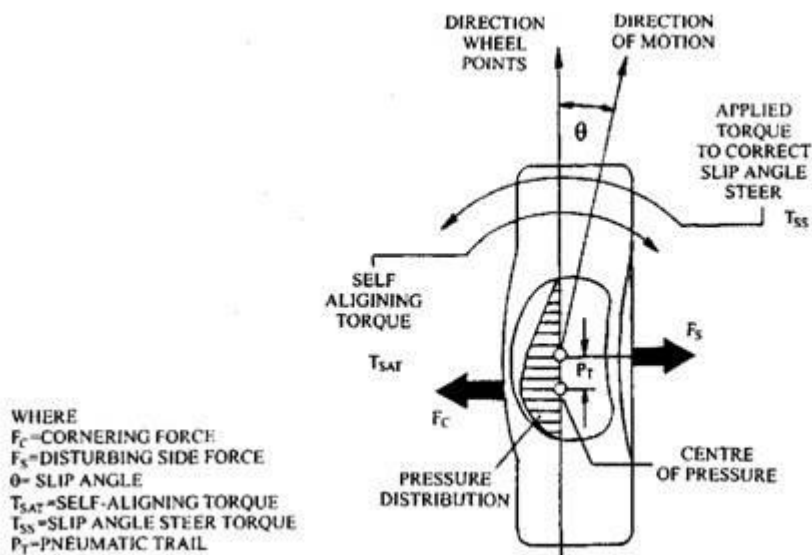


Figure 2. Diagram of a tire's lateral force distribution

Mass and Inertia

Another factor that demands consideration in tire choice are the masses of the tire and wheel themselves. Wheels and tires make up about 16% of the total vehicle mass and are rotating and unsprung mass, which means they contribute even more significantly to the car's inertia (rotational and yaw inertia, primarily) than non-rotating, sprung mass (the bulk of the vehicle mass). It is possible to convert rotating mass into an effective non-rotating mass by equating the kinetic energy of the rotating component to the kinetic energy of an effective non-rotating one and solving for the mass of the latter. For our wheel and tire sizes, the effective non-rotating mass is about 1.3 pounds per pound of wheel and 1.9 pounds per pound of tire¹. Analysis has been performed to find the vehicle's lap time sensitivity to mass, that is, how many seconds faster the car can drive a given track if it's a pound lighter. Results from simulation of the endurance event in both an in-house lap simulator and a model of the CP18C in VI-Grade CarRealTime, suggest that a pound added to the car increases endurance lap time by 21 milliseconds (on a 15-lap event). Assuming they're both mounted on Keizer 4-lug wheels, the

¹ These calculations are given as estimates, but in reality, a smaller wheel/tire should have a smaller scaling factor from rotating to non-rotating mass, since the scaling factor is proportional to the square of the radius. Further calculation could be done to arrive at more accurate numbers.

weight difference between running the Hoosier 20.5x7.0-13 tires (currently on the car) and an average 10" tire, say the Hoosier 18.0x6.0-10, is 20 total pounds across the car². Converted to non-rotating mass, that's 65 milliseconds per endurance lap, assuming all other factors, including grip, are held constant. In reality, smaller tires often produce less force, so analysis of both factors is required to evaluate tire performance.

Transient Response

Tire testing, like that used to make the lateral force vs. slip angle plot above, is generally performed during steady-state operation, meaning that measurements are taken once the tire has settled after a direction or load change. Quasi-static (steady-state) tire analysis is a very good start to choosing a tire and often suffices, especially for oval track racing. However, FSAE races autocross tracks with a significant number of decreasing radius turns, slaloms, and quick direction changes, in which the tires don't fully develop force or transfer weight. As such, consideration of transient tire behavior is warranted. One parameter contributing to its transient response is the tire's relaxation length, the distance over which the tire rolls before the lateral force builds up to 63% of its steady-state value in response to a direction change. Relaxation length can be estimated as $\frac{1}{4}$ - $\frac{1}{3}$ of the tire circumference, or by the cornering stiffness over the lateral stiffness. According to the most basic estimate of relaxation length as a function of only the tire circumference, a smaller diameter tire should, in theory, have a smaller relaxation length and therefore respond more quickly to direction changes. Most of the 10" tires under consideration have an 18.0" diameter, whereas the 13" tires have an outer diameter of 20.5", so the difference in relaxation length between these tires is 11%, a fairly small amount. The Round 6 tire data provided by the FSAE Tire Test Consortium contains transient test results, from which relaxation length were calculated more definitively.

REQUIREMENTS – TIRE CHOICE

Table 1 shows the engineering specifications of the tire choice for *Reinventing the Wheel*.

The foremost objective of the tire choice is to choose the quickest tires for the Cal Poly vehicle in the FSAE competition. The parameters contributing to this goal were initially studied using Quality Function Deployment (QFD), the chart for which can be found in Appendix A. However, it was determined that rating the importance of these parameters on a scale of 1-5 did not accurately represent the vehicle's sensitivity to each parameter, so the QFD did not prove to be a useful tool in setting requirements beyond familiarizing the team with the problem.

² This number assumes a 10" and 13" Keizer wheels, weighing 4.5 lbs and 7.5 lbs, respectively. Uprights would have to get smaller for a 10" wheel, but even a 15% decrease in upright weight is only about 1 pound per car, so it's negligible compared to the wheel and tire weight difference.

Table 1. Engineering requirements for tire choice

Spec #	Parameter	Requirement/Target	Tolerance	Risk	Compliance
1	Performance	Higher overall dynamic performance than baseline tire	Min	H	A,S,T
2	Cost	\$3000, total yearly cost to team	Max	M	A, I
3	Cost-normalized Performance Improvement	0.1 seconds of endurance per dollar	Min	M	A, S, T
4	Temperature Operating Range Maximum*	140 °F	Min	H	A, S, T

* Meaning that maximum operating temperature must be at least this hot.

The tires under consideration, along with relevant specifications, are listed in Table 2.

Performance

As discussed in the background section, tire choice is a balance between grip, mass, and transient response. Since these parameters are interrelated and often at odds with one another, it is difficult to establish a set of requirements for tire attributes. For example, the quickest tire may not be the lightest because the lighter tire may have less grip. We can, however, set a broad performance requirement for the tire: the tire we choose must perform at least as well as the tire the team currently runs. This baseline tire option, the 13x7 Hoosier R25B, is the easiest for the team to design for, as it requires no change in vehicle platform and minimal changes to suspension kinematics. It is also the cheapest option -- the team already has old tires that can be run during shakedown testing at the beginning of the season, as well as rain tires that don't need to be purchased on a yearly basis if used minimally. Accordingly, there's no reason to consider tires with lower performance than the baseline. Beyond this base requirement, the quickest tire was chosen, with consideration of cost, availability, packaging, etc.

Cost

The 2018 team's maximum budget for tires is \$3000. However, more expensive tires may be purchased if sponsorships are acquired. It is worth noting that purchasing cheaper tires means that the team can purchase more tires. Since tire wear can drastically decrease performance, we may find that a tire that makes slightly less grip but is significantly cheaper is preferred as it allows the team to purchase more sets. Similarly, a softer tire with a shorter life is effectively more expensive than a longer life tire, since more sets of the softer tire must be purchased.

Since the team does not have a very flexible budget, we need a way to decide the minimum performance improvement required for the expenditure to be worthwhile. Based on the team's current financial situation, it seems reasonable to expect an improvement of at least 4 places in endurance per \$1000 of new tires. From analysis of the 2016 FSAE Lincoln IC endurance scores, 4 places corresponds to about 100 seconds off endurance (for the teams that finished). Accordingly, the requirement is established that the tire choice must result in a performance increase of at least 0.1 seconds per dollar spent on new tires.

Table 2. Tires under consideration

Tire	Size	Tread Width (in)	OD (in)	Approx. Weight (lb)	Rotational Inertia ⁴ (lb*in ²)	Anticipated Car Weight Loss ¹ (lb)	Operating Temp. (°F)	Cost Per Tire ²	Total Cost ³
13 Hoosier R25B	20.5 x 7.0-13	7.0	20.5	11.0	1,156	0	90-140	\$132.00	\$2,112.00
13 Hoosier R25B	20.5 x 6.0-13	6.0	21.0	11.0	1,213	0	90-140	\$132.00	\$3,168.00
10 Hoosier R25B	18.0 x 6.0-10	6.2	18.0	9.0	729	16	90-140	\$103.80	\$2,491.20
10 Hoosier R25B	18.0 x 7.5-10	7.5	18.3	10.0	837	12	90-140	\$114.60	\$2,750.40
10 Hoosier LC0	6.0/18.0-10	6.0	18.0	8.0	648	20	70-120	\$103.80	\$2,491.20
13 Continental C16	205/470 R13	8.0	18.5	8.3	708	11	~150	\$117.00	\$2,808.00
13 Goodyear D2704	20.0x7.0-13.	6.9	20.4	8.8	916	9	-	\$136.25	\$3,270.00
10 Avon A92	7.0/16.0-10	6.0	16.0	7.7	493	21	-	\$225.00	\$5,400.00
13 Avon A92	6.2/20.0-13	6.2	20.0	11.5	1,146	-2	-	\$122.00	\$2,928.00

[1] Weight reduction based on our weight estimates for 10" and 13" wheels. Baseline is the Hoosier R25B 13x7.0 on the predicted wheels.

[2] Price to team listed. Hoosier tires have the 25% Gerhardt discount applied.

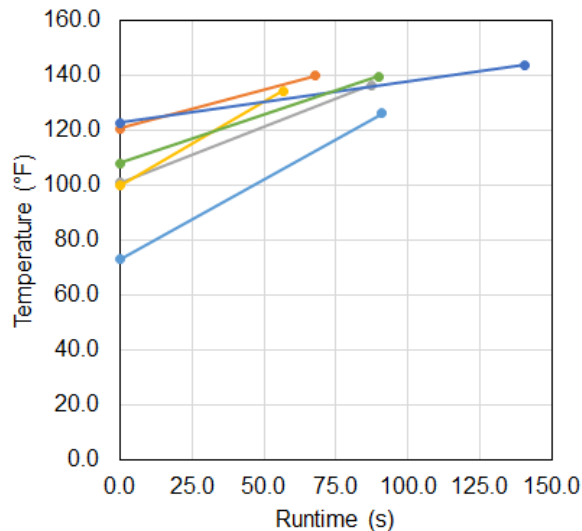
[3] Includes 4 sets for the team's current tire and 6 sets for the others.

[4] Calculated using cylinder of diameter equal to tire diameter. Not a perfect estimate because of the tire sidewall, but serves as a decent comparison.

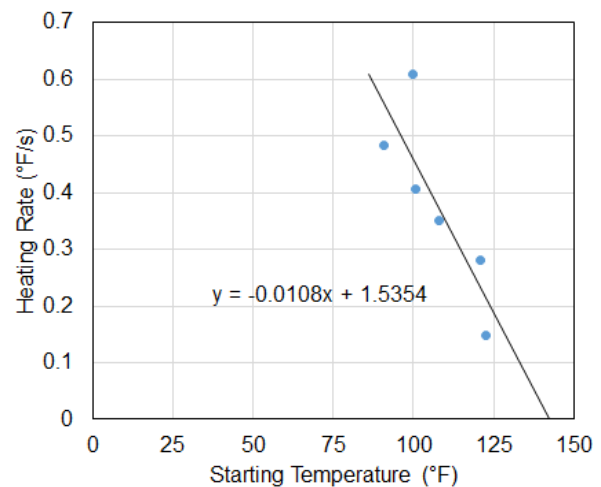
Operating Temperature

In general, tires perform better when hotter, up to a certain point at which they lose traction and wear excessively. Originally it was thought that the team's current tires did not heat up sufficiently during competition events thus were underperforming. However, recent testing on the 2017 FSAE car suggests otherwise. According to a representative of Hoosier tires, the operating temperature of the team's current tires is between 90 and 140 °F. Additionally, the representative claims that there is no difference in tire temperatures or rate of temperature climb between different tire sizes of the same compound, so the 10" R25B tires don't provide a distinct advantage in tire heating over the 13" R25B tires. Track temperatures at the FSAE Lincoln competition are generally at least 110 °F. Pyrometer testing of the tires on the 2017 vehicle has shown that "cold" tires are 10-15 °F cooler than track temperature, which still leaves the current tires within their operating range, even before driving. From recent skidpad testing on a mild day with a track temperature of 100 °F, the average steady-state temperature was estimated as 142 °F, with an average tire temperature of 134 °F after 70 seconds of runtime. A plot of tire temperatures recorded before and after runs can be found in Figure 3a. In Figure 3b, heating rate (the slope of each line in Figure 3a) is plotted against starting temperature in order to estimate steady state temperature (starting temperature at a heating rate of zero). Obviously tire temperature varies with a number of factors (track temperature, ambient temperature, driving course, tire pressure, normal load, and camber, to name a few) but this data is sufficient to show that the current 13" Hoosier tires remaining too cold throughout the competition is not a

major concern. Excessive heating, however, remains a concern in tire choice, justifying the requirement that the maximum operating temperature of the tire must be at least 140 °F. The team's decision regarding which competition to attend in 2018 and future years may affect *Reinventing the Wheel's* tire choice. FSAE Michigan is generally in much cooler weather, potentially justifying a tire compound with a lower operating temperature, such as the Hoosier LC0 compound.



3a. Average tire temperatures vs. runtime



3b. Tire heating rate vs. starting temperature

Figure 3. Tire temperature data from skidpad testing of the CP17C

TIRE EVALUATION

Several requirements for the wheel design, most importantly the diameter, depend on the tire choice, so in order for wheel design to stay on schedule, tire choice must be made quickly. As such, the decision method was to first eliminate tires from the list under consideration by logistics, such as availability and cost, and by inspection of tire plots and basic calculations before performing more advanced analysis.

Lateral Force

Figure 4 is a lateral force vs. slip angle for the tires under consideration for the 2018 FSAE vehicles. The data shown is for a 250 lb normal load and 0° of inclination angle. Most of the tires under consideration are of bias ply construction and perform best with little to no camber, so 0° was selected as a representative way of initially comparing the tires. It is worth noting that the Continental C16 tire, the one radial tire under consideration, performs best at higher inclination angles and will be looked at more closely later on.

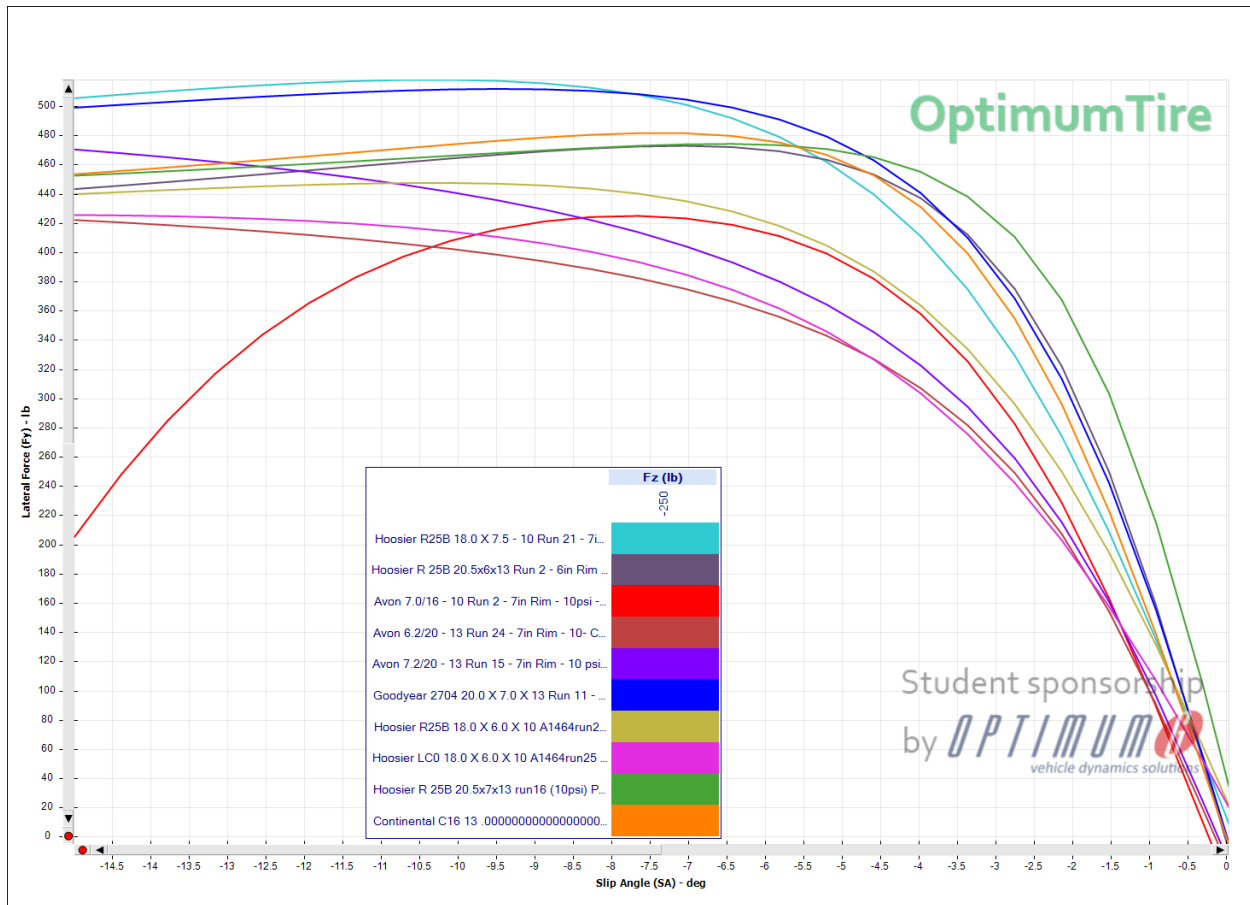


Figure 4. Lateral force vs. slip angle plot for tires under consideration at 250 lb normal load, 10 psi tire pressure, and 0° of inclination angle

Elimination of tires was done by inspection of the tires' lateral behavior, along with a high-level understanding of trends in drivability, response time, grip, and lap times as a function of cornering stiffness, mass, tread width, maximum lateral force, the slip angle at which this occurs, normal load sensitivity.

Hoosier LC0

The 6.0/18.0-10 Hoosier LC0 was eliminated due to its low operating temperature of 70-120 °F. The team has historically competed in the FSAE Lincoln competition, where track and ambient temperatures are hot enough to likely overheat the LC0 compound. If the team decides before *Reinventing the Wheel's* mid-July PDR that the combustion car will compete in FSAE Michigan in 2018 and future years, the LC0 compound may be reconsidered. In this case, it may be worth choosing a 10" diameter wheel in order to platform the electric and combustion vehicles structurally, while allowing the combustion car to run the lower-temperature LC0 tire while the electric car runs the higher-temperature R25B in order to compete in FSAE Lincoln. Regardless, the LC0 tires don't make very much grip and have a cornering stiffness less than nearly every other tire under consideration. While the LC0s are lightweight, the 18.0 x 6.0-10 Hoosier R25B tire is only a pound heavier and make significantly more grip and at a lower slip angle, making it the better low-mass tire option to evaluate.

18.0x6-10 Hoosier R25B

Like the LC0, the R25B 18.0x6-10 is a low cornering stiffness, low grip tire. While it is light -- only 9 lbs -- it is sufficiently low grip to be not worth considering since there is a comparably small tire, the 10 lb 18x7.5-10, that makes 18% more lateral force.

13x6 Hoosier R25B

Driver feedback from brief testing of the 20.5 x 6.0-13 Hoosier R25B tires on the electric car this year indicated that these tires are significantly limited in grip, compared to the with the 7" wide tires later run on the car. The lateral force plot shows a similar trend -- for relatively similar mass, the 6" wide tires have sufficiently lower grip than the 7" ones to not be worth consideration. While they are thinner and therefore carry less rotational inertia, they also have lower cornering stiffness, which tends to suggest overall slower response time, especially of the rear tires which take time to catch up to the fronts after a steering input.

Avon

The 13" Avon tires are heavier than the current Hoosier tires on the car, make significantly less grip, and make max grip at a higher slip angle. The 10" Avon tires make less grip than the LC0s for a similar weight and also exhibit a fairly sharp drop-off in grip at high slip angles, suggesting they'd be difficult to drive. This particular lateral force plot is deceiving because the Avon tires are only tested up to about 10° of slip, but there is in fact somewhat of a drop-off in lateral force around 8-10° of slip visible in the raw data. Just as the LC0s were eliminated for insufficient grip and cornering stiffness, so too will the Avon tires.

The tires remaining to be evaluated are the Continental C16s, the Goodyear D2704s, the 10"x7.5" Hoosier RR25Bs, and the 13"x7" R25B Hoosiers currently on the car. It's worth noting that Continental only provides tires to one FSAE team in the US each year. We have not been selected this year, but we will briefly consider the tire nonetheless in the event that Cal Poly FSAE becomes eligible for these tires in the future. Similarly, the Goodyears are well outside our budget but will continue to appear in plots for reference and to evaluate whether these tires are worth purchasing if the team expands its budget or develops a partnership with Goodyear at a later date.

Figure 5 contains a lateral force vs. slip angle plot for these four tires at 0° and 3° of inclination at a 100 and 250 lb normal load. It is clear from this plot that the Hoosier 10x7.5" tires are a bit of an anomaly. They're a smaller diameter tire than the Hoosier 13 currently on the car (18.0 vs. 20.5 inches) but are capable of significantly higher force, at least at slip angles above 5 degrees. As was discussed earlier, part of the lateral force gets lost to drag on the vehicle at high slip angles. This effect is not shown in Figure 5 but is considered in the lateral acceleration calculations in Table 3.

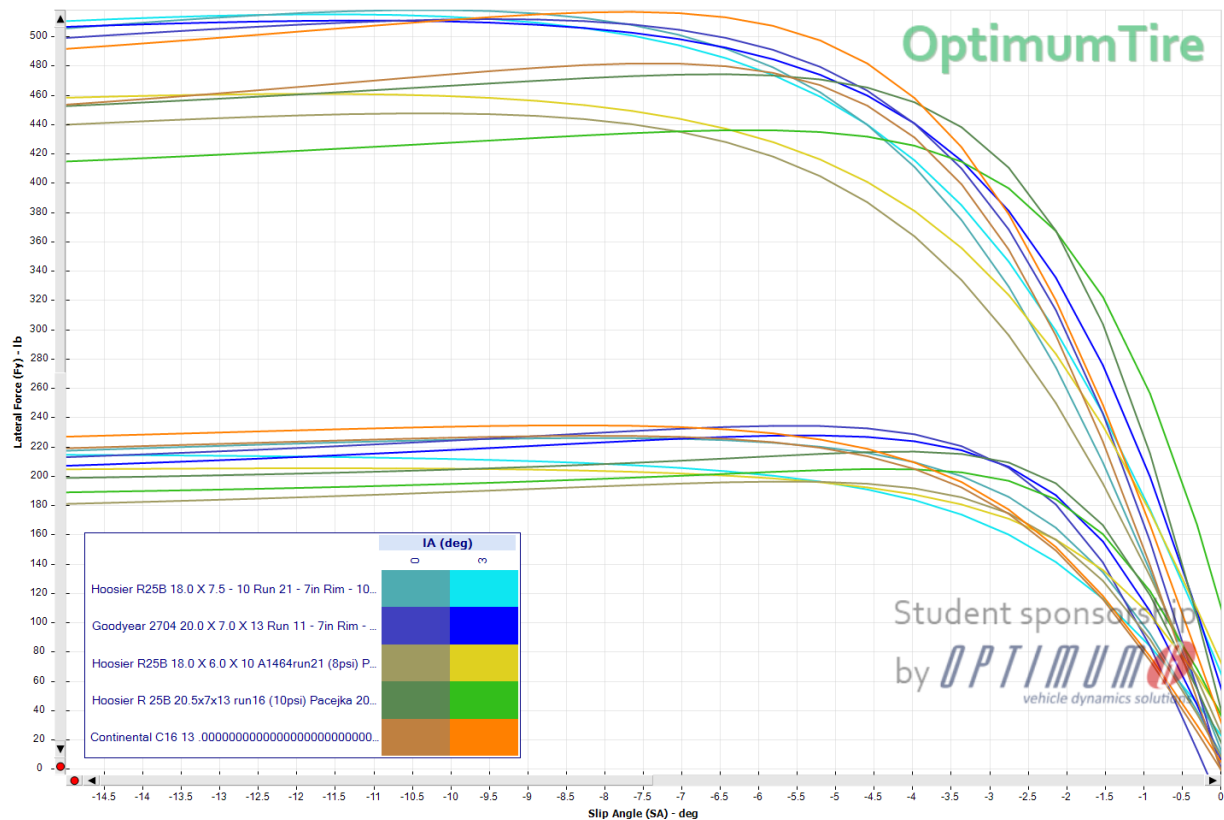


Figure 5. Lateral force vs. slip angle for the four remaining tires under consideration. Data at 250 and 150 lb normal load, 0° and 3° of inclination, and 10 psi of tire pressure

Longitudinal Force

Figure 6 shows a longitudinal force vs. slip ratio plot for three of the remaining tires under consideration. While the Hoosier 13s reach peak force at a lower slip ratio, at high slip ratios, the Hoosier 10s produce about 15% more force than the 13s. The 2018 combustion car is power-limited in most gears, so the extra force capability provided by the 10 may not have a major impact on positive longitudinal acceleration but could be expected to improve braking ability. Additionally, since the Reinventing the Wheel tire and wheel package will be eventually brought to the electric car, a tire with more longitudinal acceleration capability is further justified, as it would if the team switched to a more powerful engine in coming years.

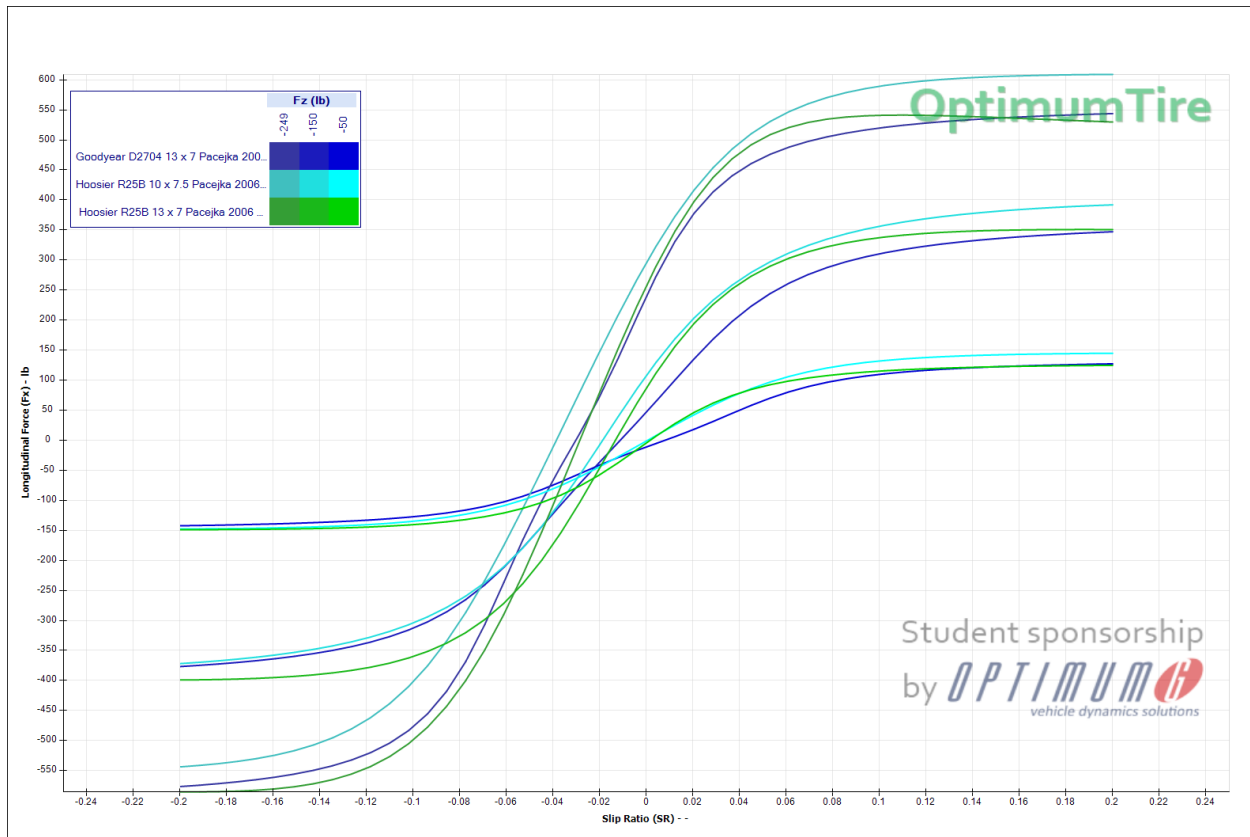


Figure 6. Lateral force vs. slip angle for the four remaining tires under consideration. Data at 250, 150, and 50 lb normal load, 0° of inclination, and 10 psi of tire pressure

Table 3 is a summary of acceleration capabilities of each tire, assuming the same set of matching specifications based on the CP18C preliminary design. It is clear that the differences in acceleration capability between these three tires are minimal.

Table 3. Lateral and longitudinal acceleration capabilities as compared to the baseline tire

Tire	Size	Predicted Max Vehicle Lat Acceleration (G)	Percent Increase Over Baseline (%)	Predicted Max Vehicle Long Acceleration (G)	Percent Increase Over Baseline (%)
13 Hoosier R25B	20.5 x 7.0-13	2.36	0%	1.85	0%
10 Hoosier R25B	18.0 x 7.5-10	2.40	1%	2.08	12%
13 Goodyear D2704	20.0x7.0-13.	2.60	8%	1.85	0%

Normal Load Sensitivity

The coefficient of friction of a tire, lateral or longitudinal, is defined as the force produced by the tire at a certain normal load divided by the magnitude of the normal load on the tire. The mechanics of how tires produce grip are highly complicated and rely on both pure friction and

adhesion. One result of this is that these coefficients of friction are not constant -- they depend on a variety of tire parameters, including normal load itself. The coefficients of friction are generally inversely proportional to normal load, so while loading a tire more always results in more traction, it does so by incrementally smaller amounts as force increases. This means that a set of tires is more effective when evenly loaded. However, different tires have different normal load sensitivity -- that is, the penalty for uneven loading is more for some tires than others. In general, less normal load sensitivity is better. Normal load sensitivity is a particular concern for heavy vehicles or vehicles producing high amounts of aerodynamic downforce. When a vehicle accelerates, in cornering, braking, or forwards acceleration, normal load is transferred to the set of tires opposite the direction of acceleration (i.e. the outside tires on a turn), in addition to the static load on the tire due to the car's weight and aerodynamic downforce. This weight transfer means an uneven loading of tires, so tires that can better handle uneven loading will be able to accelerate faster. Figure 7 is a normal load sensitivity plot of lateral force vs. normal load for all tires originally considered for zero degrees of inclination angle and 10 degrees of slip angle.

Of the four highest performing tires, the Hoosier R25B 10x7.5 is the least sensitive to normal load. However, the Goodyear has a higher lateral coefficient of friction throughout the entire range of normal loads shown, so it is technically the better cornering tire at this slip angle. Similarly, between the two Hoosier R25B tires still under consideration, the 10" tire is the better one through this range. The CP18C is a mid- to high-weight car for Formula SAE, but even for a conservative 400 lb weight estimate, planning to make around 100 lb of downforce, we can expect to see about 350 lbs of normal load on the outside tire. This load is not shown in Figure 7, but even at a 250 lb normal load, the Hoosier 10" tire has a 6% higher coefficient of lateral friction than the Hoosier 13".

Relaxation Length

Using the basic estimate of relaxation length being roughly a tire's diameter, it is expected that the smaller of the two Hoosier tires have the smaller relaxation length. However, as the 10" Hoosier has a lower cornering stiffness, the estimate of relaxation length as cornering stiffness over lateral stiffness indicates otherwise. Figure 8 shows two lateral force vs. time traces each for the Hoosier 10s and 13s from the Round 6 TTC transient test. These were used to calculate the relaxation length numbers shown in Table 4. Only a few transient tests were run for each tire and the test data was relatively noisy, so it's difficult to say conclusively which tire has a truly shorter relaxation length. Defining the times of zero lateral force and full lateral force had a great impact on the calculated relaxation length and data could not be averaged over more than two samples. It is clear, at the very least, that the two Hoosier R25B tires are similarly responsive.

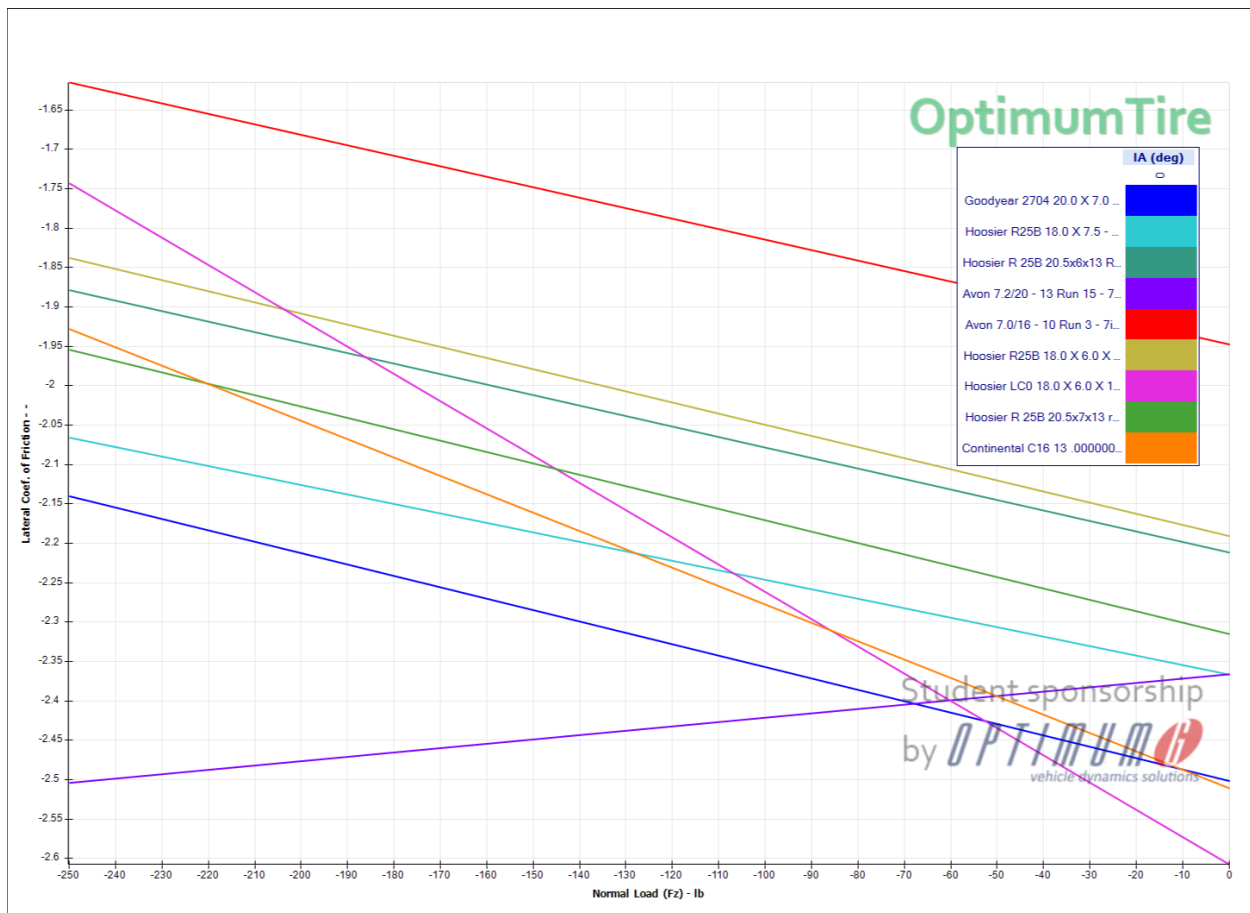


Figure 7. Normal load sensitivity plot for all tires under consideration

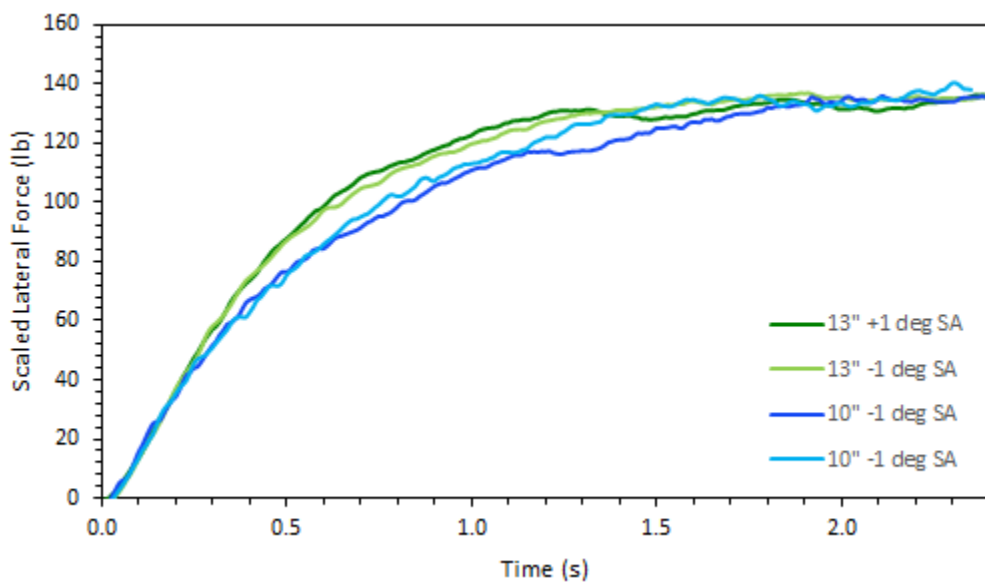


Figure 8. Lateral force vs. time for transient test of Hoosier R25B 10x7.5 and 13x7.

Table 4. Calculated relaxation lengths from lateral force vs. time traces

Tire	Time to 60% of Max Fy (s)	Relaxation length (in)
13 Hoosier R25B	0.55	19.4
10 Hoosier R25B	0.56	19.5

Vehicle Integration

Steering Effort

Figure 9 is a plot of aligning moment vs. slip angle for the Hoosier 10" and 13" tires. As discussed previously, a tire's aligning moment affects the car's steering feel and overall steering effort. Comparing the Hoosier 10s to the car's current tires, it is clear that the peak aligning moments are fairly similar. As a note, the Hoosier 10s are tested only up to 250 lbs of normal load, so the last curve (for $F_z = 350$ lbs) may not be accurate. The 10" tire is less normal load sensitive than the 13" tires (at the rim widths shown), so it is expected that aligning moment should increase less with normal load than the 13s. The peak aligning moment on the 10s occurs at a larger slip angle than the 13s and drops off more slowly, which is to be expected since the lateral force follows the same behavior. Overall, the two tires should have similar maximum steering efforts and their steering feel should be representative of the car's lateral behavior.

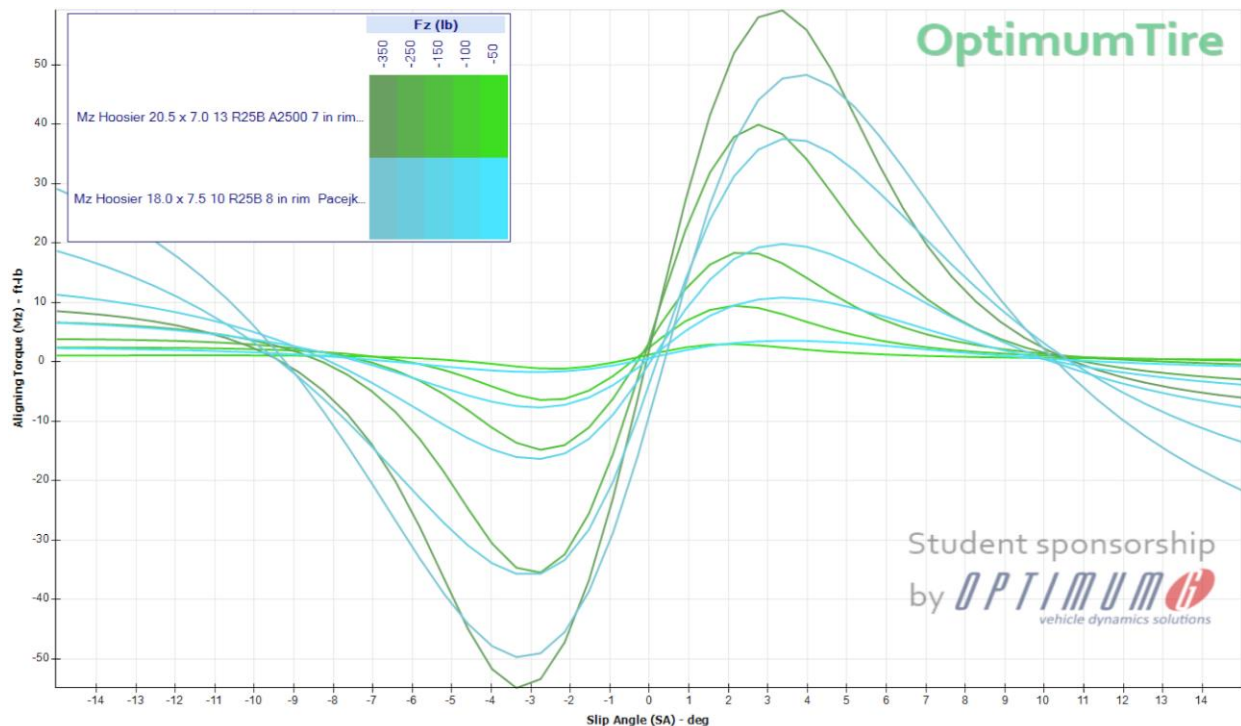


Figure 9. Aligning moment vs. slip angle plot for R25B 10s and 13s under consideration

CG Height and Overturning

It is worth mentioning that one of the focuses of the CP18C high-level design is ensuring that the car does not overturn. The CP17C struggled to avoid overturning at the 2017 competition due to added grip from aero and a particularly large CG height to track with ratio. On the one hand, the increased lateral force capability of the 10x7.5" Hoosier R25B would tend to increase this risk over the current 13x7.0" tires. However, for a fairly small increase in lateral grip, the 10" tires would drop the CG of the unsprung mass and many other components tied to the wheel height, by 1.25 inches. Including the estimated weight loss, this would result in a 0.2-inch drop in CG height from changing wheels and tires alone.

Aero

While the 10"x7.5" tires are a half inch wider than the current tires on the car, the overall frontal area of the tires is 135 square inches, 6% smaller than the current tires' frontal area of 144 square inches. The tires' frontal area varies directly with drag, so a reduction is preferred. Based on the FSAE rules design envelope for aero, a half inch wider tire allows for a half inch wider front wing and forces a half inch skinnier rear wing. However, as there is generally more room to package a rear wing than a front one, this is a worthwhile tradeoff.

Kinematics and Packaging

The single biggest design challenge in switching to a smaller tire size is outboard suspension and brakes packaging. An initial packaging study shows that the current brake calipers would fit in a smaller wheel, but outboard suspension points have yet to be established. In looking at FSAE teams with similar suspension architectures but smaller wheels than ours, a few challenges are clear. Steer link and toe link pickups are difficult to fit inside a smaller wheel while keeping bump steer at a minimum and loads in those links low (for steering effort in the front and for toe compliance in the rear). With a wider and smaller wheel, it becomes increasingly difficult to maintain a small scrub radius and to keep the normal load on the tire between the wheel bearings while maintaining sufficient a-arm angles in order to keep link loads low. However, as most of the top-performing teams in the competition run 10" wheels, it is clear that suspension and brake systems can be designed successfully within the tight packaging constraints.

Camber and Toe Stiffness

One of the driving requirements in Reinventing the Wheel's structural wheel design is camber stiffness. Under load, the suspension supporting the outside tire will tend to deflect towards more positive camber. Lateral force data for the Hoosier R25B 18x7.5-10 at different inclination angles can be found in Figure 10 – positive camber (negative inclination angle) is in the right-hand side of the plot. For increasing positive camber, limiting the loss in peak grip to 2% of maximum force restricts camber deflection to 0.4 deg/G. This means, for example, that for a lateral force corresponding to a 2 G cornering event, 0.8 total degrees of camber compliance would be tolerated. Compliance tolerances were proportioned evenly between 4 sections of the suspension--wheel, hub, upright, and links/mounts—limiting the wheel to 0.1 deg/G of camber deflection.

The CP18C tire is relatively insensitive to changes in slip angle at and above peak lateral force. As such, vehicle toe stiffness requirements were set based on tire performance in the linear range, where tire aligning moment is small, i.e. the lateral force is applied roughly at the wheel center, not behind it by some pneumatic trail³. In this range especially, the wheel does not contribute to toe deflection as significantly as the upright, toe link, inboard mounting, and chassis wall do. Hence, toe stiffness was not considered as a limiting requirement on the wheel.

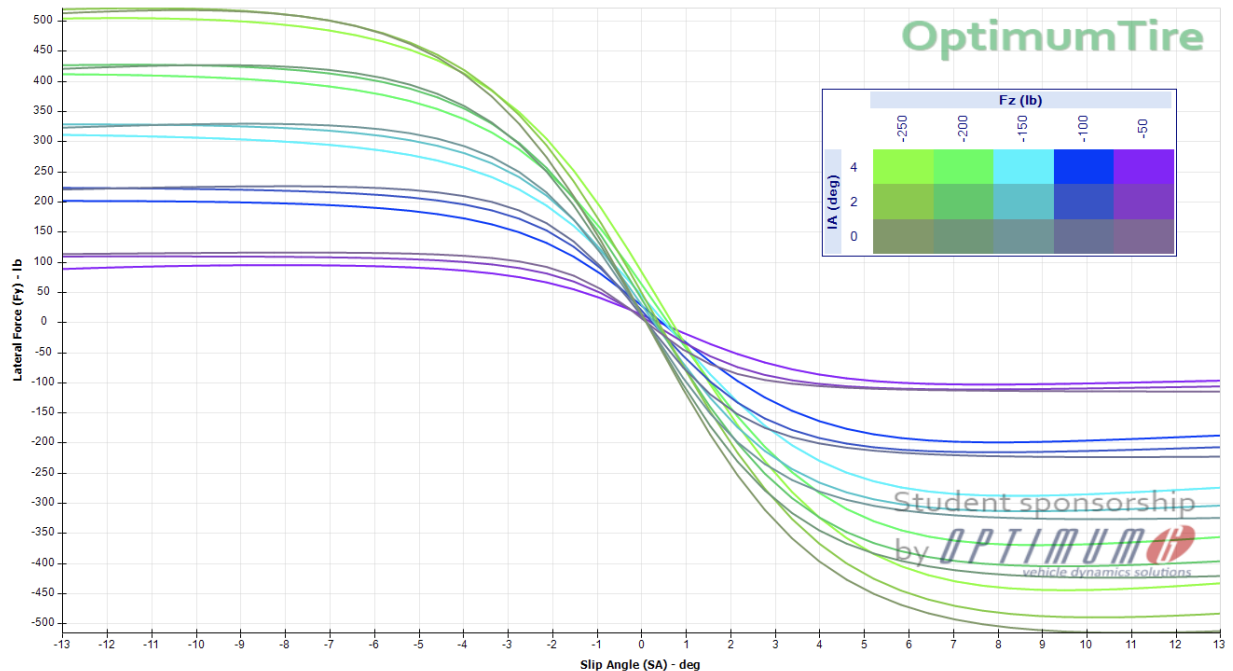


Figure 10. Lateral force vs. slip angle for the R25B 18.0x7.5-10 tires for a variety of inclination angles and normal loads. Positive camber on the outside tire is represented by the right hand (positive slip angle) side of the plot.

Conclusion

The original decision methodology was to first evaluate tires based on logistics (cost, availability), basic steady-state performance (estimated lateral and longitudinal acceleration capability), an overview of transient response (particularly relaxation length), and a consideration of the tire's relationship to other full-vehicle design parameters (drivability, aero integration, CG height, etc.). Tires not meeting basic requirements or with significantly low performance were eliminated, leaving only the Hoosier R25B 10x7.5" and 13x7". It was anticipated that the tire choice would come down to a tradeoff between grip and mass/response (with the heavier 13" tire being less responsive yet making more grip, and the lighter 10" tire having a quicker response and lower grip). This tradeoff would require transient lap simulation to answer thoroughly. Contrary to our expectations, the Hoosier 10, while allowing for an up to 5 lb lighter wheel package per corner (considering only wheels and tires and not considering rotational inertia), did not make less grip. In fact, the Hoosier 10, when compared with the 13,

³ Vehicle toe compliance tolerance was set at 0.03 deg/G. This yields a 2% loss in lateral force in the linear range.

had a slightly larger force capacity (both laterally and longitudinally), about the same relaxation length, was less camber sensitive and less normal load sensitive, exhibited a fairly similar peak aligning moment, and helped lower the vehicle CG height. The Hoosier 10 did not have as high of a cornering stiffness as the 13, but this could arguably make these tires easier feel more forgiving and easier to drive. Table 5 shows the final summary of the possible weight loss to the vehicle with these two tires, with more accurate rotational inertia estimates. (The Goodyear tire is shown here as well to demonstrate the effect that a smaller wheel can have on effective vehicle mass. The tire is very light, but on a 13-inch rim, still yields a heavier overall car than the 10s.) Based on previous Cal Poly FSAE team mass sensitivities, the possible weight loss associated with the Hoosier 10, 35 effective pounds, corresponds to a potential 10.5 second decrease in endurance times. For a significant decrease in mass from the baseline tire and similar performance otherwise, the tire choice for the CP18C is clearly the Hoosier R25B 18.0x7.5-10.

Table 5. Weight loss summary for remaining tires under consideration, the Hoosier R25B 10s and 13s, along with the Goodyears for reference

Tire	Size	Tread Width (in)	OD (in)	Tire Weight (lb)	Tire Rotational Inertia (lb*in ²)	Wheel Rotational Inertia (lb*in ²)	Full Car Weight Loss (lb)	Effective Full Car Weight Loss (lb)
Baseline	20.5 x 7.0-13	7	20.5	11	938	592	0.0	0.0
13 Hoosier R25B	20.5 x 7.0-13	7	20.5	11	938	423	8.0	14.4
10 Hoosier R25B	18.0 x 7.5-10	7.5	18.3	10	752	150	20.0	35.2
13 Goodyear D2704	20.0x7.0-13.	6.9	20.4	8.8	741	423	16.8	30.3

Rim Width

Reinventing the Wheel's tire choice, the Hoosier R25B 18.0x7.5-10, was tested on two different rim sizes, 7" and 8". Figures 11, 12, 13, and 14 are a lateral force vs. slip angle, longitudinal force vs. slip ratio, lateral normal load sensitivity, and longitudinal normal load sensitivity plot, respectively, for the tire choice. As expected, the wider rim gave the tire more cornering stiffness, hence likely giving it a shorter relaxation length. However, this increased cornering stiffness was accompanied with a decrease in longitudinal force capability and slight decrease in lateral force capability. The 8-inch rims showed slightly better lateral normal load sensitivity, although the effect is minor.

Rim width also affects suspension kinematics and packaging. Particularly in the front, the need for steering clearance drives narrower a-arm angles for a wider rim. Narrower a-arm angles imply higher loads. Keeping logistics in mind, the wheels manufactured by the project should probably match the width of the backup purchased wheels. As the team plans to purchase Keizer wheel shells and 10" Keizer wheel shells are available in specific increments only, we're limited to the choice of 7.25 or 8 inches. Additionally, it would be smart to keep all four wheels the same -- this allows wheels to be interchanged more easily in the event of a failure and

keeps manufacturing cost low by requiring only one mold. Ultimately, suspension kinematics and packaging drove the choice of rim width to 7.25”.

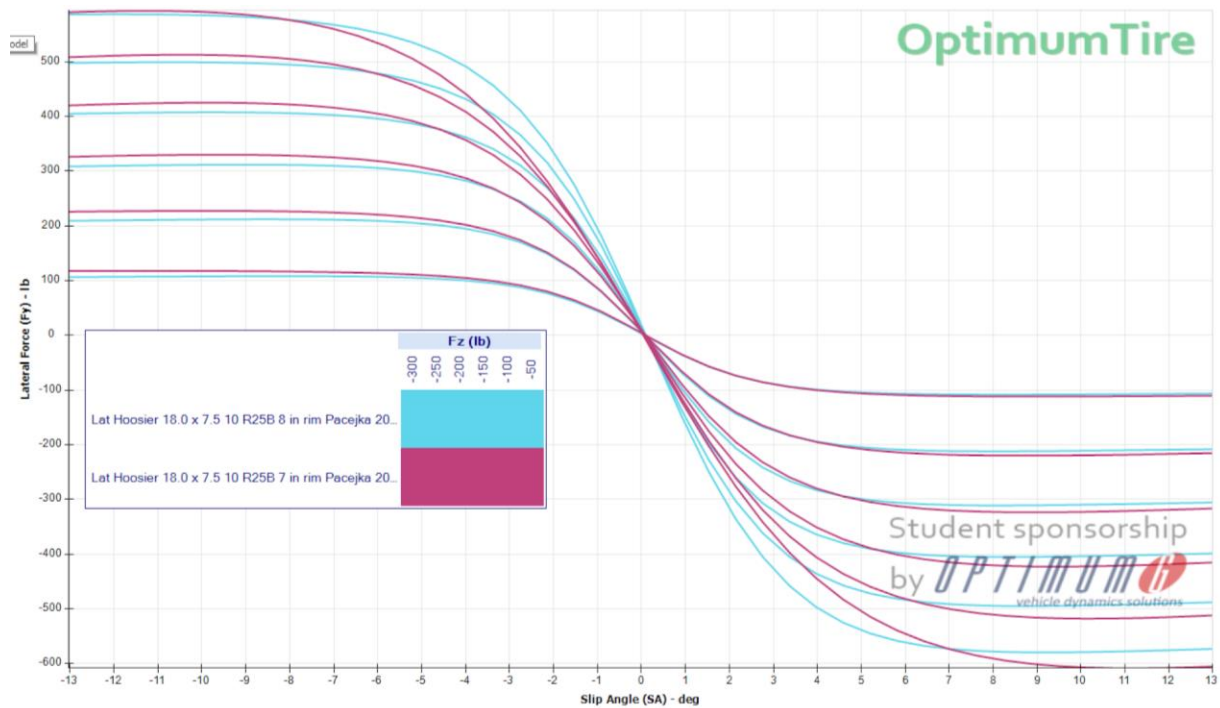


Figure 11. Lateral force vs. slip angle for R25B 18x7.5-10 on 7 and 8-inch rims

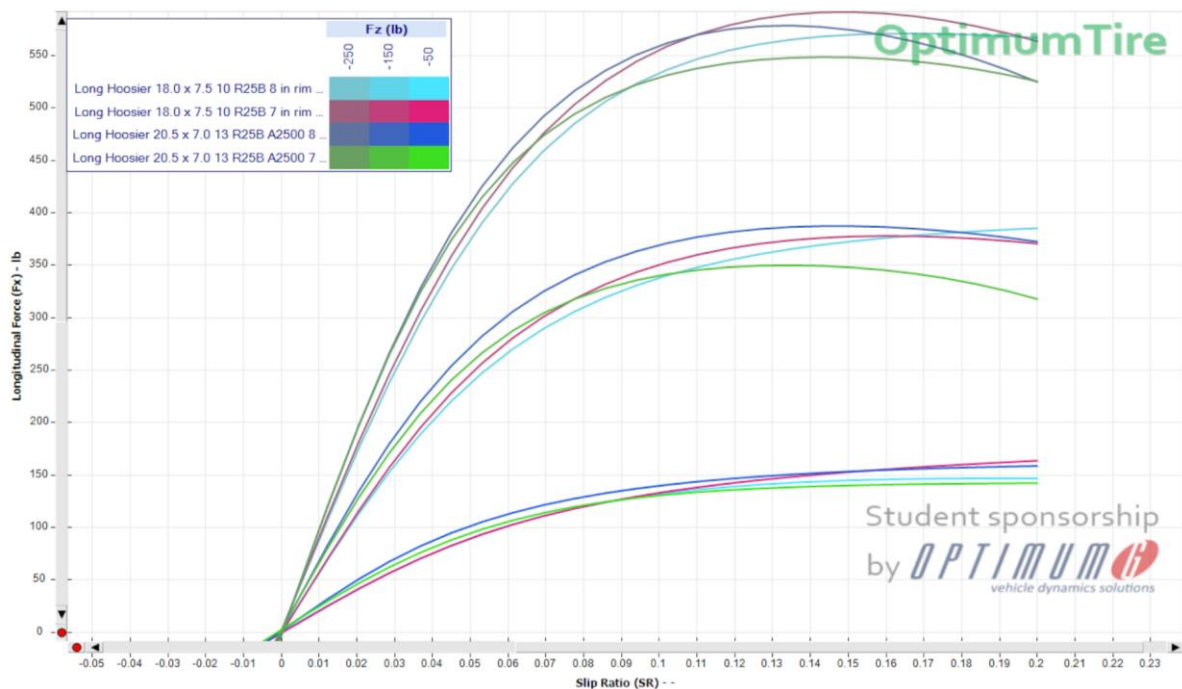


Figure 12. Longitudinal force vs. slip ratio for R25B 18x7.5-10 on 7- and 8-inch rims

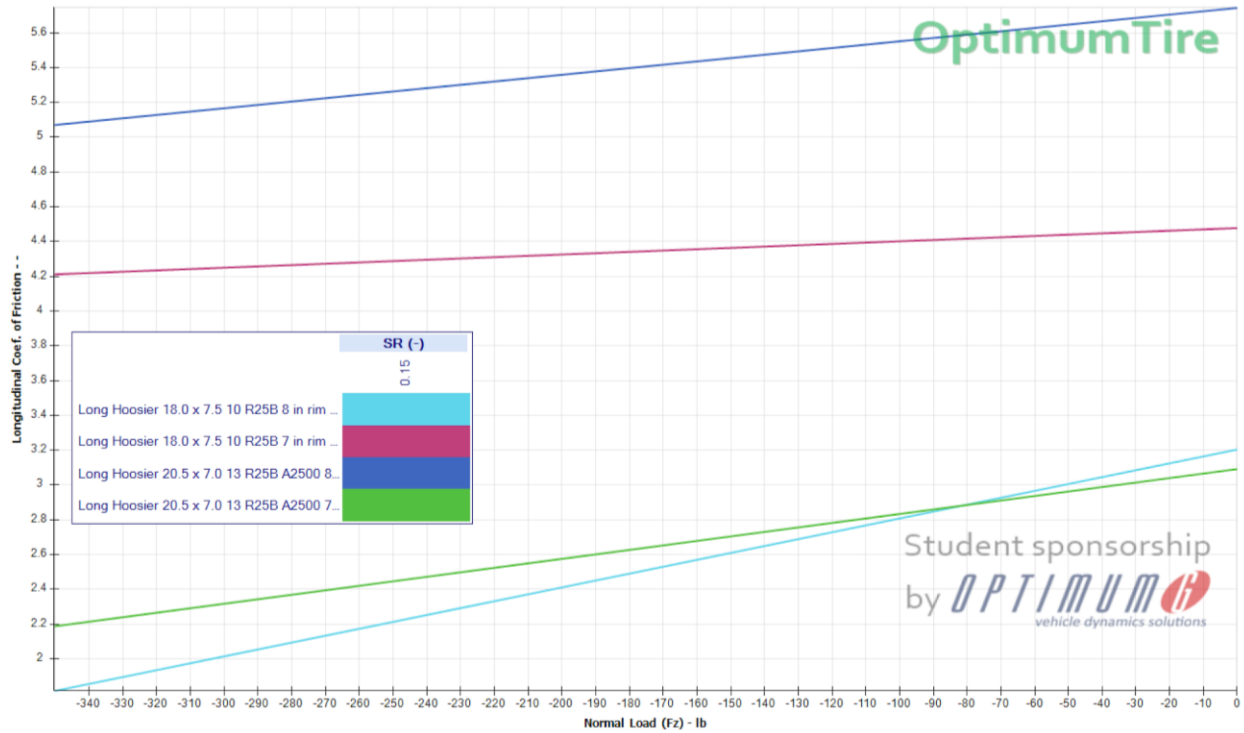


Figure 13. Longitudinal coefficient of friction vs. normal load for R25B 18x7.5-10 on 7- and 8-inch rims



Figure 14. Lateral coefficient of friction vs. normal load for R25B 18x7.5-10 on 7- and 8-inch rims

BACKGROUND – WHEEL DESIGN

In addition to withstanding the forces on the wheel imparted by the tire, the wheels must be sufficiently stiff to keep the tire within a predicted camber position to prevent (too much) loss of grip. Given that the wheels contribute significantly to the weight and inertia of the vehicle, minimizing the weight of the wheel is also desired. The wheels currently in use by the Cal Poly FSAE team are Keizer 4L 13" diameter wheels, aluminum three-piece wheels common in FSAE. Physical testing and finite element models indicate that the Keizer wheels are not sufficiently stiff to maintain our desired range of camber during cornering (described previously). Therefore, the primary structural goal of *Reinventing the Wheel*, beyond sufficient strength, was specific camber stiffness.

Composites

Composite materials, such as fiber reinforced plastics, offer superior specific stiffness to steel and aluminum wheels. Because composites can be tailored to handle loads more efficiently depending on the load direction, fiber reinforced plastics are a suitable choice for maintaining high camber stiffness while achieving low weight. Several FSAE teams have implemented carbon-fiber reinforced plastic rims for the Formula Student competition series. Review of some of these attempts offer insights to wheel design and manufacturing.

Relevant Efforts to Produce Carbon Fiber Wheels

Ohio State

OSU began their structural analysis by modeling their original full aluminum wheels and validating their model using a testing apparatus they developed. Once this was completed and the loading cases were understood, they developed four other models for analysis. Out of the five total models, a full carbon design with a bonded in carbon center had the highest specific stiffness. However, due to manufacturing and time considerations, they decided to throw this design out. The remaining designs were a carbon single-piece wheel and a three-piece wheel with carbon barrels and an aluminum center. Analysis did show that the single-piece was stiffer, however we decided to go for a three-piece design due to ease of tire mounting. For a three-piece wheel, they cited being able to assemble the wheel around the tire to mount it.

On the manufacturing side, they implemented a two-piece external tool which was split along the length of the barrel, as opposed to the diameter. Figure 15 shows a photo of this tool. The rim was trapped during the cooling of the tool after cure and attempting to remove the rim from the tool resulted in destruction of the wheel. (2)



Figure 15. OSU carbon fiber rim entrapment

Kansas

The Kansas FSAE team produced a single-piece carbon fiber wheel. They had already been running a carbon barrel and aluminum center, so the goal of the project was to pursue greater weight savings. The structural analysis was set up relative to a specific stiffness benchmark, set by 13" Keizers. According to their analysis, the one-piece was 19% stiffer, 11% lighter than the previous design, and about 4 lbs lighter than the Keizers. However, their original aluminum center wheel turned out to be 3.6% stiffer than the one-piece. This was disregarded since the margins were minimal and they stood to save 1.18 lbs with a one-piece. Kansas implemented silicone pressure intensifiers to produce a hollow rim geometry. They also seemed to have modeled the multiple piece wheel with bonded contacts, not taking into account fastener compliance. This may artificially increase the stiffness of the multiple piece concepts. (3)

Cal Poly

Several previous Cal Poly FSAE teams have attempted to implement carbon-fiber wheels. In 2009 the Cal Poly FSAE team produced carbon wheels. Their wheel featured a conical barrel which reduced the deflection of the wheel during vehicle cornering. By using a conical barrel, the size of the wheel center is reduced, which reduces bending and overall wheel deflection. Although the team did successfully produce several wheels, the barrels failed at the bead seat during tire mounting and none were successfully used. Another prior Cal Poly FSAE team produced 10" wheels. The tooling methodology both teams used was similar: Both featured two inner mold line (IML) tools to manufacture the barrels in separate pieces.

TU and Joanneum Graz

TU and Joanneum Graz are two teams which have been successfully running full carbon wheels for at least the past couple of years. Both wheels feature a center lock design, and currently have hollow spoke geometries. Prior to their hollow spoke design, Joanneum ran a U-channel solid spoked wheel.



Figure 16. TU Graz



Figure 17. Joanneum Graz

Industry

In industry, two major manufacturers of carbon wheels are Koenigsegg and Carbon Revolution. Carbon revolution uses an automated dry fiber orientation and resin infusion process to produce their wheels. These are also one of the few examples of a non-center lock wheel design. As seen in the cross section below, the hub connection features flanged inserts, in addition to plating on the inner surface likely to increase surface toughness. There is not technical information on this, but upon inspection of the cross section, it seems that some sort of spoke core is used. Koenigsegg's wheel features hollow spokes and a center lock. This is a single piece wheel, and a brief look at the manufacturing process can be seen on YouTube.



Figure 18. Carbon Revolution Cross section



Figure 19. Koenigsegg Carbon Wheel

Composites Manufacturing

Manufacturing fiber reinforced plastic composites presents unique challenges. Fibers must be laminated on a precisely manufactured mold, then cured for times ranging from 20 minutes to several hours. In the case that pre-impregnated fibers, or “prepregs,” are used, the mold and fiber must be cured at elevated temperatures for several hours. In this case, coefficient of thermal expansion and thermal mass of the tool material must be considered. Most composite lamination tools only control one side of the cured laminate, leaving the other side wavy due to local resin buildup. Special tools called clamshells may be used to control both sides of a composite laminate during cure, resulting in superior surface profile control compared to traditional tooling. These tools are typically more complex and expensive than traditional tools. Furthermore, machining fiber reinforced plastic materials typically requires special tooling.

REQUIREMENTS – WHEEL DESIGN

The engineering requirements for the wheel are shown in Table 6.

Table 6. Engineering requirements for wheel design

Spec #	Parameter	Requirement/Target		Tolerance	Risk	Compliance
		10" Tire	13" Tire			
1	Weight	3lb	5 lb	Max	H	A,T
2	Cost	\$2000		Max	M	A, I
3	Rim Profile	In Accordance with Tire and Rim Association Specification		Min	H	A,S,T
4	Camber Compliance	< 0.1 deg/g		Max	H	A,T
5	Safety Factor	1.2		Min	H	A,T
6	Lateral Loading Case	2.7 G		Min	H	A,T
7	Longitudinal Loading Case	2.48 G		Min	H	A,T
8	Combined Loading Case	1.4 Gx, 1.5 Gy		Min	H	A,T
9	Tire Pressure	12 psi		Min	H	A,S,T
10	Seating Pressure	35 psi		Min	H	A,S,T
11	Design Life	2 Seasons		Min	H	A,I,T

Load cases on the wheel were derived from the maximum accelerations in the table above, as explained further in the following sections. The maximum acceleration cases were determined by the FSAE team as part of the high-level vehicle requirements. 10 psi is a typical tire pressure run on the for the FSAE car, but 12 psi was used as the design pressure to be conservative. The maximum pressure on the tires is 40 psi, and 35 psi is typically used as a seating pressure, so the wheel must be able to withstand this. A minimum safety factor of 1.2 is required on the wheel, although it is expected that the part be largely stiffness-limited, particularly by the camber stiffness requirement. The wheel is allowed to deflect 0.1 deg/g in camber, one-quarter of the total suspension camber compliance allowance.

Target wheel cost includes the cost of composite tools needed to laminate the wheels and composite processing equipment such as gloves, sandpaper, dust masks, and post-bond adhesives. The wheel cost does not include prepreg materials, which was sponsored by TenCate Advanced composites.

Determining Tolerances

In order to determine a realistic tolerance for our wheels, we compared three Keizer 13" wheels: one fresh out of the box, one currently in-use wheel with a tire mounted at 10 psi, and one used wheel that had been deemed too out of tolerance to run by a previous test of concentricity to the hub. Using the Micro Vu Vertex and Zeiss DuraMax CMMs, we were able to measure many different aspects of the wheel including runout between the bead seat and center locating feature, true position between the lug holes and the center ring axis, circularity of the bead seat, profile of the bead, as well as a few other regions of interest. An interesting finding was that the Keizers had drifted from a circularity of .003" to .08" over the course of a few seasons. Additionally, the majority of the barrel was significantly different from the straight profile in the provided CAD model. The radius at the start of the bead was also significantly larger in real life than in cad, and the bead lip did not continue as far out as the model. Results from the new Keizers, in addition to hole shaft fitment calculations done on the interface between the hub, center ring, and wheel, were used to help set our tolerances and evaluate how the wheel must be tooled.

Table 7. Tolerance baseline and requirements

Feature	Keizer (baseline) (inch)	Requirements (inch)
Runout between bead seat and center ring	0.054	0.080
True position between center ring axis and lug pattern	0.013	0.015
perpendicularity between center ring and hub mating face	N/A	1.63 deg misalignment
Flatness of hub mating surface	N/A	0.003
Circularity at bead seat	0.0026	0.05
Profile of bead seat	N/A	0.125

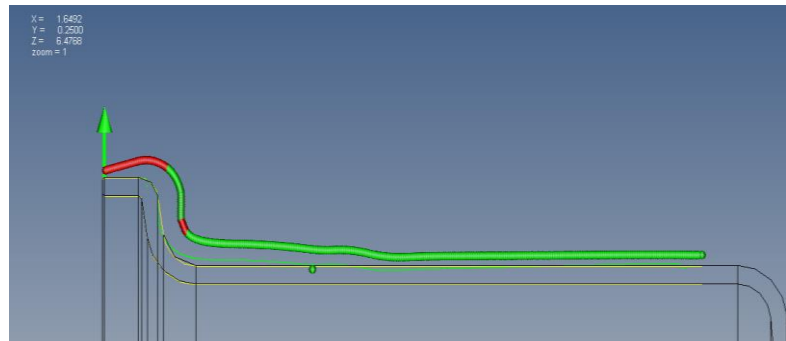
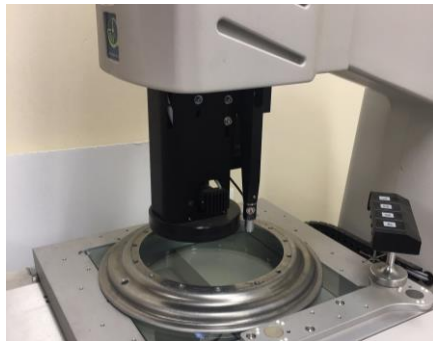


Figure 20. Micro Vu CMM setup and Zeiss profile output

Structures

Loads

The lateral, longitudinal, and normal loads on the tire at the contact patch can be resolved to the center of the wheel as shown in the diagram below. As described in the discussion of aligning moment in the tire choice section, the lateral force on the tire is applied at a point slightly behind the center of the contact patch -- this distance is called pneumatic trail and is denoted in the

diagram below as n_p . The mating plane between the hub and the wheel does not necessarily occur along the centerline of the tire either -- the distance between the center plane of the tire in the front view and the mating plane between the hub and wheel is called the wheel offset. In the diagram below, R_t denotes the tire radius.

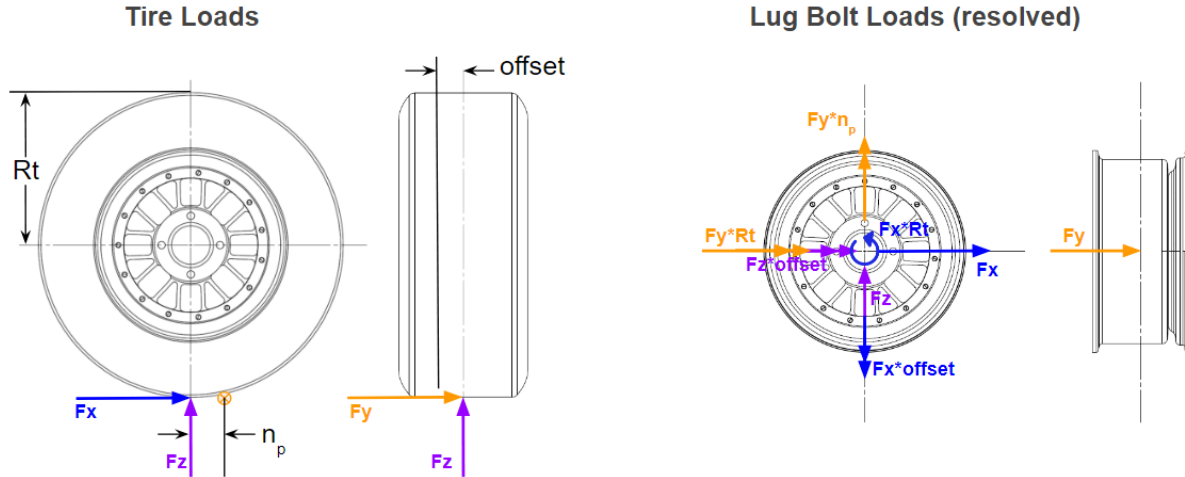


Figure 21. Wheel loading

Several load cases were considered in analysis of the wheel -- these can be found in Table 8. Conservative estimates of maximum braking, maximum cornering, and combined braking and cornering were used. Loads for the most heavily loaded wheel on the car during each event were chosen. The high end of the tire pressures run during normal operation and tire installation are also included.

Table 8. Wheel design loads

Load Case	Normal Force, F_z	Longitudinal Force, F_x	Lateral Force, F_y	Pressure, P
	(lb)	(lb)	(lb)	(psi)
2.7 G Cornering	337	0	768	12
-2.48 G Braking	284	-527	0	12
-1.4/1.5 Combined Long/Lat	322	-555	623	12
Bump	450	0	0	12
Tire Seating	0	0	0	35

The forces on the tire are resolved at the base of the bead seat of the wheel. According to research in *Carbon Fiber Wheel* (1), the loads at the tire contact patch are resolved as pressure distributions governed by the following equations:

$$P_w = P_{w0} * \cos((\pi/2) * (\theta_w/\theta_0))$$

Where P_{w0} is the maximum pressure of the tire, which is found using the equation:

$$P_{w0} = (w * \pi) / (tb * rb * 4\theta_0)$$

Where w is the normal load on the tire, tb is bead width, and rb is bead radius. For a typical automotive tire, θ ranges from -40 to 40 degrees. The resulting pressure distribution profiles for normal, longitudinal, and lateral loads are shown. The longitudinal and normal loads are applied symmetric about the wheel center plane to the inner and outer bead seats. The lateral load is applied only to the inner rim bead seat.

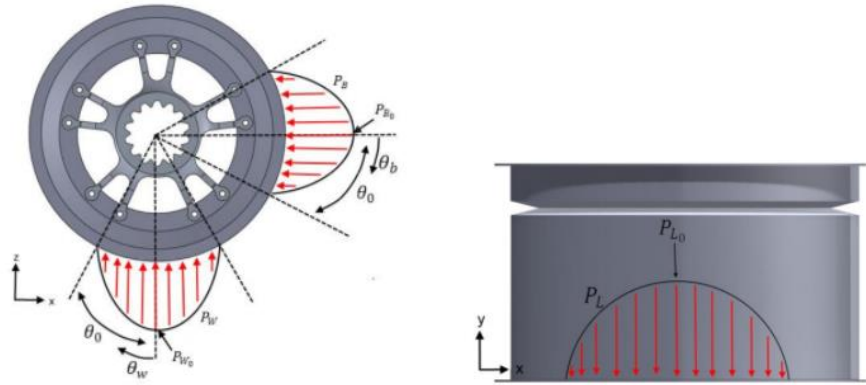


Figure 22. Bead seat load distribution

In addition to the transposed loads mentioned, the torsion (T_L) about Y , and aligning moment (M_a) about Z , are applied to both bead seats. This torsion assumes no slip of the tire under longitudinal loading, and is the same torque applied to the lugs as previously shown. Aligning moment is a result of lateral loading offset by a pneumatic trail of 1".

Pressure (P) is applied on all surfaces between the bead seats to simulate the operating pressure of the tire. This tire pressure also causes the tire to expand outwards, resulting in load on the bead flanges. The total load on each flange is governed by:

$$Ff = (rt^2 - rf^2) * (P * \pi/2)$$

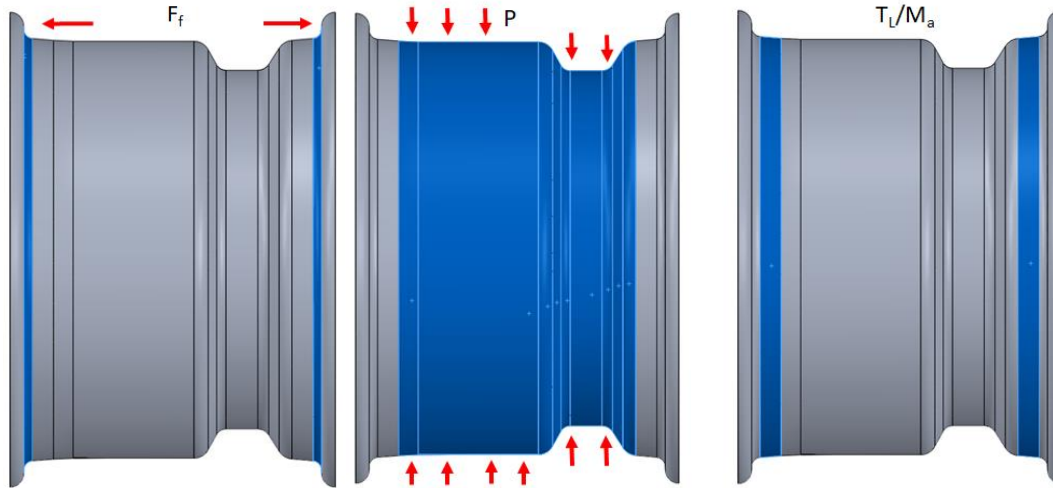


Figure 23. Pressure, flange load, torque, and aligning moment application

ANALYSIS

Methodology

The following sections discuss the design and analysis process for the wheel, according to the following methodology:

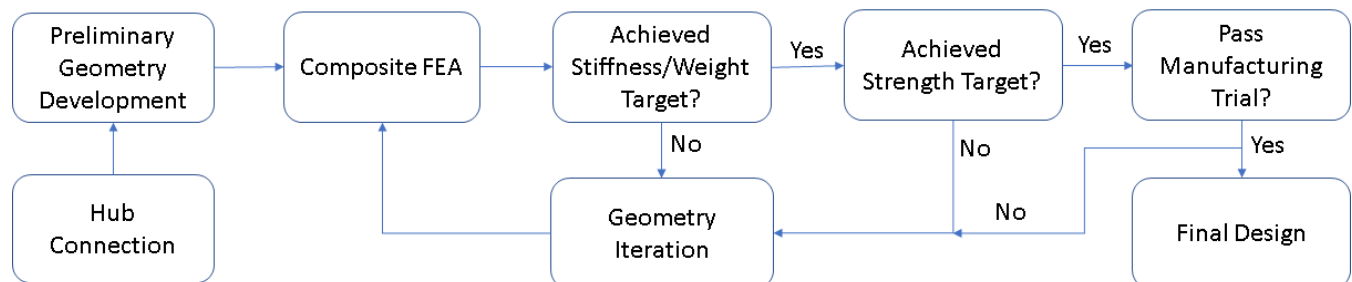


Figure 24. Wheel structural analysis and design iteration methodology

Hub connection analysis includes sizing of lugs and insert design. This is done first as it is a driving factor in some of the geometric decisions of the wheel. Next, preliminary analysis is done to determine the most structurally efficient geometries utilizing simplified methods. The preliminary design is then detailed in a FE stiffness analysis. The wheel is assumed to be stiffness driven, which is why it is performed prior to strength analysis. Before jumping into composite stiffness analysis, laminate requirements are set in order to reduce the number of iterations. This takes into account things like ease of manufacturing and basics of laminate construction. Laminate iterations are then performed on the maximum cornering case to determine whether the design achieves the set performance target. As this is done, wheel weight is monitored. If the stiffness target cannot be achieved under the projected wheel weight, further geometric iterations are required. Once acceptable stiffness is achieved, strength analysis is performed to ensure reliability of the final wheel design. A manufacturing trial is done

after the first round of analysis to ensure manufacturability of the geometry. If this fails, one must iterate geometry and go back through the analysis flow shown above.

Hub Connection

Concept Designs

The bolted joint between the hub and the wheel has two functions: to locate the wheel relative to the rest of the suspension and to transfer load from the wheel to the hub. Three proposed design solutions were considered for this connection and evaluated on weight, manufacturability (particularly with regards to tolerancing), and efficiency of load path. A center lock design was not considered due to being out of scope for the team and this project.

Tapered Lug Nuts

The first concept relies on radially positioned lug studs to both locate the wheel and transmit all load. The lugs would slip fit into tapered holes in the wheel, allowing the wheels to be easily put on the hubs. Tapered lug nuts would tighten down on the lugs to center them in the tapered holes, theoretically positioning the wheel concentrically with the hub. A layout of this concept is shown in Figure 25. This is lightest solution out of the three evaluated -- it is estimated at about 0.18 lbs per corner, assuming three 5/16" lugs and lug nuts. While it is also the simplest design, there are several issues with the retention method. Firstly, if the lugs loosen during operation, location of the wheel is lost, allowing the wheel to move around considerably and likely speeding up the process of fully loosening the lugs and losing a wheel. Secondly, since the tapered lug nuts would have a closer fit with the wheel than the rest of the stud, all the shear would be transmitted through the tapered portion of the nut which is generally fairly short, as shown in Figure 26. Concentrated shear along a thin section is a poor load path and would likely force the design into added weight or into unexpected failure. Lastly, it is difficult to properly align all of lug studs, nuts, and holes. This design would require very tight tolerances in the position and vectors of the lug holes to prevent misalignment issues from over-defining the position of the wheel with three to four separate locating features. And even if the tolerances are tight, bolting up the wheel required care to ensure that the lug nuts seat themselves properly in their tapered holes. Any misalignment in either of these, manufacturing or installation, would result in uneven contact between the lug nut and hole tapers, exacerbating the poor loading problem described above. Overall, this design is insufficient.

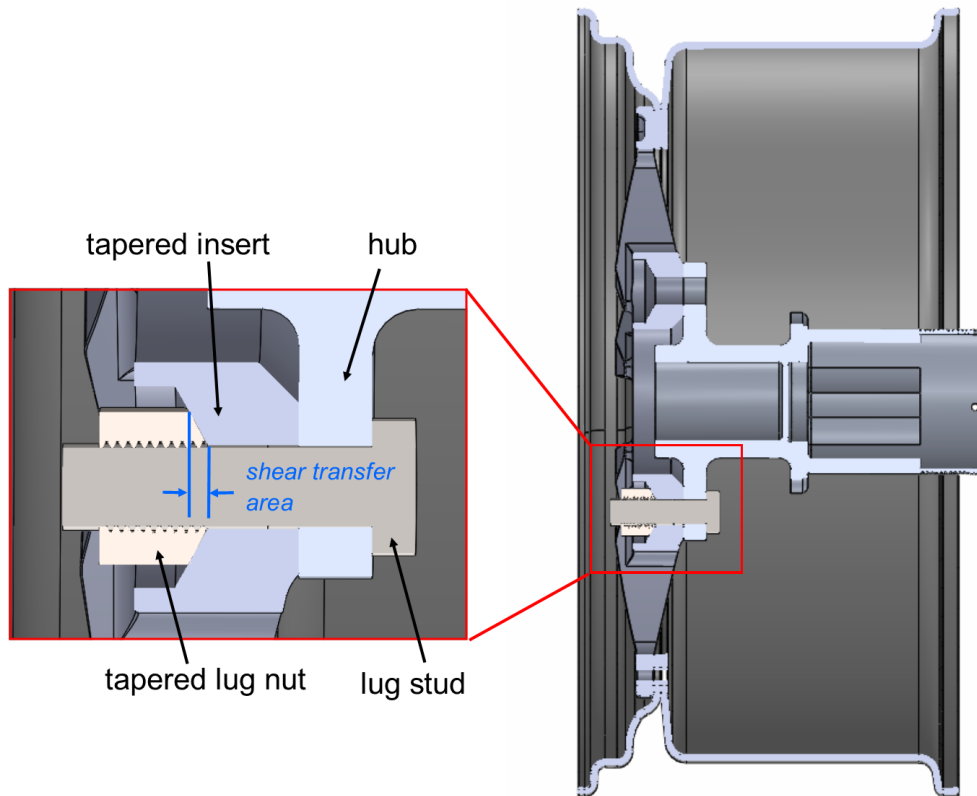


Figure 25. Tapered lug and stud concept design



Figure 26. Typical tapered lug stud

Shoulder Bolt and Nut

This design features a stud with a shoulder that fits tightly into a hole on the wheel. A stepped nut with a matching shoulder meets the stud in the same hole. A layout of the design concept is shown in Figure 27. While the shoulders fix the load path problem of the tapered lug stud and nut design, they do not fix the difficulty in manufacturing and installation of locating a wheel on an over-defined set of holes. This is also the heaviest design concept, at 0.46 lbs a corner (assuming 5/16 threaded portion and reasonable step sizes). Lastly, this concept would require us to make our own fasteners, increasing manufacturing time.

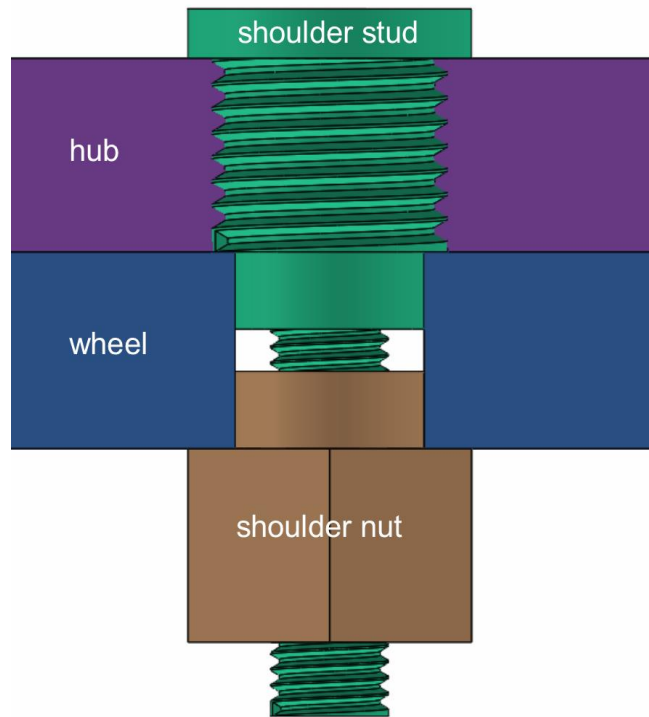


Figure 27. Shoulder stud concept design

Center Ring and Clearance Studs

Unlike the previous two design concepts, this design uses a central locating feature, separate from the lug studs, to concentrically locate the wheel on the hub. The hub would have a boss extending out the end which locates tightly to a cylindrical feature at the center of the wheel. A pattern of lug studs would surround the center feature radially. The lug holes would be a slightly looser fit to the lug studs than the center ring to the hub to avoid over-constraining the wheel. The wheel load would be split up between the lugs and the center feature as well -- the center ring would react direct shear, i.e. normal load and the longitudinal force due to braking or accelerating. The lug studs, on the other hand, would take the overturning moment on the wheel in tension and the braking and accelerating torque in direct shear. At an estimated 0.39 lb per corner, this is a relatively light design with a reliable load path and components that can be easily purchased or manufactured in-house. This is the chosen concept for the *Reinventing the Wheel* hub-wheel connection -- a layout is shown in Figure 28.

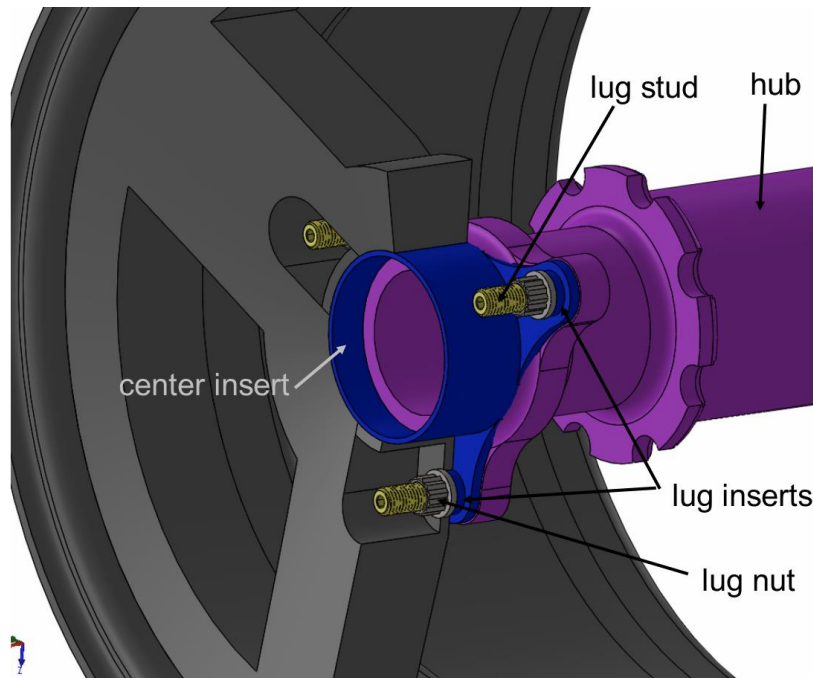


Figure 28. Reinventing the Wheel Hub-Wheel Connection

Detailed Design

Inserts are required in the lug bolt holes to support the compressive load of torquing down the lug nuts without compressing the laminate to protect against surface damage. Similarly, an insert is required for the center cylinder that fits closely to the hub to ensure that contact between the hub spigot and the wheel doesn't damage the carbon. A machined and properly located insert can also provide a tighter surface tolerance for wheel/hub fitment than carbon fiber can. Due to the high compressive requirements outlined in the insert structural analysis below, aluminum was chosen as the insert material. It is sufficiently strong to support the compressive load, easy to machine, and lightweight.

The original intent was to bond in lug inserts and the single center insert all separately. However, tolerance requirements would make bonding each insert separately incredibly challenging. The position, hole vector, and flatness at the hub mating plane of each feature -- the lug holes and center hole -- are all critical to one another, as outlined earlier in the tolerance requirements. To remedy this, the insert was designed as one continuous piece, as shown in Figure 29. For a mere 0.0170 lb per center insert (20% increase in mass), the separate lug inserts and center insert can be connected in a single machined part, guaranteeing all of the critical tolerances between these features can be held. The single insert also saves the time to design, manufacture, and use a complex bonding fixture -- with a single-piece insert, only the center feature needs to be located, not each individual lug. Lastly, a single-piece center insert provides a continuous face of contact for the hub. This will likely add stiffness to the joint since a full face of contact can react normal load better than single bosses around bolts can.

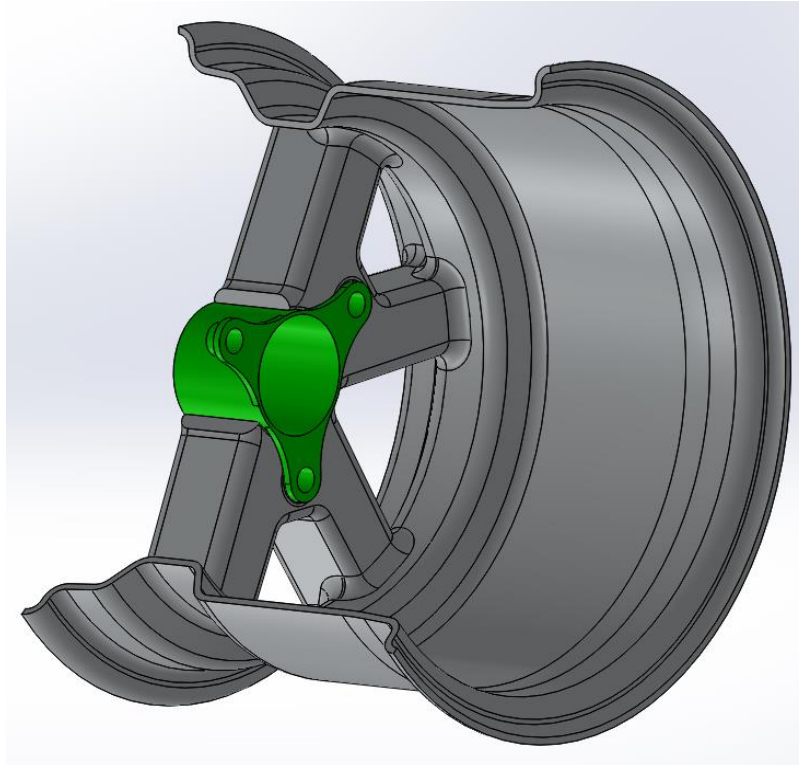


Figure 29. Reinventing the center insert

Stud Retention

Two methods of lug stud retention in the hub were considered: knurls and threads. Knurled lug studs, like the one shown in Figure 30 are common in production vehicles. Press-fitting the knurled stud into a hole in the hub provides retention against torqueing for little added mass to the stud. However, past Cal Poly FSAE cars have had problems with knurled studs stripping the hole in the hub when over-torqued. Most off-the-shelf knurled studs are designed to be pressed into steel, so they have shallow, fine-pitch ridges. Unlike most OEM hubs, the hubs on the FSAE car are made of aluminum, so the small knurls tend to just shear away the aluminum when excessively torqued (measured to be about 140 ft*lbs on the 1/2" studs used on the CP17 cars) or widen the holes over time under load resulting in loose studs. This problem would likely be fixed if wider pitch, more aggressive knurls designed for aluminum were used, but these have proven difficult to find, especially in the low sizes we run.



Figure 30. Knurled studs

Another solution to stud retention is threading the studs directly into the hub. Threaded lug studs allow for the studs to be replaced if necessary. This is especially helpful in the event that stud fatigue becomes a greater problem than estimated by calculations or if longer studs are required

to perform a test using wheel spacers, etc. These studs can easily be retained by seating the tapered section to a slight countersink and safety-wired to pass rules as positively retained fasteners.

Due largely to the availability of threaded lug studs (and not knurled lug studs) in the size that we'd like to run this year, threaded lug studs were chosen.

Bolt Circle Radius

The minimum bolt circle radius was chosen as 1.75", a safe distance from the hub boss to clear any fillets on that feature. Since any increase in the bolt spacing requires the addition of aluminum hub and insert material, it was decided that the bolt circle be chosen as this minimum radius. In this case, the most specifically stiff wheel is the one with least aluminum at the center, since adding aluminum is less structurally efficient than adding an equal weight of carbon. If future teams use an aluminum wheel center, a study should be performed to find the bolt circle radius which produces the lowest weight hub and wheel assembly while meeting the required strength and stiffness.

Structural Analysis

Bolt Calculation Assumptions

The sizing of the lug studs began with the wheel loads resolved to the wheel center as described in the loads section. Knowing that the hub boss to center ring joint will be a closer fit than the lug studs to the lug holes (.015" diametrically on the center feature vs. .050" on the lug studs), it is assumed that the hub boss takes all direct shear loads to the wheel center, i.e. the longitudinal and normal loads applied directly to the wheel center. The contact between the hub and the center insert at the face of the hub-wheel mating surface can be assumed to take the direct lateral load to the wheel center. The lug studs are responsible for reacting the moments to the wheel, primarily the overturning moment due to the lateral force and the torque due to braking. The overturning moment will be reacted in bolt tension that varies as the wheel turns. The brake torque will be reacted by direct shear in each bolt at the wheel-hub plane. As a first pass, the radius to react all moments was assumed to be the bolt circle radius, but once the number of bolts was chosen, this was updated to reflect actual geometry. In the case of three lugs, as was chosen, the reaction radius was chosen as a fraction of the bolt spacing, as shown in Figure 31. It is assumed that the overturning moment on the wheel is taken by only two bolts in tension at the aforementioned spacing, but for the braking torque, it is assumed that all lugs participate equally. The hub and center insert can both be expected to hold tight tolerances since they're both CNC parts, so it is not an unreasonable assumption that all studs will contact the insert walls equally (although it is not conservative). Preliminary calculations were performed with a preload force specified as twice the load required to separate the joint. Maximum torque specs were checked later. Cornering was a slightly worse case for the safety factor on yield, but all cases -- max cornering, braking, and combined loads were checked, not only for bolt sizing but for insert design as well.

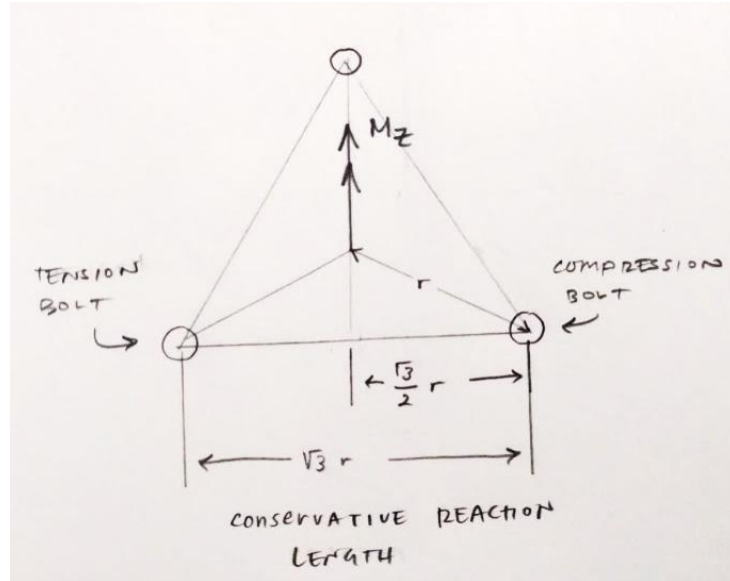


Figure 31. Reaction radius

Fatigue Analysis

It is worth noting that the tension in the bolts is cyclic, at least while cornering, meaning that a fatigue analysis of the studs is warranted. Braking and acceleration loads are sustained in the lugs throughout a braking or driving event, so these loads are taken as mean loads, not alternating ones. To analyze the fatigue, average load cases are used instead of maximum ones. (The car corners frequently, but not always at the limit.) Scaled up for the CP18C's tires and expected performance, the average cornering and braking accelerations during a typical endurance run are 1.0 and 0.5 Gs, respectively. It is difficult to accurately predict the number of cycles the car sees over the course of a season, so the studs were sized for infinite life. Both Gerber and Modified Goodman fatigue failure criterion were checked, to provide non-conservative and conservative estimates, respectively. Table 9 contains safety factors on static and fatigue failure.

Table 9. Bolt sizing

Bolt Size	Number	SF on Inf. Life Goodman Fatigue	SF on Inf. Life Gerber Fatigue	SF on Von Mises Yield
1/4	3	0.5672	0.4766	0.6991
1/4	4	0.5718	0.4848	0.7083
5/16	3	0.9041	1.0804	1.1382
5/16	4	0.9117	1.0971	1.1539
3/8	3	1.369	2.0803	1.7617
3/8	4	1.381	2.1071	1.7872

The decision was originally made to use three 5/16 bolts. However, considering the uncertainty in the fatigue analysis, the method by which loads will actually be distributed, the unexpected

load cases (like students pulling on the wheels to move the car), and most importantly torque spec, the decision was made to use 3/8ths bolts instead. As these are student cars and many inexperienced hands torque wheels, we need to protect for students accidentally over-torquing the bolts. These calculations assume a torque spec of 24.5 ft lbs on the 5/16ths and 27.5 ft lbs on the 3/8ths (safety factor of 2 on joint separation). Using a more reasonable torque spec, around 35 ft*lbs, for example, safety factors drop considerably. The 5/16ths bolt is safe in loaded yield to up to 29 ft*lbs, whereas the 3/8ths is safe to up to 55. It is also worth noting that an unthreaded shank stud was chosen, so as to avoid the stress concentration of threads in direct shear. A stress concentration factor was not used in calculating normal stress since there are no threads in between the nuts. This non-conservative assumption further justifies the need for a higher safety factor bolt choice.

Insert Sizing

Bearing stress on the insert walls under maximum braking torque was checked, yielding a safety factor of over 6. The insert wall thickness was chosen to favor a failure of the stud instead of the insert since the studs are easier to replace. If over-torqued, the combined preload force and wrench-on torque would fail the bolt before yielding the insert under compression. (In this case, the safety factor on the stud wrench-on stress is 1 when the insert compression safety factor is 1.2). The wall thickness on the center ring was sized using a safety factor of 2 on von Mises stress as found in the FEA model. In order to prevent peeling of the insert away from the wheel under inside wheel cornering, a washer should be bonded to the outboard face of the wheel. This washer provides a load path into the wheel for the tension of pulling the wheel away from the hub, as opposed to reacting the load solely with the adhesive.

Final Design

A black-oxide high-strength fine-to-coarse stud was chosen as the lug stud -- a model of one is shown in Figure 32. The nut was chosen as a matching black oxide 12 pt. flange nut, a lightweight but sturdy fastener. A full layout of the design is shown in Figure 33. Both stud and nut can be purchased from McMaster Carr. A drawing of the insert can be found in Attachment A. When purchased, we discovered that the coarse thread side of the stud featured a taper. For future hubs, we recommend countersinking the threaded stud hole to match the stud's own taper, then seating the stud against this taper by tightening it into the hub to a torque spec greater than the lug nut torque spec to ensure that the studs do not loosen when loosening lug nuts.

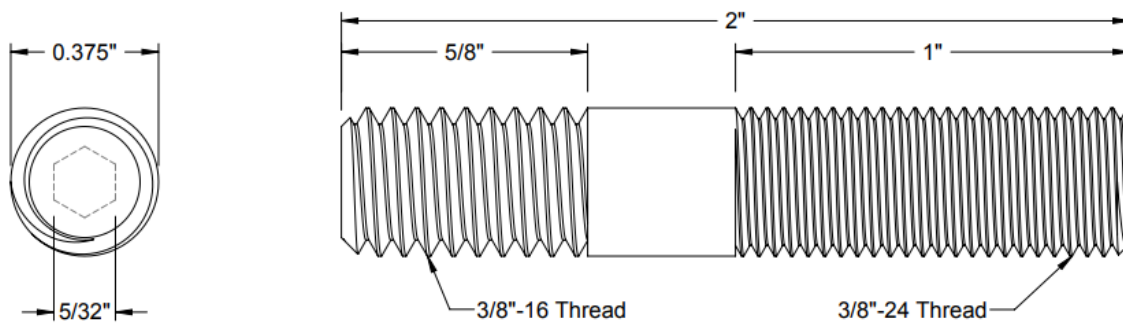


Figure 32. Drawing for the threaded lug stud

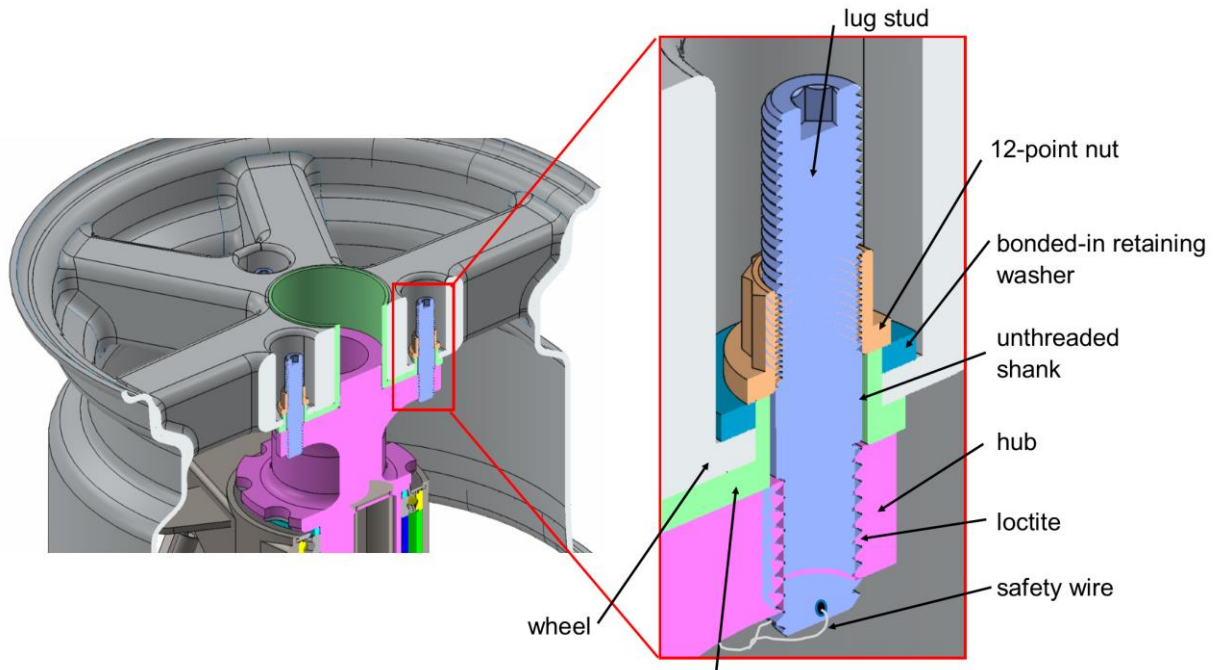


Figure 33. Design layout for hub connection with center ring and threaded studs

Wheel Geometry

The following geometric studies utilize simple analysis to narrow down the most efficient structure early on. This allows for saved time during detailed design and develops an understanding for certain geometric effects. Manufacturing considerations are briefly mentioned but discussed in greater detail in the manufacturing section.

Stiffness Sensitivity

A wheel consists of two main load carrying components; the center and barrel. As shown in previous sections, tire loads are transmitted through the bead, and reacted at the center due to the hub bolted connection. In order to develop an efficient structure, it is essential to understand the stiffness contributions of each component. This is because the center and barrel can be considered 'springs in series'. If k_2 is significantly stiffer than k_1 , a stiffness increase in k_2 has minimal positive effects on the system, as governed by the relationship below. Therefore, understanding stiffness contributions allows for an equal distribution of stiffness across all springs and series.

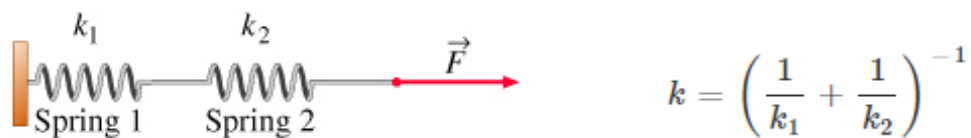


Figure 34. Springs in series

To establish a preliminary understanding of these effects, FEA was performed on a basic 10" wheel design, with the 2016-2017 lug pattern. The wheel was fixed at the lug holes, and a constant load was applied at the bead opposite of the center. Both normal and lateral loading effects were studied.

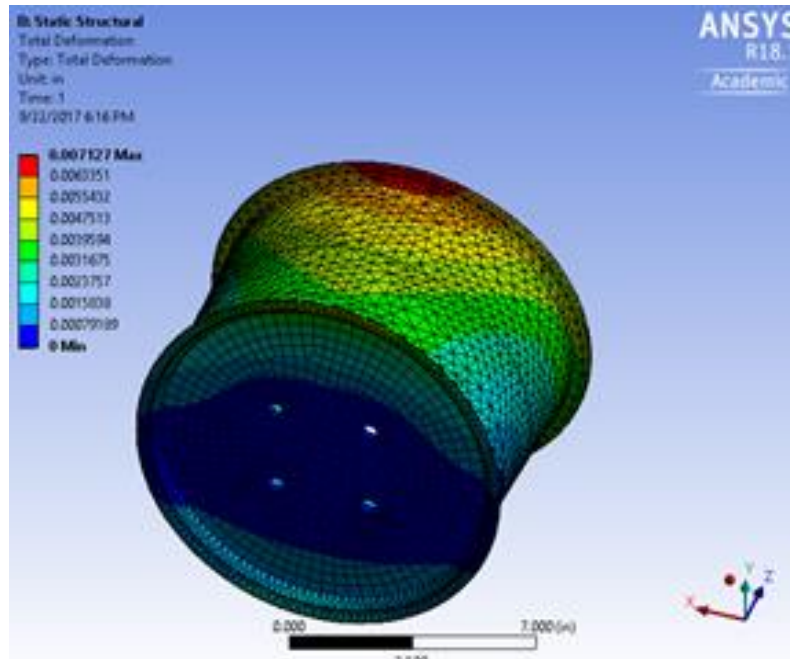


Figure 35. Baseline, lateral loading

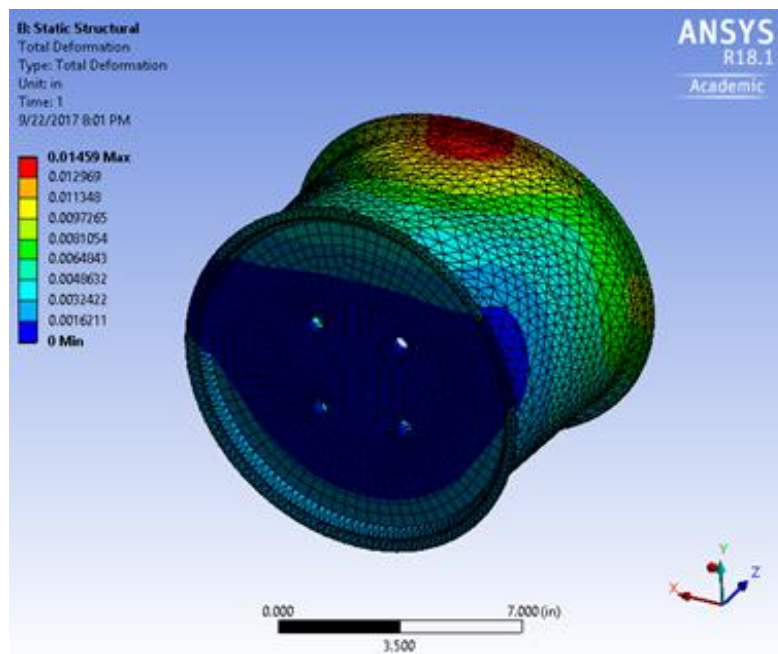


Figure 36. Baseline, normal loading

As seen in the Table 10 below, a rigid center increased stiffness from the baseline by ~16x that of the barrel under lateral loading, and ~3x under normal loading. In the lateral loading case, the barrel was 9x as stiff as the center, highlighting the dominant effects of a weaker spring in series. The exact magnitudes of these differences depend on the relative stiffnesses of the barrel and center, which were set arbitrarily. However, this still indicated that efforts to stiffen the entire system were much more effective at the center, which is what the following sections focus on. Even though this suggested that the center is inherently the weak spring in series (due to primarily being loaded in bending), relative stiffness to the barrel was monitored to ensure efficiency throughout the detailed design process.

Table 10. Relative stiffnesses

Lateral Loading				
	Load (lb)	Vertical Deflection (in)	Stiffness (ft*lb/deg)	Difference (%)
Baseline	200	5.48E-03	1745	
Rigid Center	200	3.18E-04	30050	1622.06
Rigid Barrel	200	2.84E-03	3369	93.07
Normal Loading				
Baseline	200	5.48E-03	934.81	
Rigid Center	200	3.18E-04	9113.85	422.28
Rigid Barrel	200	2.84E-03	4488.68	157.23

Spoke Cross-Section

The spokes were designed to have high bending stiffness and low weight. In order to select the most efficient geometry, the moment of inertia divided by area of each spoke geometry was compared. The MATLAB script used to perform these calculations can be found in Appendix C.2. The load case for the wheel center in cornering is shown:

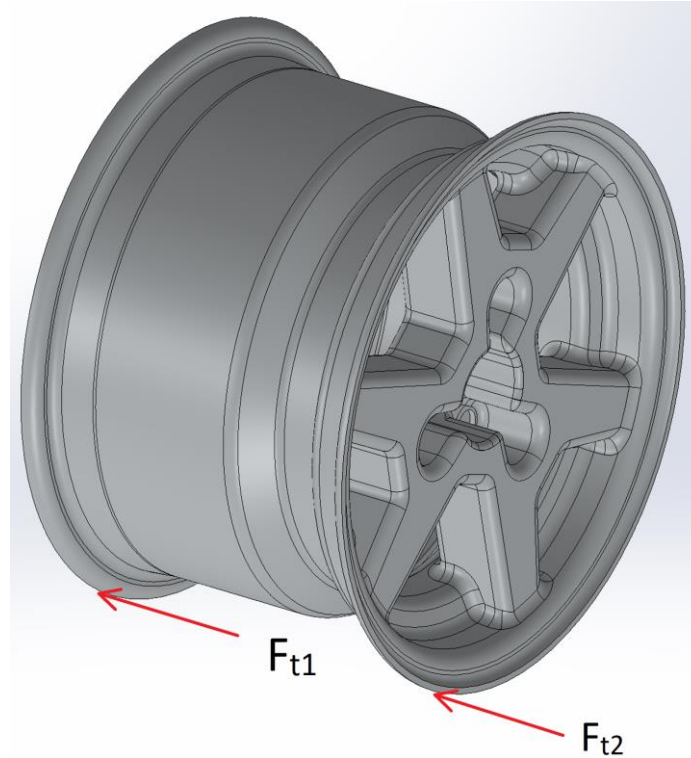


Figure 37. Wheel cornering loads

The cross-section geometries considered were flat plate, U channel, round tube, and square tube. These cross-sections are shown below.

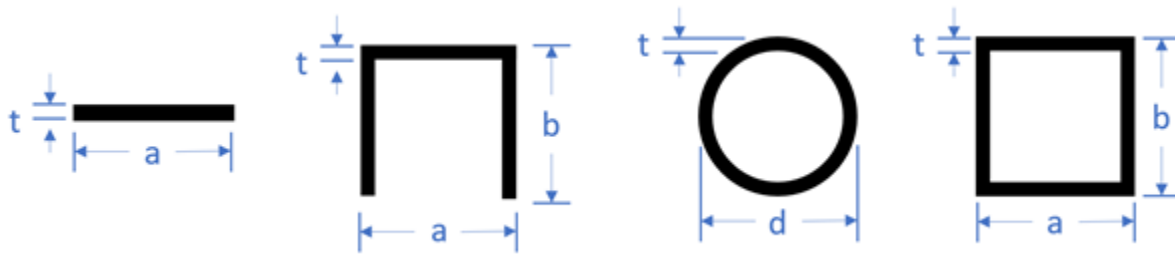


Figure 38. Spoke Geometries. Plate (Far Left), U-channel (Left-Center), Circular Tube (Right-Center), and Square Tube (Far Right). For All Geometries $a=b=d=1"$, and $t=.1"$

The specific bending stiffness of these shapes was compared for a thickness of .10 inches, the predicted laminate thickness. The geometric stiffness was also evaluated from a range of .01 inches to .10 inches, to see if the comparative advantage of each geometry would change when the laminate thickness changes, however this did not change the results. The area normalized bending stiffness of each shape considered is shown in Table 11.

Table 11. Bending stiffness divided by area for spoke geometries

Shape	Ratio	Percent of Highest Case
	I/A	%
Plate	8.33e-4	0.1
U Channel	4.13e-1	65
Circular Tube	4.75e-1	75
Square Tube	6.34e-1	100

The square tube was the most specifically stiff in cornering and was therefore selected. The manufacturing challenges and design solutions for this geometry are discussed in the tooling section. See Appendix C.4 for analysis script.

Spoke vs. Plate Analysis

Once the most structurally efficient cross sectional spoke geometry was determined, a preliminary plate and spoked center design were modeled to compare relative specific stiffnesses. The overall structure is stiffness driven, so normalizing this by mass determines what the most efficient geometries are. For each type of center, a special laminate was designed for the load paths in the respective geometries. All dimensions were approximated from a 10" Keizer barrel geometry. This served as a preliminary analysis to guide subsequent FEA comparisons between center designs of greater complexity.

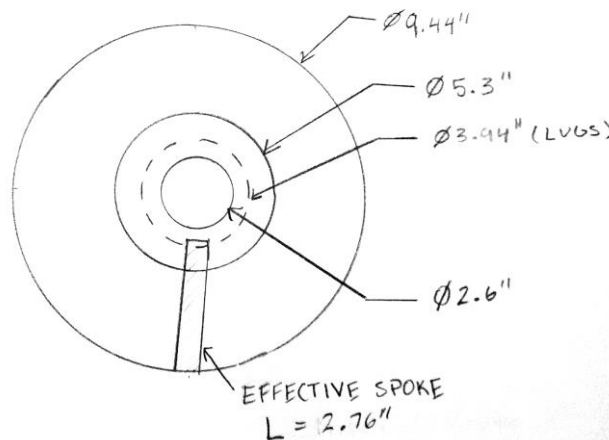


Figure 39. Plate center dimensions and effective spoke length

Plate Center

The plate analysis features a plate with an OD of 9.44", and an ID of 2.6", as seen in Figure 39 above. A 12 ply, M46J uni quasi isotropic laminate was designed, allowing the use of isotropic plate theory to analyze deflection. The loading case selected involves an annular plate simply supported on the outer edge, with a circumferential line load applied at the same radius the lugs

are located. The simply supported edge represents a rigid interface with the rim, and the line load represents the reaction at the hub connection.

Case no., edge restraints	Boundary values
1. Outer edge simply supported, inner edge free	$M_{rb} = 0, \quad Q_b = 0, \quad y_a = 0, \quad M_{ra} = 0$ $y_b = \frac{-wa^3}{D} \left(\frac{C_1 L_9}{C_7} - L_3 \right)$ $\theta_b = \frac{wa^2}{DC_7} L_9$ $\theta_a = \frac{wa^2}{D} \left(\frac{C_4 L_9}{C_7} - L_6 \right)$ $Q_a = -w \frac{r_o}{a}$

Figure 40. Isotropic plate theory for center plate analysis

Spoked Center

For the spoked center analysis, the inner and outer rings that would exist were assumed to be rigid. Therefore, an effective spoke length was created that extends half-way through the inner ring, and to the outer edge of the plate. This can be seen in Figure 40. Next, the same total load (divided by the number of spokes) used in the plate analysis was resolved to a single spoke. This allowed for beam bending calculations to be performed to determine the deflection of the center, assuming load is equally distributed across the spokes. A three spoke center was used as a conservative assumption. The laminate designed was [0c/-45/45/0/0]s with M46J uni and HTS40 cloth. The loading path of the spokes are along the lengths, so it is ideal for a 0-degree unidirectional fiber dominated laminate. However, cloth was placed on the outsides for ease of manufacturing, as well as overall durability of the laminate. 45's were placed to account for any potential torsion, which was anticipated to be seen in future models. It was placed in this laminate for a conservative modulus along the load path. The spoke cross section used was a 1"x1" square tube, from the earlier cross section analysis. 1"x1" was used as a conservative assumption, since that was expected to be the minimum dimension of a future spoke design.

1 Cantilever—end load

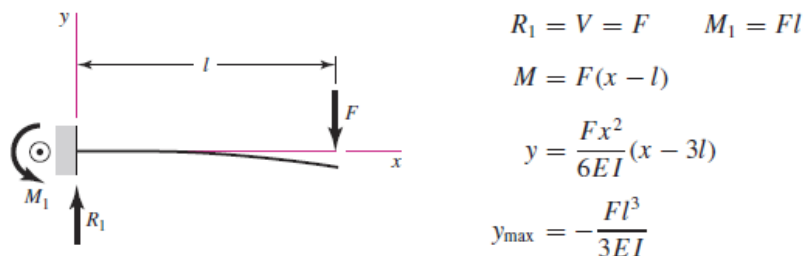


Figure 41. Spoke beam theory

Conclusion

As seen in Table 12 below, a quasi-isotropic plate only had 24% of the specific stiffness of a

preliminary spoked center. Now, it was understood that this didn't take into account a more complex plate design with channels or core to increase stiffness. This analysis also assumed there is rigid load transfer from the spoke to the hub connection and outer rim, which proved difficult to achieve in detailed analysis. Besides structural considerations, brake heating was a concern. Brake temperatures reach about 580 F at 3 inches away from the rim surface. According to data sheets, the TC 250 resin system in the prepreg used has a Tg of 285F. A good rule of thumb is to remain 50 F below the Tg in order to prevent degradation of mechanical properties. Rim temperature testing was planned on the 2016-2017 car, however engine issues prevented testing during the design season. The temperature effects of plated center airflow restriction was therefore not well understood, so pursuit of a more complex plate design was discontinued from further consideration. See Appendix C.3 and C.4 for analysis scripts.

Table 12. Plate-spoke comparison

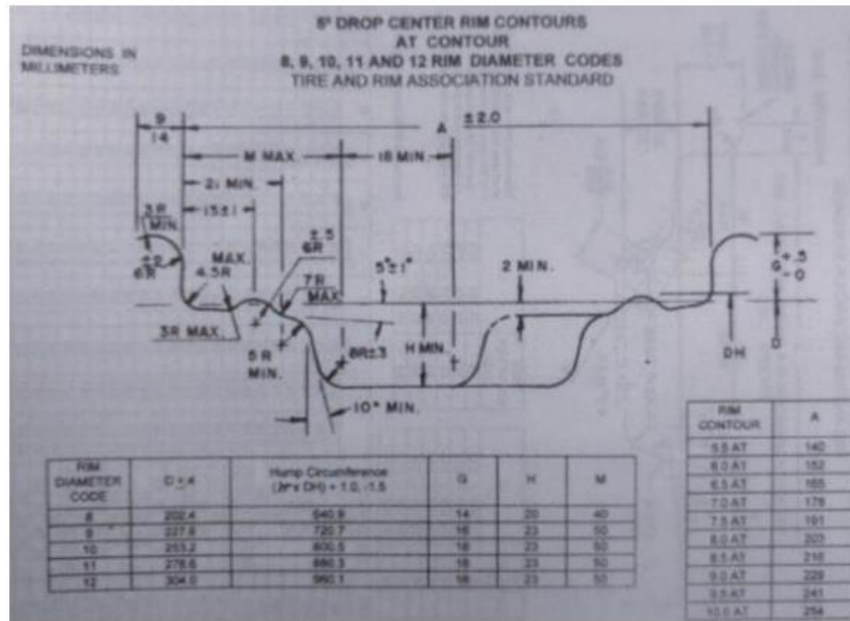
Center Type	Laminate	Laminate Flexural Modulus (Efx)	Laminate Flexural Modulus (Efy)	Specific Stiffness	Percent of Highest Case
		(Msi)	(Msi)	(lbf/in*lbm)	%
Plate	Quasi Iso	11.8	8.7	5.08E+03	24
Spoke	[0c/-45/45/0/0]s	8.54	7.1	2.1E+04	100

Spoke Number

A convergence of specific stiffness with increasing spoke size was attempted, however found to be unreliable without considering the structural effects of the overall wheel. Instead, the spoke number decision was made based on the load paths seen on a wheel. As mentioned earlier, load is transmitted from the tire contact patch through the bead, and eventually reacted at the hub connection. In order to minimize the deflection in a structure, it is advantageous to shorten the load path as much as possible. In the context of a wheel center, designing a spoke pattern that is in line with the lug pattern achieves this concept. Therefore, the initial decision was for the wheel to have three spokes, based on analysis in the hub connection section.

Barrel Shape

A conical barrel was considered in order to decrease center diameter and effectively stiffen the wheel. However, as the decision to move towards a 10" wheel was made, a conical barrel was not feasible due to packaging limitations. Therefore, the wheel featured a straight barrel, with rim profile and dimensions as specified by the Tire and Rim Association yearbook for a 10" tire. Below is an example of a rim specification -- this publication was also used to determine and implement standard valve dimensions.



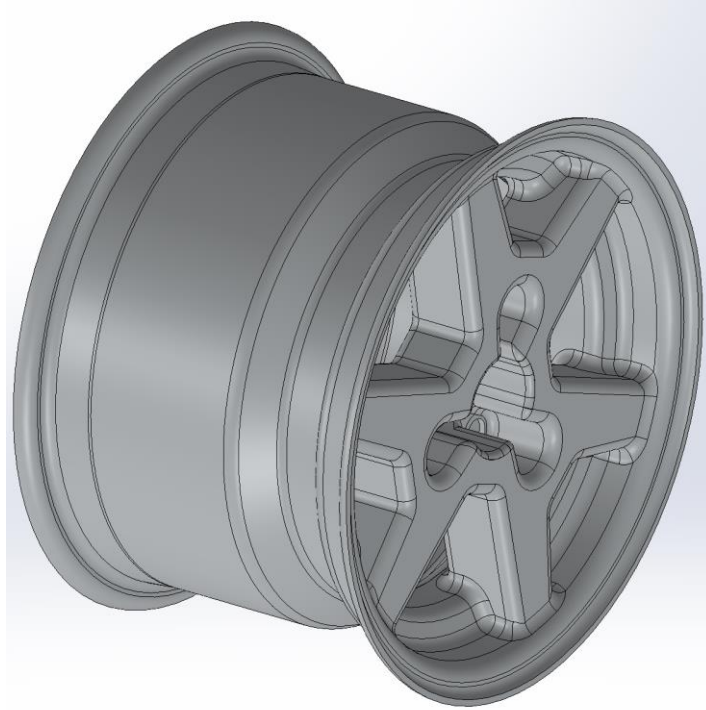


Figure 43. One-piece design

Two Piece

The two-piece wheel may consist of either a one-piece barrel bolted to a composite or aluminum center, or it may consist of a split-barrel design where the wheel center is co-laminated with one of the barrel sections. In either case the stiffness of the wheel is reduced due to the bolted joint, and wheel weight increases. U channels would be used in this concept, since a hollow spoke would cause equal manufacturing difficulty to that of a one piece. Sealing the halves would also require a gasket or silicone seal. However, two-piece wheels pose reduced risk mounting tires, since the wheel can be assembled around the tire. A standard two-piece composite wheel construction is shown.



Figure 44. Two-piece concept design. Source: Corvus Aerospace

Three Piece

Finally, a three-piece wheel featuring a two-piece barrel and separate wheel center was considered. In terms of advantages and disadvantages, this is very similar to a two-piece design. However, there is extra carbon weight at the connection, and another surface would need to be sealed compared to a two-piece wheel. Because this three-piece construction would not be easier to manufacture and does not provide advantages over a two-piece wheel, it was discontinued from further consideration.

Selection

Quality function deployment (QFD) was used to select between the one and two-piece designs. The QFD is shown in Appendix B. Due to the added fastener weight, structural deficiencies, and added gasket complexity a two-piece wheel introduces, the one-piece wheel was selected. It was projected that the fasteners required for a multiple piece wheel would be approximately 0.4lbs. This alone would account for 13% of the 3 lb wheel weight target. Therefore, even if a multiple piece wheel did not introduce stiffness loss, the weight alone was enough to move away from such a design. The hollow-spoke design poses additional manufacturing challenges, however. Manufacturing considerations are discussed in further detail in the manufacturing section.

Preliminary Geometry Selection Summary

Based on the discussed tradeoffs and preliminary structural analysis, a one-piece wheel with the following component geometries were selected.

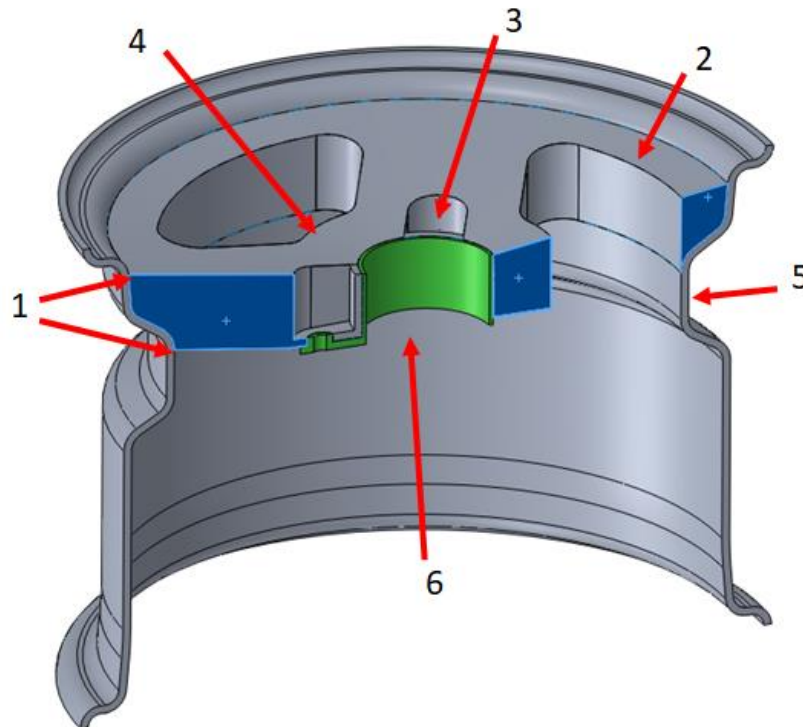


Figure 45. Preliminary wheel summary

1. Three rectangular section non-tapered hollow spokes. As shown, the spoke begins at the wheel offset plane to avoid any packaging interference with inboard components. It then ends at the outer edge of the bead seat, to maximize the direct load transfer from the bead seat.
2. Variations of rim bracing were noticed in preliminary research, and it was predicted that this could stiffen the un-spoked sections of the rim. Therefore, it was included in the preliminary design, and its effects studied in detailed analysis.
3. To reduce risk and increase strength, pure carbon stackups were favored at the carbon interface with the lugs. However, there was large potential for stiffness loss due to plate bending in this section. To minimize this, the thickness of the carbon was oversized, and spokes were 'forked' around the lugs to reduce unsupported plate area.
4. Extra hollow bracing around the center ring was added to help increase stiffness in this section. True effects are analyzed in detailed design.
5. Rim drop down as specified by TRA to help facilitate tire mounting.
6. Full center insert bonded at the center locating ring, and the hub side face of the wheel. The insert has extrusions for lugs to pass through to protect the carbon from over torqueing. The plating on the hub face also protects from surface damage due to edges of the hub.

Composites

Fiber reinforced plastic (FRP) composite materials typically achieve specific stiffness and strength 50-70% higher than that of aluminum and steel. Unidirectional fibers are particularly effective at reinforcing sections to transfer load in a single direction. Because FRP composites are orthotropic, the laminate may be tailored to more effectively reinforce sections of the wheel based on the load conditions for each section. The modulus can be changed by adjusting the number of plies and their orientation in the laminate.

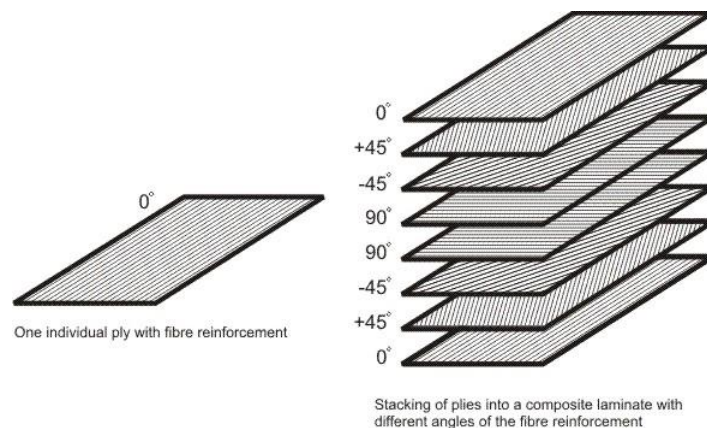


Figure 46. Example laminate

Since there is a massive number of stacking sequences and fiber orientations, requirements were set to reduce the number of laminate iterations in FEA.

The first aspect of composites considered was manufacturing. Most of these determinations were based off of prior experience manufacturing composites with Cal Poly Racing. Plies were

to be cut by hand, therefore only 45, 90 and 0-degree orientations were considered. A 45-degree unidirectional ply is difficult to lay up on a complex contour, so this was omitted from the rim. Lastly, the first ply of either the center or rim was cloth. The first ply is typically the most difficult to laminate, and cloth provides the easiest time doing this. This also increases impact resistance of the laminate from any dropped tools or small rocks which are kicked up during driving.

Next, symmetry and balance within the laminate were considered. Just like the strength and stiffness properties are directional, so is the CTE. This is important because laminates that are asymmetrical warp due to the unbalanced thermal stresses during cure and part cooldown. A balanced laminate requires that for every positive angle, there must exist a negatively oriented counterpart of the same angle. Symmetric laminates require the laminate to be mirrored about the laminate midplane. This eliminated any odd numbered ply counts (unless the center ply was cloth) and required a -45 for every 45 used.

Lastly, load path through the part was considered. Since the center and rim are loaded differently, their laminates were modified accordingly. Plies oriented at 0 degrees typically improve bending and axial stiffness, while plies at 45 degrees are most efficient in torsion. In the event that multiple axial or bending stresses are present, both 0- and 90- degree plies are preferred. The rim sees hoop, bending and torsion loads, making 90, 0, and 45 degree plies required respectively. The center sees bending and torsion, so only 0s and 45s were used. As a rule of thumb, approximately 30% of fibers must be oriented in the non-loaded direction to stabilize the laminate. Otherwise a plate with fibers oriented in one direction crumbles under any out of plane load. The 0 direction is defined in the radial direction for the center, and along the width of the wheel for the rim.

Based on the discussed requirements, the following table of iterations was created as a starting point for analysis. Ply number is increased in subsequent sections as necessary, while monitoring the projected overall wheel weight.

Table 13. Preliminary laminates. Lowercase c denotes cloth, uni otherwise

Center	Rim
[0c/45/-45/0]s	[45c/90/90/0/0]s
[0c/45c/0/0]s	[45c/90/90/90/0]s
[0c/0/45/-45]s	[45c/0/0/90/90]s
[0c/45c/0/0c]s	[45c/45c/0/0/90]s

The carbon used was M46J TC250 unidirectional tape, and T300 BT250 cloth. These were chosen due to Cal Poly Racing donated material availability. As described in *Carbon Fiber Monocoque Chassis for Formula SAE and Formula SAE Electric Race Cars* (5), extensive ASTM standard material testing has been performed on these materials in the prior season.

T300 was not tested, but it was deemed acceptable to use HTS40/AS4 cloth test data. This is because T300 has similar fiber properties and was newer than the HTS40/AS4. Therefore, using these properties was conservative, as older material is more likely to have inferior properties. Table 14 outlines property values used for analysis. They are significantly lower than the data sheets, likely due to a combination of non-ideal storage and sample manufacturing conditions.

Table 14. Material properties used in analysis

Properties	M46J 12k unidirectional/T C250	Data Sheet (% Difference)	T300 3k 2x2 Twill/BT250	Data Sheet (% Difference)
E1 (msi)	28.77	25.3	6.7	-
E2 (msi)	0.78	69.5	6.7	-
G12 (msi)	0.47	15.8	0.54	-
G23 (msi)	0.21	-	0.2	-
v12	0.22	1.1	0.003	-
v23	0.87	-	0.87	-

Detailed Stiffness Analysis

After the preliminary geometry and laminate was set, detailed FEA was started. Since the wheel was assumed to be stiffness driven, stiffness analysis was performed first. Once the stiffness target was achieved, the model was post processed using a failure criterion for reserve factors on the wheel.

As introduced in the previous sections, the rim and center see different load paths and have different sensitivities to the overall system stiffness. Therefore, to optimize the laminate of each portion, laminate iterations were done by isolating each component. For example, when optimizing the center, the rim was made rigid. As a starting point, the initial total camber compliance budget (0.2 deg) at max cornering was evenly budgeted between the center and rim.

Throughout stiffness analysis, the max cornering case and respective pressures and pressure distributions were applied to the rim. The FE software used did not have an option for spatially varying loads, so 20 partitions were created across the circumference of the 80-degree pressure distribution. The pressures were then Riemann summed to find the pressure that must be applied at each partition. See Appendix C.1 for sample load calculations. The inner surface of the rim was imported to avoid a gap with the mating edges of the center. The bead radius used to calculate pressure distribution was adjusted by the thickness of the rim. Boundary conditions included a fixed constraint at the center insert bearing faces, roller support on the back face of

the insert, and a center ring constrained in Z and X. The center insert was kept rigid to isolate the rest of the wheel. It was switched to aluminum in the final stages of stiffness analysis. Meshing and deflection calculation is detailed in Appendix C.6 and C.5 respectively.

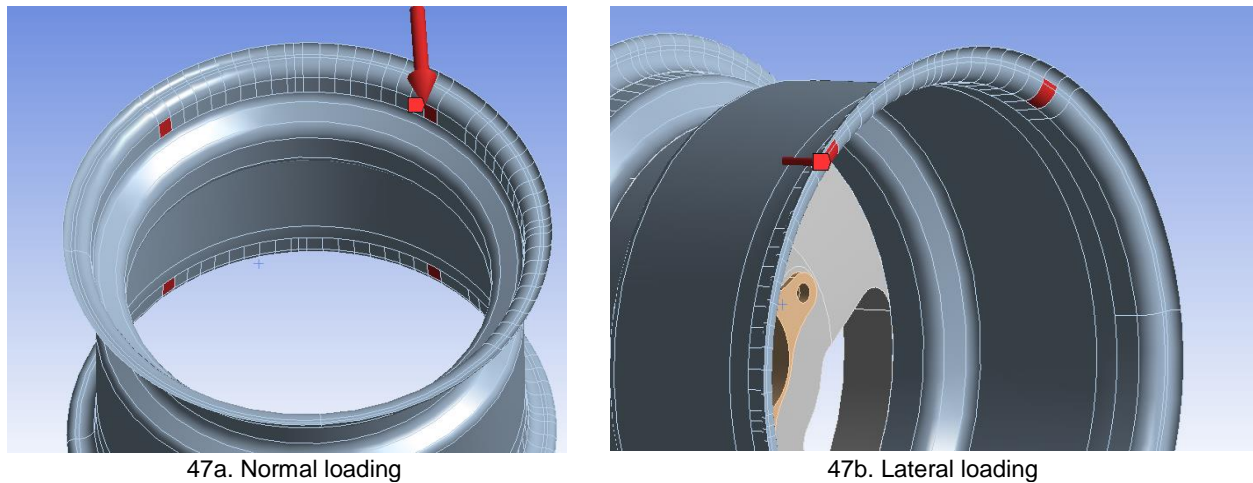


Figure 47. FEA load application

The rim was optimized first, while keeping the center rigid. Table 15 outlines the results of this analysis, with the highlighted row being the selected laminate. This was slightly above the allocated .1 degrees of deflection; however thicker laminates were abandoned due to brake caliper packaging.

Table 15. Rim optimization

Layup Schedule	Ply Number	Weight (lb)	Deflection (degrees)
[45c/90/90/0/0]s	10	1.31	.16
[0c/45c/90/90/0/0]s	12	1.58	.134
[45c/0/0/90/90/90]s	12	1.58	.103
[45c/0/0/0/90/90]s	12	1.58	.11
[45c/90/90/90/0/0]s	12	1.58	.131
[45c/0/90/0/90/90]s	12	1.58	.104

Next, the center was isolated by making the rim rigid. During this analysis, it was realized that a rigid rim artificially stiffened the center by forcing load through all the spokes. The load path drastically changed as the entire system was made elastic and caused stiffness to be lost in one of the spokes. Therefore, the results of these iterations were invalid. Regardless, when the combined system was analyzed with a 10-ply center laminate, the wheel deflected 1.54 degrees. This was about 7 times the stiffness target, which no amount of reasonable laminate iteration could remedy. Therefore, further geometry iteration was necessary.

Upon closer inspection of the center deformation, one can see significant plate bending at the interface with the lug bore and the center insert to the hollow center bracing. In order to stabilize the laminate, the spoke was first split along the center, and the hollow center bracing was drastically reduced. For quicker geometric iterations, the rim and center were held constant at .125" and .1" of aluminum respectively. The center insert was kept rigid, and the same boundary conditions of the previous analysis were applied. 100 lbs was applied at the lateral loading partition along the bead seat, and vertical deflection at the rim was used as a relative stiffness metric.

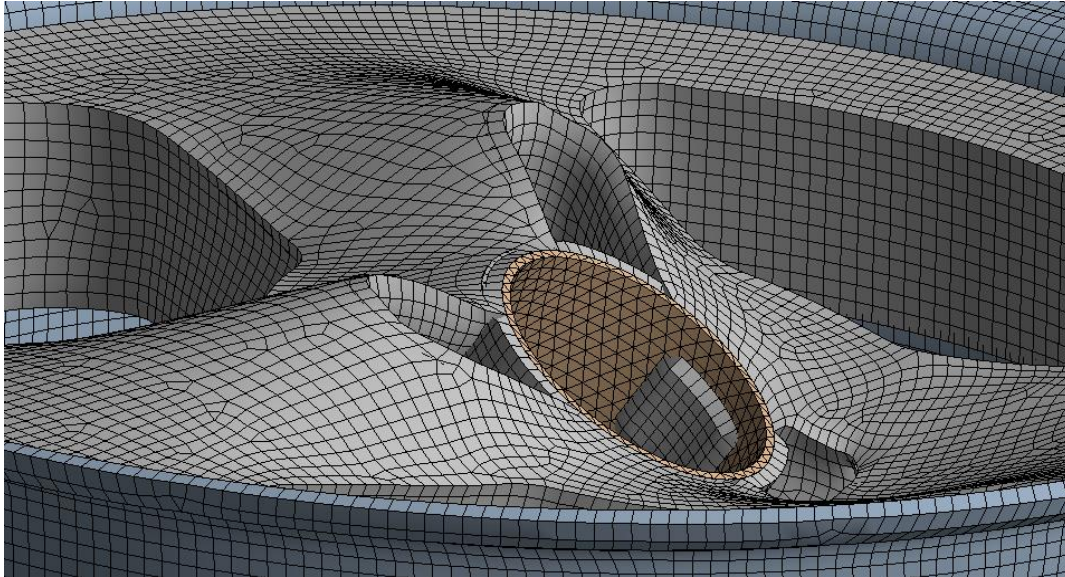


Figure 48. Plate bending at lug bore interface

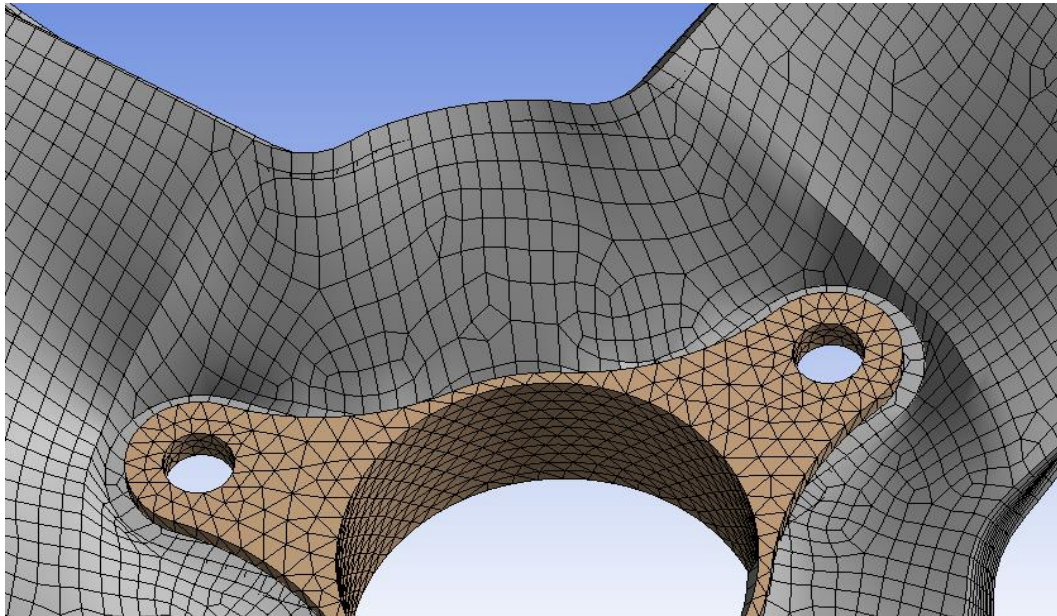


Figure 49. Plate bending at hollow center bracing

In order to normalize the results by mass, total surface area of the iteration was multiplied by the vertical deflection. Therefore, this number was minimized. As shown in the graph below, the structural efficiency of the aluminum version of the wheel was increased by 42% after the final geometric iteration. Details of each iteration are discussed below:

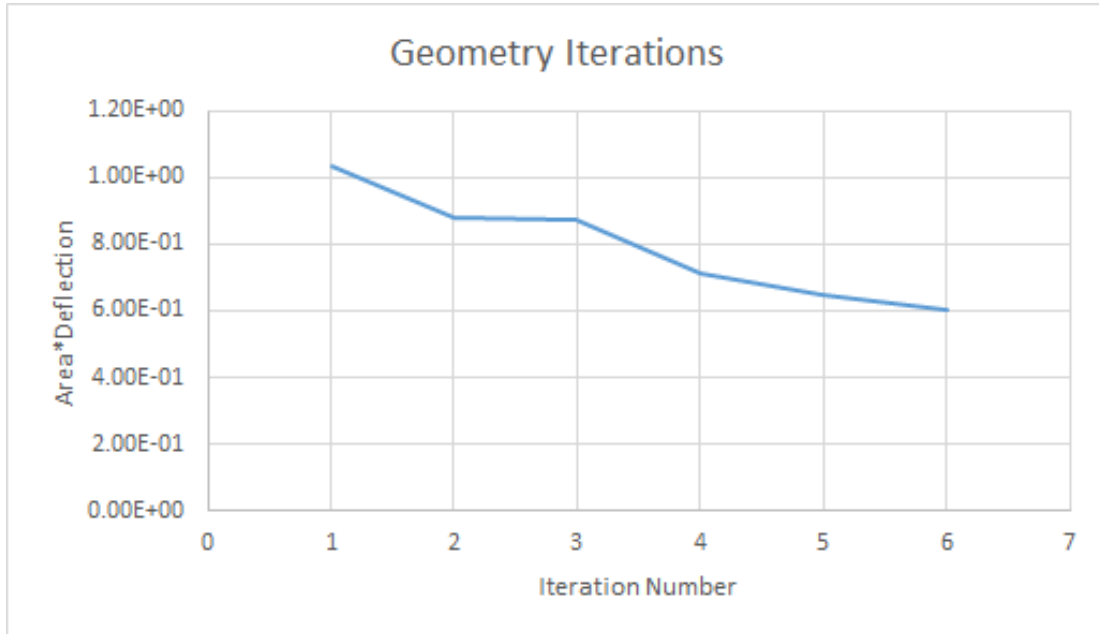
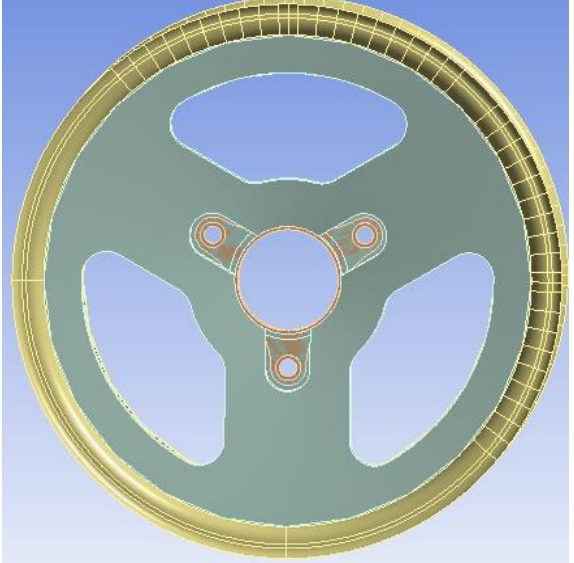
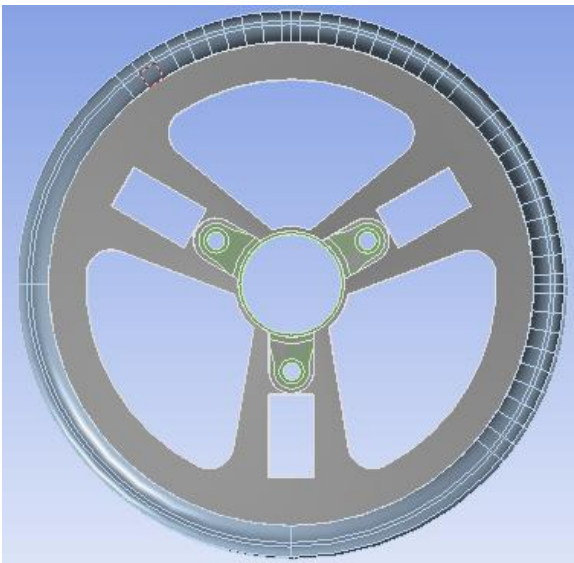
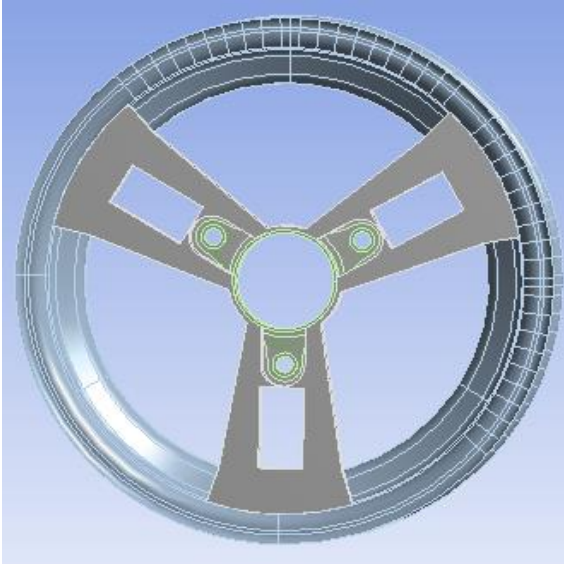
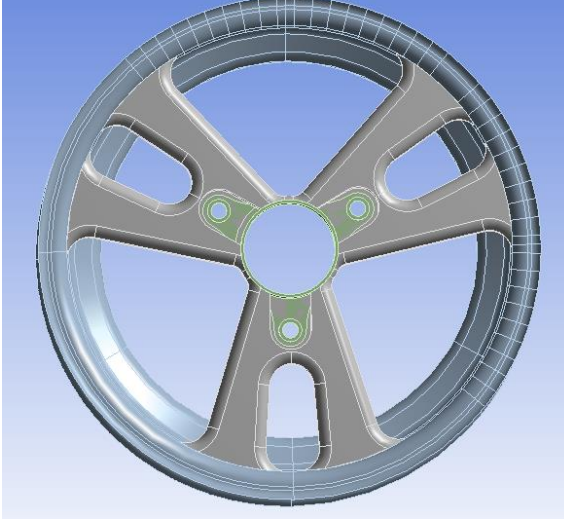


Figure 50. Geometry iteration structural efficiencies

Table 16. Geometry iterations

	<p>Geometry 1</p> <p>Original preliminary geometry.</p>
	<p>Geometry 2</p> <p>Structural Efficiency Increase Relative to Original: 15%</p> <p>Spokes split along the center to stabilize skins, and hollow bracing around center bore removed.</p>

	<p>Geometry 3</p> <p>Structural Efficiency Increase Relative to Original: 16%</p> <p>Bracing around the rim removed. There was a slight stiffness loss, however the reduction in surface area resulted in a slight efficiency gain. This also makes manufacturing significantly easier.</p>
	<p>Geometry 4</p> <p>Structural Efficiency Increase Relative to Original: 30%</p> <p>Fillets added and angle between spokes set to 85 degrees. It has been decided that the only geometric feature that required optimization at this point was spoke angle.</p>

	<p>Geometry 5</p> <p>Structural Efficiency Increase Relative to Original: 37%</p> <p>Angle set to 75 degrees.</p>
	<p>Geometry 6</p> <p>Structural Efficiency Increase Relative to Original: 42%</p> <p>Angle set to 58 degrees so that the centerline of the spoke is approximately at 60 degrees. Iterating spoke angle any further will give artificial results. This was decided to be the final major geometric iteration necessary before reintroducing composite analysis.</p>

Prior to rebuilding the model with the new geometry, more fillets were added for manufacturing feasibility and stress concentration relief. The lug bore was also made circular for more spacing to remove internal spoke tooling.

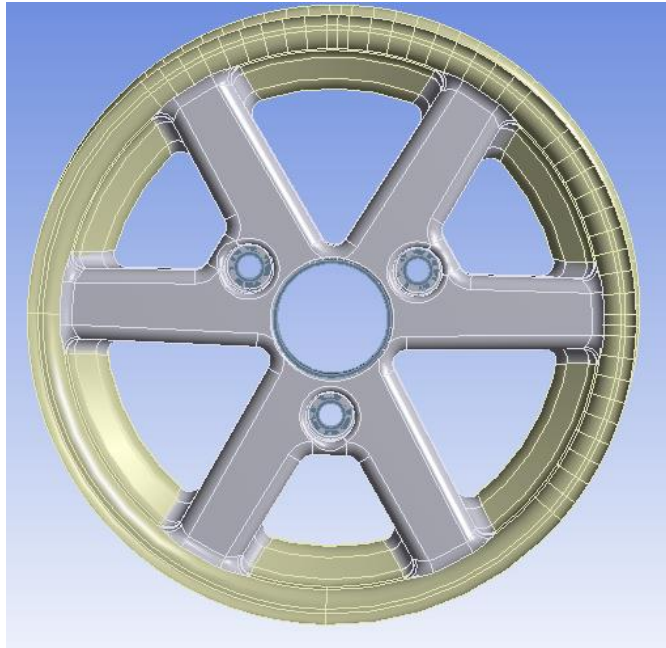


Figure 51. Final geometric detailing

To remove the internal tooling, slots in the center ring bore were required. Partitions were created for this section as shown below and defined with a custom material of miniscule modulus.

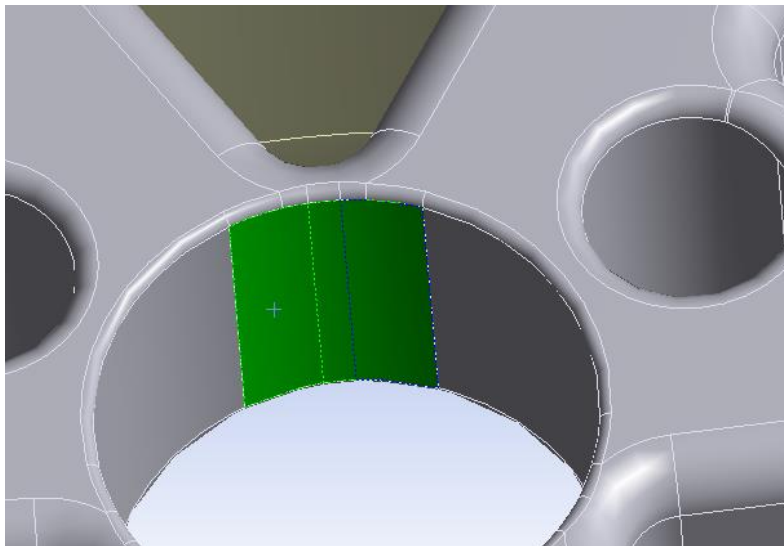


Figure 52. Slot partitions

Composite analysis was reintroduced, and the following laminate iterations were run through the maximum cornering case. The center insert was made aluminum for this final stage of analysis. The rim was kept constant throughout, at the previously selected laminate. As seen below, different laminates for the top and bottom faces of the spokes (vertical faces) and the faces parallel to Y were experimented with. Originally, it was thought that zero-degree plies would be far superior in order to carry bending. This was used as an initial probe of sufficient laminate thickness to hit the stiffness target. However, 45-degree plies dominated the stiffest iterations, implying torsion was primarily occurring. This made sense considering that the wheel was oriented such that load is applied in between the spokes, as a conservative assumption. The stiffest laminate was just under the .1 deg/g stiffness target, at .096 deg/g. This stiffness study was performed with the old 2.4 g max cornering case, which was later revised to 2.7g's. This shouldn't make a difference for stiffness considerations, since the model is linear. The higher loading case was used for subsequent strength considerations. A 14-ply laminate was at a thickness of .16", and a laminate any thicker may have posed manufacturing related issues when trying to laminate tighter radii. Therefore, the highlighted laminate was selected as the stiffness driven center laminate.

Table 17 . Center optimization

Center (Vertical faces)	Center (Horizontal faces)	Weight (lb)	Deflection (deg)
[0c/0/0/0/0]s	[0c/0/0/0/0]s	2.44	.4
[0c/0/0/0/0]s	[0c/45/-45/45/-45]s	2.44	.3
[0c/0/0/0/0/0]s	[45/-45/45/-45/45/-45]s	2.58	.28
[0c/0/0/0/0/0/0]s	[0c/45/-45/45/-45/45/-45]s	2.71	.25
[45c/45/-45/0/0/0/0]s	[0c/45/-45/45/-45/45/-45]s	2.71	.23
[45c/45/-45/45/-45/0/0]s	[0c/45/-45/45/-45/45/-45]s	2.71	.23
[0c/45/-45/45/-45/45/-45]s	[0c/45/-45/45/-45/45/-45]s	2.71	.24

Detailed Strength Analysis

Once a laminate and geometry were determined based on detailed stiffness analysis, the current design was checked for failure across all predicted loading cases. The composite failure criteria selected was Tsai Wu, as it is the most general criteria and accounts for interaction of stress in multiple directions. The 6061 aluminum center insert was checked for a minimum factor of safety of 1.2.

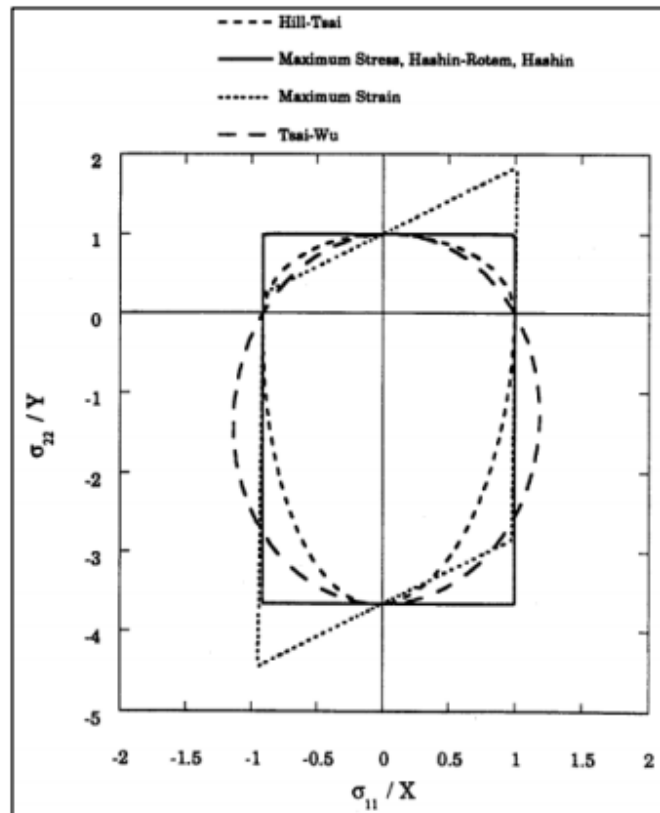


Figure 53. Comparison of failure criteria

Failure was analyzed through a post processor directly linked to the original stiffness analysis. One simply has to select the desired failure criteria, and the RF (Reserve Factor) is plotted on the wheel. A reserve factor of 1 signifies failure.

The laminate for these iterations was switched to [0c/45/-45/45/-45/45/-45]s all over the center. This was done to increase strength at the slight cost of stiffness. This still put the wheel right on target, at .1 deg/g. The following critical loading cases were analyzed:

Table 18. Strength analysis results

Loading Case	Lowest Reserve Factor	Center Insert FOS
Combined	.8	1.42
Max Cornering	.89	9.72
Tire Seating	1.08	-
Bump	2.9	1.46

Table 18 shows failing reserve factors for most of these cases, however the plots brought suspicion to these values. The minimum value was often a single element surrounded by elements with reserve factors of 3 and 4. Another source of error was that the bottom of the lug bore was modeled as an extended edge without a radius. This created a sharp corner with the hub mating face, that caused low reserve factors in that area. In a reality, there was a radius there to relieve any stress concentrations.

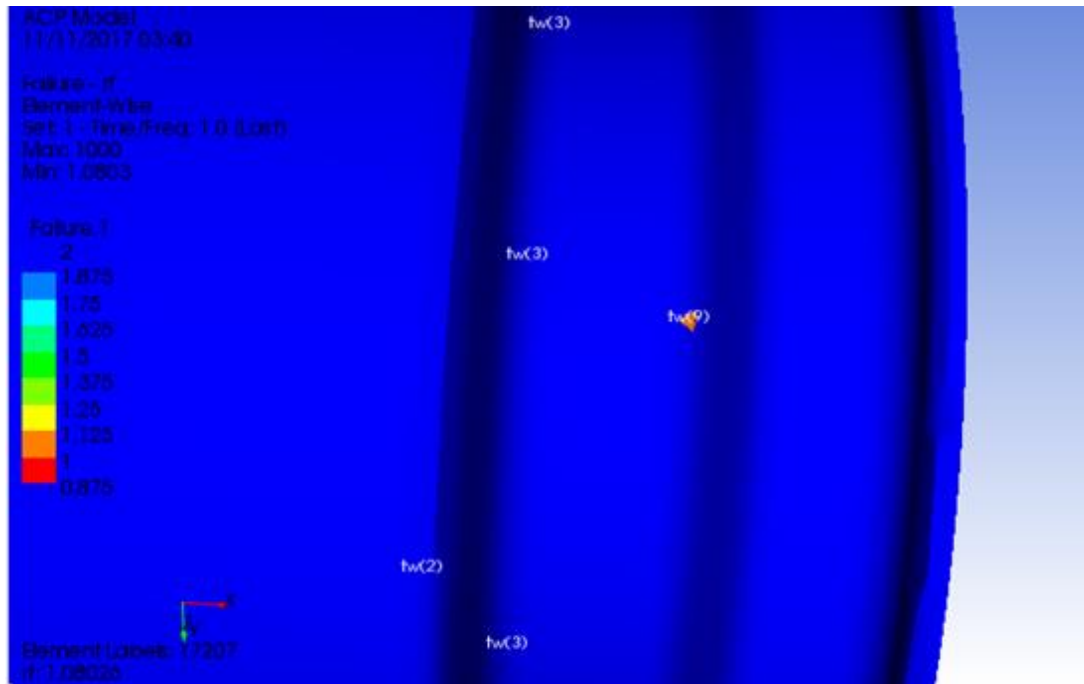


Figure 54. Suspicious reserve factor minimum

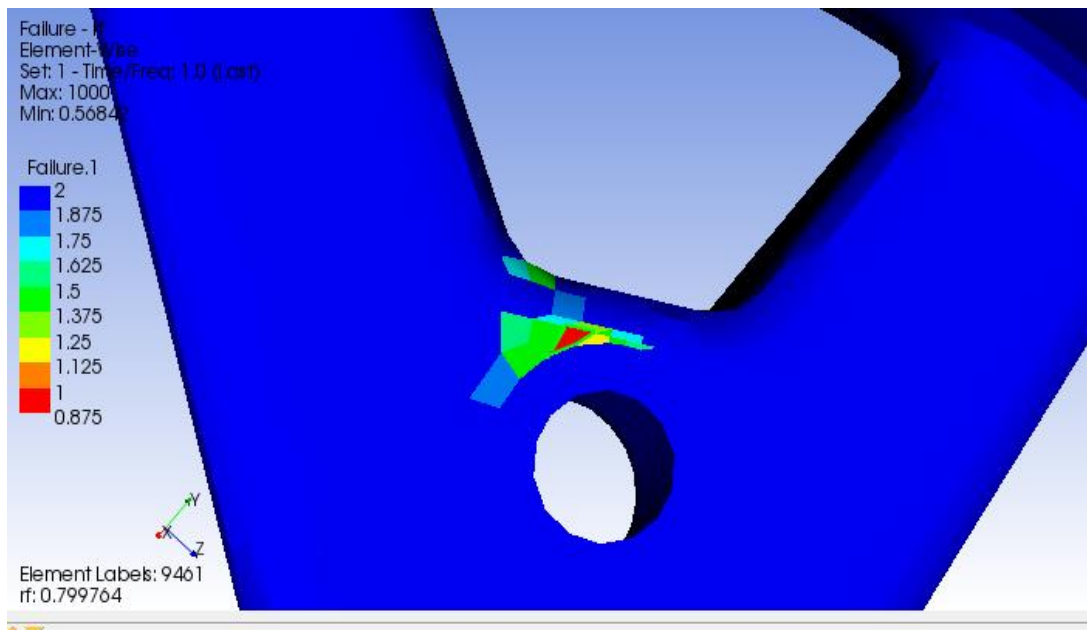


Figure 55. Artificial lug bore stress concentration

Not taking into account suspicious elements, the reserve factors were approximately 1.3-1.4 for all critical loading cases. The center insert also had a minimum factor of safety against yield of 1.42.

Post Manufacturing Trial Analysis

Various minor geometry changes were made after the manufacturing trials mentioned in the Manufacturing Tests section. Therefore, further analysis was required to ensure performance targets were still met.

Using the same model, we found that the manufacturing trial changes resulted in approximately a 14.5% increase in camber compliance, putting the wheel just above the camber compliance target of 0.1 deg/g. Most of the loss was attributed to the expansion of material directly around the center locating bore for manufacturability. This change allowed for greater plate bending around a center bore that is fixed in plane.

Since there was still leeway with our mass target, we added 2 plies of zero direction uni to the center in order to stiffen the system ([0c/0/45/-45/45/-45/45/-45]s). Addition of material to the barrel was avoided, due to its large surface area having a greater effect on mass increase. This iteration resulted in an overall mass of 2.82 lbs and 0.094 deg/g, a 2% increase in specific stiffness.

Strength analysis results remained similar to that of the previous iteration. Overall there is suspicion over the “failing” reserve factors, with the vast majority of the wheel featuring high reserve factors. Areas in question were to be subject to close inspection during physical strength testing and reinforced accordingly. Further detailed strength analysis was deemed not worth team resources, for the level of confidence such an analysis would provide.

Detailed Analysis Summary

The final wheel design came out to 2.82 lbs, which was .18 lbs under the 3 lb target. This took into account the center insert, and a 5% markup due to ply overlap during manufacturing. Final stiffness was 0.094 deg/g, under our 0.1 deg/g target.

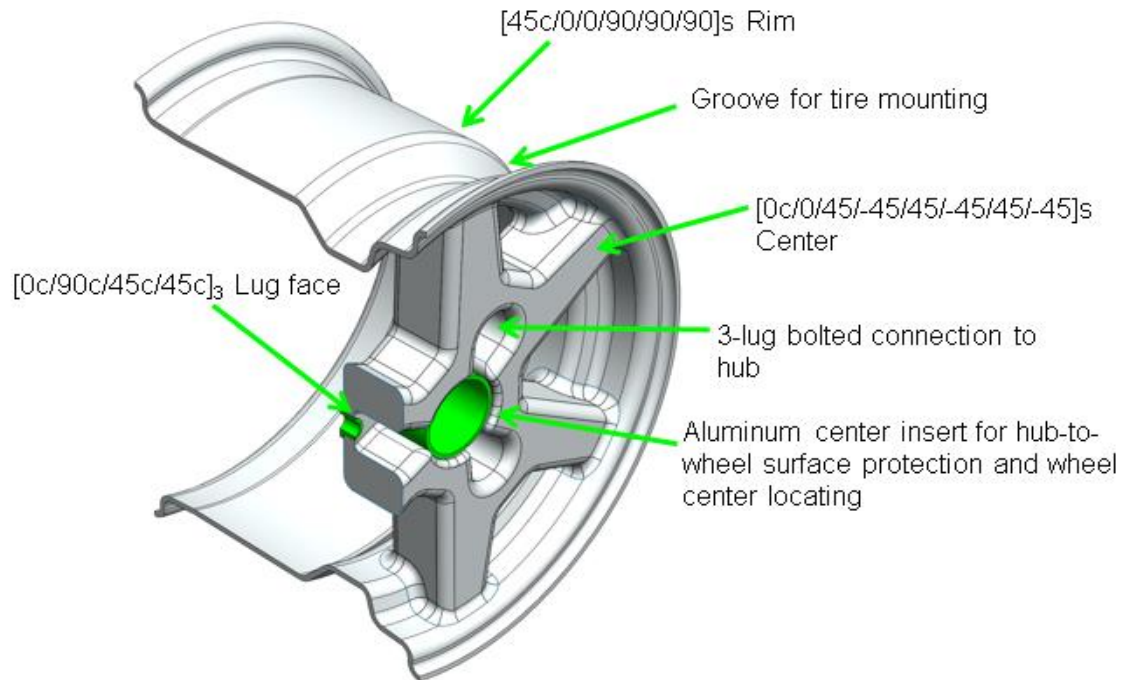


Figure 56.Final wheel summary

Valve

The TR-413 valve was selected. The valve was selected for its low cost (about \$1 each), small size and high temperature resistant brass core. A .453" (11.5mm) hole was located in the barrel, equidistant between two spokes, in order to install the valve. The locating hole for the valve is shown.

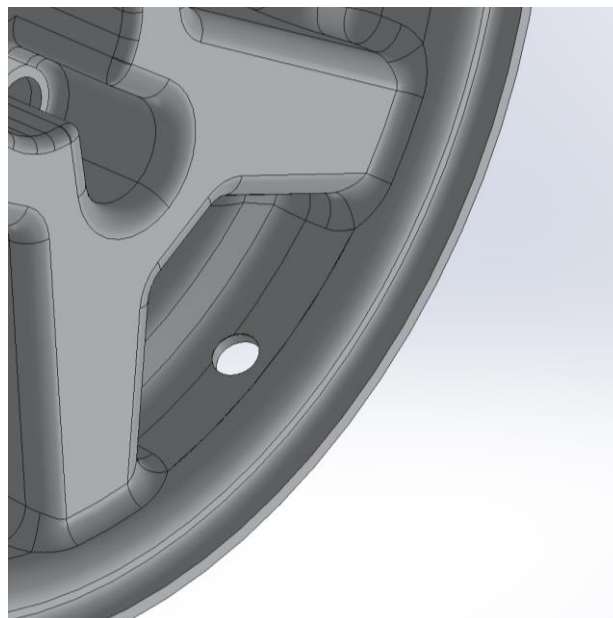


Figure 57. Valve locating hole

Manufacturing

The manufacturing processes selected were aimed at producing one wheel per week and a total production volume of 10 wheels. This production volume would provide two sets of wheels, one spare wheel, and one wheel for structural testing. While the production rate and volume were never realized, they played a crucial role in process and tool material selection and are still relevant to future manufacturing efforts.

Manufacturing Process Selection

Prepreg carbon-fiber was selected to manufacture the wheels. Prepregs allow precise control of fiber orientation and fiber content compared to wet-lamination and infusion techniques. Better control of fiber content and orientation result in improved structural efficiency and, therefore, lower weight. Furthermore, prepregs offer shorter cure times (4-6 hours) compared with infusion or wet-lamination processes, which typically cure for 12 hours or more for a laminate of this thickness. Prepreg also supports the use of coefficient of thermal expansion (CTE) driven pressure intensifiers (discussed in further detail in the next section) in order to produce hollow geometry, while infusion and wet lamination do not. Finally, Cal Poly Racing has various prepreg materials available through multiple sponsors. One key disadvantage of using prepreg material is that prepregs must be cured at temperatures ranging between 230 and 500°F. Elevated cure temperatures dramatically increase tool cost, and they require ovens or autoclaves for cure.

Tooling

Tooling Architecture

The tool consists of two male plugs which control the inner surfaces of the barrel, the spokes, and the hub face. This layout was selected because it is the only one which could produce a single piece wheel. One crucial limitation to this design, however, is that the bead seats are not controlled by a tool surface. Because it was unknown whether the bagging surface would provide a smooth enough surface to mount the tire after minimal sanding, the tool was designed so that a set of external rings could be bolted on during cure. One of the tool pieces is shown below.

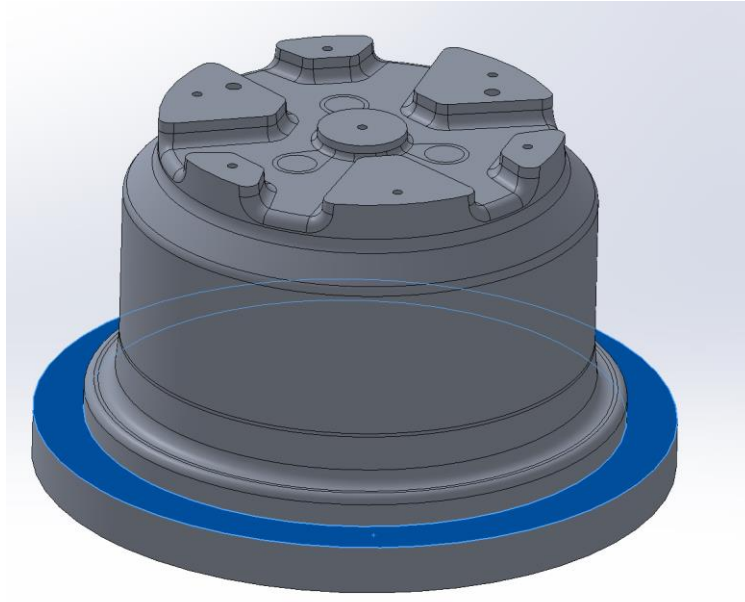


Figure 58. Internal tool section. Ring bolting flange highlighted

The clamshell rings described were never produced due to time considerations. However, the layout of the clamshell rings is shown in case they are deemed necessary for future manufacturing attempts.

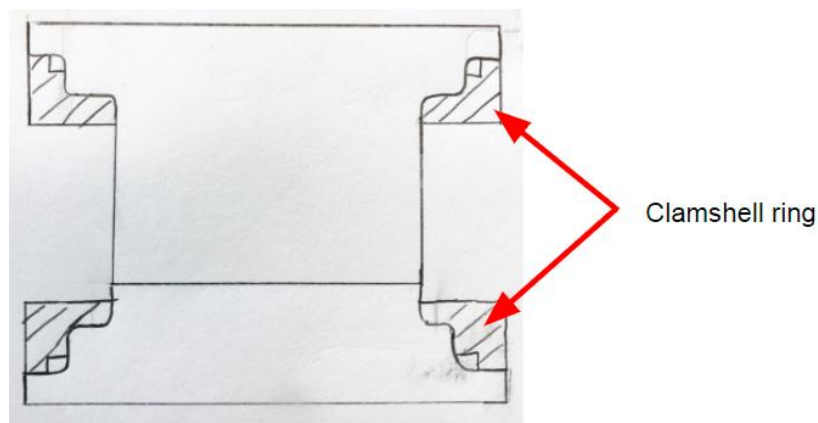


Figure 59. Clamshell ring diagram

Each ring could be constructed from several pieces of metal, plastic, or tooling carbon. The latter could be formed by laminating five to ten plies of carbon fiber over a completed wheel, using mold release or wax to prevent bonding between the completed wheel and the additional carbon. This method is particularly useful because it requires no machining, and it does not require the designers to predict the cured ply thickness of the laminate.

Material Selection: Overview

Aluminum alloy and Stratasys' Ultem 1010 plastic (a 3D printing material) were considered for tool materials. The criteria for material selection included tolerances, thermal considerations, cost, manufacturing timeline, production volume capacity, and cure temperature/time. The importance of each criterion and an outline of the comparative advantages of each material is included in the following sections.

Tolerance

The surface profile tolerance achieved on the mold directly affects the tolerance of the inner wheel surface. Since more accurate control of the wheel features is desired, a tool achieving tighter tolerances is preferred. Because the Ultem 1010 must be finished by hand, the surface profile is worse than the as-printed part. While the exact change in surface profile tolerance due to post-processing is not known, the printed tool is predicted to produce a wheel surface with surface profile tolerance of .125". By comparison, the aluminum tool may be laminated on without any post processing. Additionally, the surface tolerance of CNC machining is estimated at about .010" for a tool of this size (compared to approximately .050" for the as-printed Stratasys tool). The aluminum tool was predicted to produce a part with surface profile tolerance .075".

Coefficient of Thermal Expansion

When a carbon fiber reinforced plastic material is cured at high temperature, the mold and part materials expand, often at different rates. The relationship between the final size and initial size due to heating is:

$$L_f = L_i[1 + \alpha(T_f - T_i)]$$

L_f and L_i refer to the final and initial sizes of the tool respectively. T_f and T_i refer to the final and initial temperatures. Alpha refers to the coefficient of thermal expansion of the material, which is assumed to be linear for the range of temperatures used.

The expansion of the mold causes deviation between the modeled geometry of the part and the resulting shape. While tools can be scaled to compensate for thermal expansion, molds with lower thermal expansion are preferred because expansion of the tool can cause other issues such as bridging or resin pooling. For the temperature range of the cure (69 degrees at room temperature to 275 degrees for cure) aluminum exhibits thermal expansion of 14 microinches per inch degree Fahrenheit. Ultem 1010 exhibits expansion of 26 microinches per inch degree Fahrenheit in this range.

Thermal Mass

In order to achieve temperature increase or "ramp" rates desired for cure of prepreg resins, the tool's mass must be low enough that the heat input from the oven or autoclave will increase the temperature at the desired rate. Therefore tools with lower mass are desired. Aluminum's density is .098 lb/in³, and Ultem 1010's density is .046 lb/in³. However, printed tools typically feature hollow in-fills, so the effective density of an Ultem 1010 tool is predicted to be approximately .010 lb/in³.

Temperature Limit

Ultem 1010 has a temperature range of 400°F, and aluminum may be used to 500-600°F before softening occurs. Therefore, both are equally suitable to cure TC275-1 resin at 275°F.

Cost

Ultem 1010 tools are sponsored by Stratasys and therefore have no cost to the team. However, the delivered tools may not be laminated on as-is: They must be sanded and coated with tooling resin before parts can be produced. The cost of the Ultem 1010 tool was therefore estimated at \$100, which includes costs for sandpaper, tooling resin, and nitrile gloves. 6061 aluminum if purchased by the senior project team was estimated to cost \$1500 from a metal supply source.

Timeline

The timeline for completing each tool is broken down into its delivery and preparation time. The delivery time for the Ultem 1010 tool is estimated between 2-14 weeks: Stratasys has sponsored Cal Poly Racing with various printed materials and has delivered parts of similar print-time to this tool within two to three weeks of sending them completed designs. However, in the most recent case of one Ultem 1010 tool requested during June of 2017, delivery time was delayed to 14 weeks due to personnel changes within Stratasys, and delays in printer availability. The Ultem 1010 tools also require two weeks to post process (this time consists of sanding, resin application, and resin post-cure) before lamination begins. The aluminum tools have an estimated machining time of 2-6 weeks and do not require any post processing.

Production Capacity

Due to surface degradation, scratching, and thermal cycling, composite tools wear down over time and therefore have limited production capacity. While the exact production capacity of materials is dependent on tool size and geometry, several approximations can be made: Metallic tools typically support production of about 200 parts before standard wear causes marring of the tool surface. Stratasys indicates that the printed Ultem 1010 material does not have a thermal cycling limit, however tooling resin degradation typically occurs after about 40 cycles, at which point the tool would need to be refinished. Since the required number of parts for this project is 9 wheels, aluminum's higher production capacity does not offer a distinct advantage.

Material Selection: Summary

Table 19. Summary of the comparison between Ultem 1010 and aluminum

Property	Ultem 1010	Aluminum
CTE	26 uin/in	14 uin/in
Density	.046lb/in ³	.098lb/in ³
Tolerance (Profile)	0.125	0.075
Predicted Cost (To team)	100	1500
Timeline	4 to 16 weeks	2 to 6 weeks
Number of parts can be pulled	40	200

Based on each of these considerations, aluminum was the more suitable tooling material. Based on the high cost of aluminum, Cal Poly racing pursued sponsorship from Weber Metals, who provided two aluminum round blocks which were large enough to produce the tools.

Insert Design

Overview

In order to produce hollow geometry, expanding inserts were used in conjunction with a local clamshell tool section. A diagram of the expanding inserts is shown:

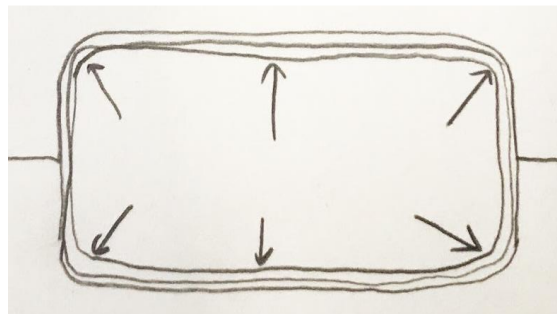


Figure 60. hollow spoke section

After cure, the expanding inserts could be removed through a hole in the wheel. Or, depending on the material used, may be dissolved by pouring a lye compound into the spoke. The tradeoffs between using removable silicone inserts and dissolvable ST-130 inserts are outlined in the following sections. Examples of silicone and ST-130 inserts are shown below:



Figure 61. Silicone insert (left) and ST-130 insert (right)

Removal

Using silicone inserts requires the placement of a hole at the base or barrel of each spoke. After cure, the inserts are removed through the hole, leaving a hollow section in the wheel. This method reduces the stiffness of the wheel design and reduces the design flexibility for the spokes: The spokes must be designed so that the silicone inserts can be removed through each of these holes, so the hole must be similar in size to the hollow section of the spoke. By contrast, the ST-130 inserts are dissolved after the cure is complete, and therefore do not pose any restrictions on the spoke geometry.

Thermal Expansion and Cure Temperature

The expansion of an insert is related to its coefficient of thermal expansion (CTE) of the insert and the cure temperature of the part. Higher cure temperatures and coefficients of thermal expansion result in more compaction and can accept higher variation in laminated ply thickness prior to cure. ST-130 has a coefficient of thermal expansion of 59-98 microinches per inch degree Fahrenheit (the CTE changes throughout its temperature range), and a maximum service temperature of 240°F. Silicone has a CTE of 150 microinches per inch degree Fahrenheit and a maximum service temperature of 500°F and therefore will provide superior compaction compared to the ST-130 tool.

Production and Removal Time

The silicone inserts are produced by pouring a two-part mix into a mold. Including the mold manufacturing and the pouring time, insert production is estimated to take a week. Because the ST-130 parts are sponsored by Stratasys, they are subject to the same lead time mentioned in the previous section, 4-16 weeks. Removal of the silicone is expected to take one to five hours depending on the complexity of the spoke geometry, whereas the ST-130 inserts take one week to dissolve.

Inserts: Summary

Table 20. Comparative advantages of the silicone and ST-130 inserts

Property	Silicone	ST130
CTE	150 uin-in	59-98 uin-in
Max Cure Temperature	500	240
Ease of Removal	Hard	Easy
Cost to Produce	\$200	\$0
Time to Produce	1 week	2 weeks-14 weeks
Time to Remove	1-5 hours	1 week

Silicone inserts are selected based on the study of the tradeoffs between silicone and ST-130. Therefore, the preliminary wheel design, shown in Figure 52 of the wheel design section, accommodates the removal of the silicone inserts by placing several holes at the wheel center.

Post Machining

After curing, one must set up the wheels in the VF3 and post machine the 4 holes for the center insert. A fixture is needed to clock the wheels repeatedly and a probing macro modified to probe off the center bore. The lug holes were to be drilled with a CoroDrill 854 drill bit in order to prevent fraying of fibers and delamination. The center bore was to be cleaned up slightly using a diamond cut router bit in order to better control the bond gap thickness, while post bonding the inserts in.

Center Insert Bonding

The center insert was to be bonded using Henkel high temperature epoxy based structural adhesive. Because the wheel lug insert holes are machined after the lamination process, the clearance between the insert outer diameter and the wheel hole inner diameter is predicted as .005", which is sufficient to achieve the required alignment between the wheel bead seat and the wheel center.

MANUFACTURING TESTS

First Manufacturing Test

Due to the high cost of machining a full-scale tool, it was important to test the effectiveness of using silicone plugs to compact the spokes prior to machining the full wheel mold. Molds which could produce one spoke were machined, and the spoke was laminated. Several uncertainties the manufacturing test addressed were the effectiveness of using silicone inserts to compact the laminate, mating the spoke sections, using a continuous "pinch" with no gap at the region halfway between spokes, and general difficulties with laminating complex geometry in deep channels. The molds used to produce the test piece are shown in Figure 62.



Figure 62. Hollow spoke test molds

Silicone Inserts

The silicone inserts were produced from OOMOO Liquid Rubber 30, two-part silicone. The silicone was mixed thoroughly, then poured into negatives of the desired silicone geometry. The silicone geometry was defined as the mold surface of the spokes offset inward by the cure-ply thickness of the laminate. Setting the offset equal to the cured ply thickness ensured maximum compaction during cure, but it also made the silicone inserts difficult to place in the mold once the part was laminated. The silicone inserts formed using this method are shown in Figure 63.



Figure 63. Silicone inserts

The silicone inserts were cut into smaller pieces in order to facilitate easier removal after cure. The theory was that after removing one piece, the remaining pieces would no longer be compressed. Removing the compression would then make other pieces much easier to remove. While splitting the pieces did make them relatively easy to remove, it also made them very difficult to place during the final steps of the lamination process. Figure 64 shows the inserts placed in the spoke.



Figure 64. First manufacturing test insert placement

Not all of the inserts could be pushed all the way to into the mold, and the top surface of the inserts did not precisely align. It was suspected that this may prevent even compaction of the laminate, so for the next test, the cuts were reduced to a minimum.

During the lamination process, it was realized that the inserts could not be removed through the center of the wheel as desired. Instead, the inserts had to be removed through a hole in the barrel. For this test, a hole was cut in the barrel section to remove the inserts. On the next test and subsequent wheel manufacturing, the hole was left open during lamination.

Compaction

With the exception of some unevenness due to cutting the silicone into many pieces, the silicone was effective in compacting the prepreg during cure. The surface quality of the resin was high (there were few pinholes, and no fiber discoloration), which is a strong indicator that compaction was high. Figure 65 shows a close-up view of the part's outer surface.



Figure 65. Outer surface of part from first manufacturing test

Pinholes typically form in the surface of the resin when the consolidation of the resin is poor. Therefore, the method of using silicone inserts was confirmed and used for subsequent manufacturing efforts.

Pinch Region

One section of the laminate required pinching plies of carbon together by closing a gap between the mold surface at the wheel center and the edge of each spoke. In practice, closing the gap between the mold surfaces by stacking plies of carbon was infeasible. As the gap became progressively smaller with each ply stacked against the vertical surfaces of the mold, it became more difficult to add plies. Because the plies are much thicker before debulking and final cure, it was impossible to add the desired number of plies. What resulted was a messy region of deformed fibers as the plies from the adjacent vertical surfaces contacted each other. Figure 66, below, show the pinch region as the plies began to come into contact.



Figure 66. Pinch region towards end of lamination process. Contact between plies circled.

Due to the issues forming the pinch, the wheel geometry was modified to leave a gap of 0.56 inches between the wheel center and outer spoke face.

Complex Geometry and Lamination Time

The final purpose of the manufacturing test was to determine any issues laminating the small and complex geometry, particularly the section around the lug boss. Laminating most of the wheel proved feasible, however the lug-boss region was very challenging and took about 40% of the total lamination time. Similar to the effect when attempting the pinch section, the gap between the lug boss and the other vertical faces diminished as plies were added. While the gaps did not completely go away as with the pinch section, the space became so small that it was impossible to fit fingers in between the plies and form the carbon effectively. Figure 67 shows the lamination of the lug-boss section.



Figure 67. Lug boss lamination

The spoke took 17 hours to laminate and bag for cure. One hour of this process was spent placing inserts, then bolting the tools together and bagging the part. Of the remaining 16 hours, 40% was spent laminating the lug boss, and about 35% was spent and trimming plies.

Insufficient Fiber Wetting

In addition to the expected challenges producing the spoke, there was a severe issue with the fiber wetting which destroyed the part. The part deteriorated when trying to pry it from the mold. Plies of carbon delaminated and then crumbled away when force was applied, which showed that the resin had not wet-out the fiber. Additionally, the top surface of the part separated from the rest of the laminate. Figure 68 shows the delamination failure of the top section of the part.

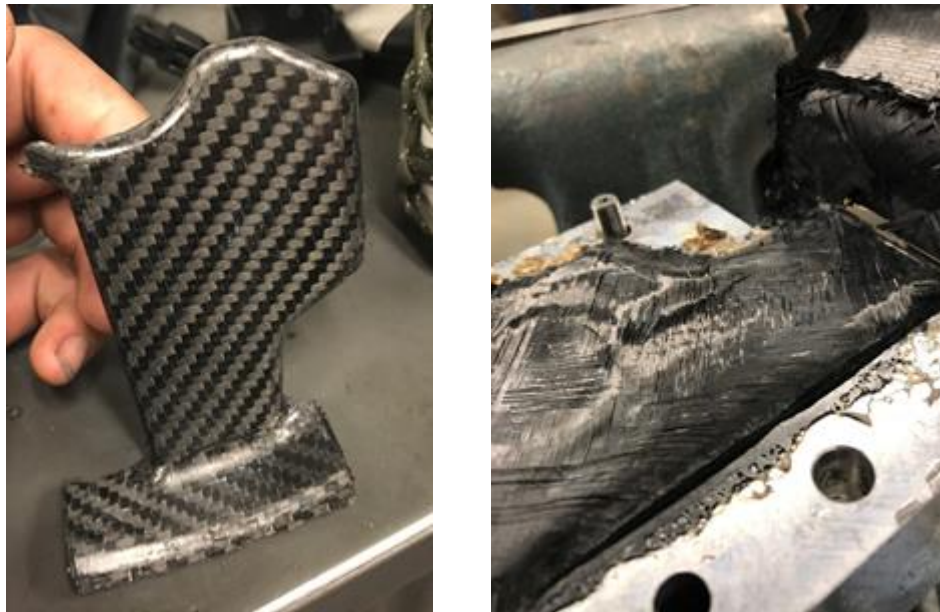


Figure 68. Delaminated Section. Mold Surface (Left), Delaminated Fiber Surface (Right)

The most significant signs of insufficient fiber wetting were the delamination of the top plies, and the loose fibers visible on the fiber surface.

Geometry Changes from First Manufacturing Test

Various changes were made to the wheel geometry based on the results of the first manufacturing test: Because the pinch could not be laminated, the gap was increased to .56". This resulted in a gap of about .25" once all plies were laminated, which was sufficient to prevent accidental contact between plies and allow at least limited room for forming plies. To address the intricate geometry around the lug boss, the lug-boss was connected to the wheel center. Finally, because the part became trapped in the mold, a draft angle of five degrees was added to the vertical walls of the spokes to reduce friction when removing the part. Additionally, knockout features were added so that it would be unnecessary to pry on the barrel surface in order to remove the part. The result of these manufacturing changes is shown in Figure 69.

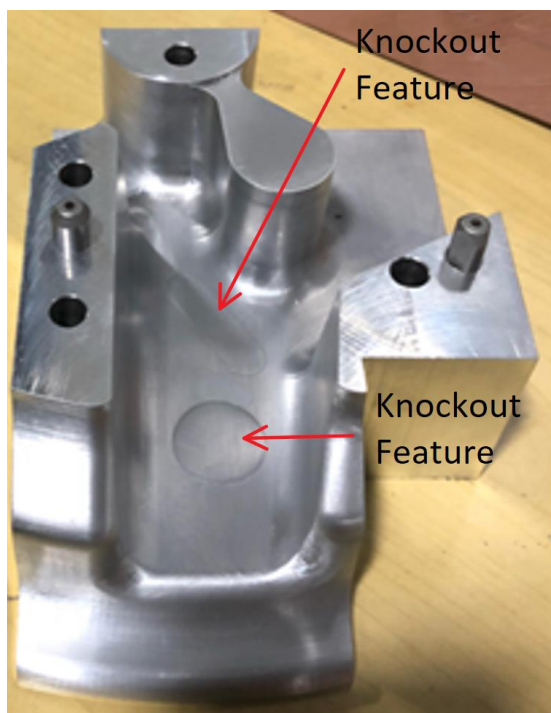


Figure 69. Revised test mold geometry. Knockout features labeled.

Cure Cycle and Fiber Wetting

To improve fiber wet-out and prevent delamination, the TC250 cure cycle was modified from the prior test: the 190°F hold (the segment of cure where most resin flow occurs) was increased from 30 minutes to 60 minutes. Based on the rheology profiles of TC250 it was predicted that increasing the duration of the low temperature hold would increase resin flow: During the 190°F hold the resin maintains very low viscosity, so increasing the duration of this segment of cure gives the resin more time to flow into the part. Figure 70 shows the recommended cure cycle for TC250, including the recommended hold and soak times.

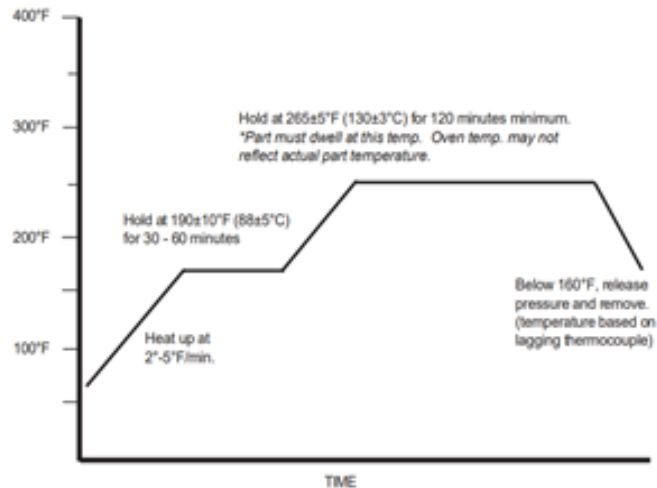


Figure 70. TC250 cure cycle. Source: TenCate advanced composites

To confirm that holding a 190°F dwell temperature for one hour would improve fiber wet-out, two panels of TC250 panels were produced. One panel was cured using the previous, 30-minute hold, cure cycle. The second panel was cured with the new, 60-minute hold, cure cycle. Figure 71 shows the panels produced using the two cure cycles.

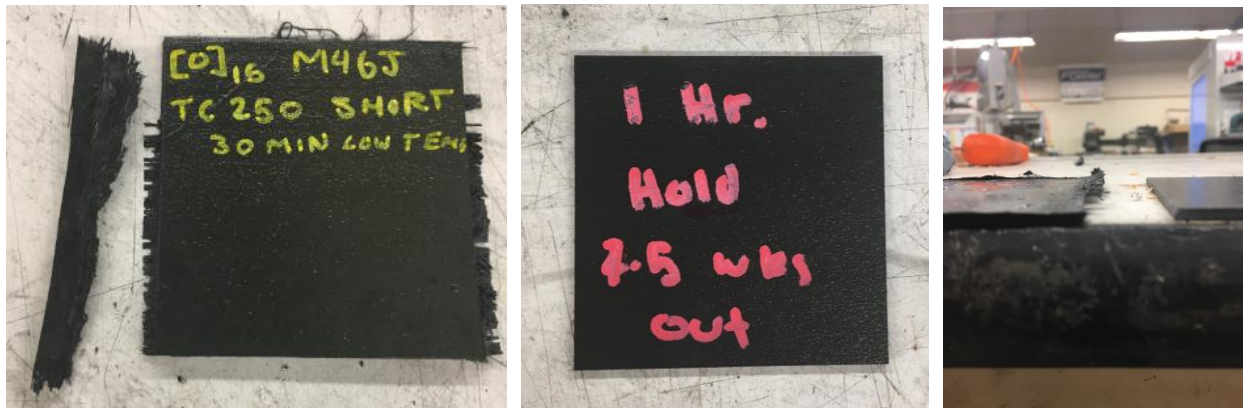


Figure 71. TC250 panels. 30-minute dwell (Left), 60-minute dwell (Center), and comparison (Right)

The panel cured with the 30-minute dwell had many loose fibers at the cut lines which are characteristic of poor fiber wetting. The panel cured with the 60-minute dwell had very sharp, well defined edges, which are characteristic of good resin flow and wetting. Therefore the 60-minute dwell was used for the subsequent manufacturing trial and wheel manufacturing.

Second Manufacturing Test

Inclusion of Film Adhesive

Following the resin rheology test, a second test specimen was laminated. Due to schedule constraints, the second manufacturing test was laminated in tandem with the rheology samples described in the prior section. In addition to the concern that the resin was not flowing into the fiber, it was theorized that the overall resin content of the laminate was too low: The laminate

comprised mostly of unidirectional fibers, which typically have low resin content. To correct for low overall resin content, layers of film adhesive were added after every four plies of the laminate. Figure 72 shows the laminate after applying a layer of film adhesive.



Figure 72. Film adhesive applied to laminate

Adding film adhesive to improve fiber wetting proved ineffective and unnecessary. First, modifying the cure cycle was sufficient to improve fiber wetting. This was most clear when the part was removed from the mold. The laminate did not, as previously, deteriorate when pried from the mold (with the exception of one knockout feature mentioned later in this section), and the section cuts produced defined edges with no loose fibers. Second, the section cuts clearly showed that the film adhesive did not flow into the fibers, but instead stayed between plies. Figure 73. shows one section cut where this effect is prominent.



Figure 73. Section cut of second manufacturing test. Purple streaks are film adhesive.

The layers of film adhesive caused areas of very high resin content, which reduce the shear properties of the laminate. Therefore, film adhesive was not used in production of the wheel.

Changes to Inserts

In addition to adding film adhesive, modifying the tool geometry and modifying the cure cycle, the lamination process and silicone tooling were changed to allow easier removal of the silicone inserts through the barrel and reduce the tooling required, respectively. To reduce the required tooling, the silicone geometry was simplified so that it did not reflect the geometry of the barrel.

The outer radii of the silicone were also removed. The simplified geometry was manufactured in a single piece mold. The differences in the silicone geometry are shown.



Figure 74. Changes in silicone geometry. First test (Left) and second test (Right).

As in the first manufacturing test, the silicone geometry was defined using the cured-ply thickness of the laminate. The same silicone (OOMOO 30) was used for both tests. The color variance is attributed to slightly different mix ratios for each insert produced.

To facilitate silicone removal, carbon was not laid over the silicone inserts to form a continuous barrel as in the previous test. Second, fewer cuts were made in the silicone inserts so they could be removed from each spoke as a single piece. The cut line between the silicone inserts was located at the line exactly halfway between two spokes, as this is the thinnest section of each spoke. If the cut line was not located at the thinnest section, the insert would have to be compressed through a thinner section, which would make removal more difficult. Figure 75 shows the inserts located in the mold during the final steps of the lamination process.



Figure 75. Silicone inserts. Cut-line circled.

Locating the cut-line at the thinnest section of the spoke caused other issues. Due to the extremely tight fit of the silicone inserts, it was impossible to ensure the silicone pieces were in perfect contact. While the expansion of the silicone during cure likely closed some of this gap, it was not entirely eliminated. As a result, carbon and excess resin were pushed into the gap between the pieces during cure, resulting in flash and reduced compaction. Figure 76 shows the flash between spokes which was visible after performing a section cut of the test piece.

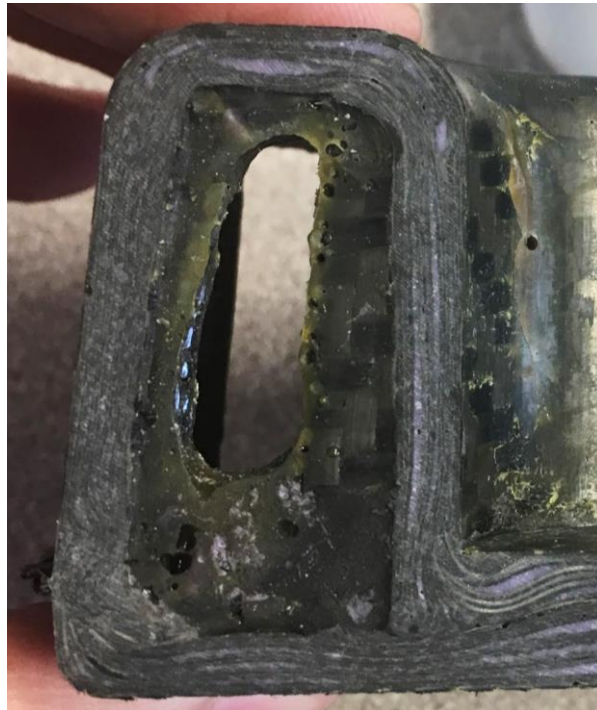


Figure 76. Flash region between spokes

Due to the weakened geometry at the cut line between the inserts, the inserts were oversized at the cut-line for the full wheel. By oversizing the pieces along the length, the silicone pieces were forced to contact each other and to compress slightly during the final steps of the lamination process. This is documented in the wheel-manufacturing section.

Flash at Split Line

In addition to the internal flash, there was flash at the split line between the molds. The flash at the split plane indicates that the fiber was forced to change direction sharply when pinched between the mold pieces. Such small radii in fibrous materials cause severe stress-concentrations. The small fiber radii and flash region are shown in Figure 77.

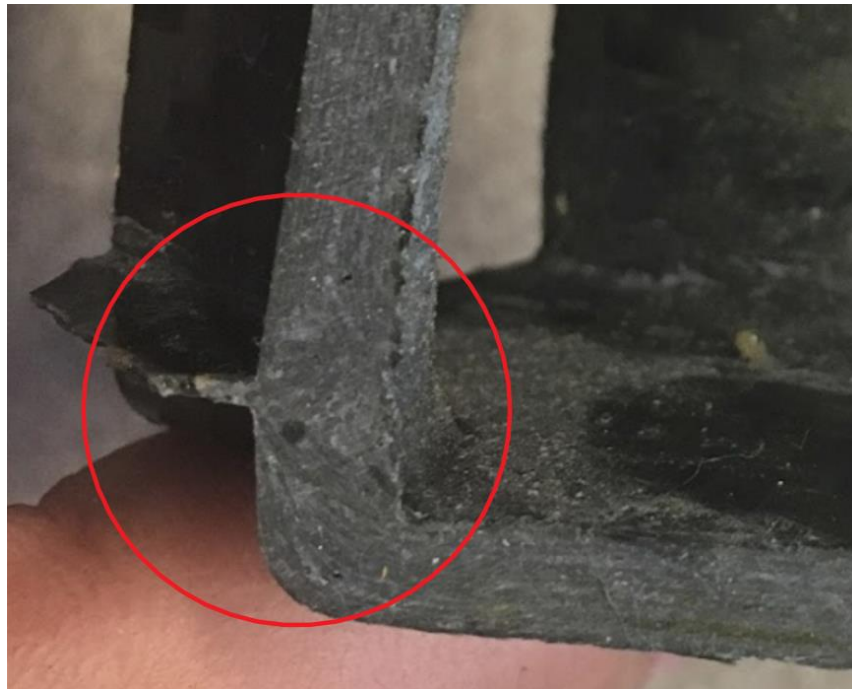


Figure 77. Close view of flash and fiber misdirection in second manufacturing test

Because small radii and fiber deformation cause severe stress concentrations in fibrous laminates, the split plane was assumed to be the weakest part of the spoke. Finite element modeling indicated that the highest-stress region of the spoke was the outboard surface near the lug-boss. The split plane was located almost all the way at the outboard-surface of the wheel for both manufacturing trials, and it was decided that placing the split plane so close to the highest stress region posed unnecessary risk. Therefore, the split plane was moved further outboard for the final wheel design. Figure 78 shows the change in split plane location.

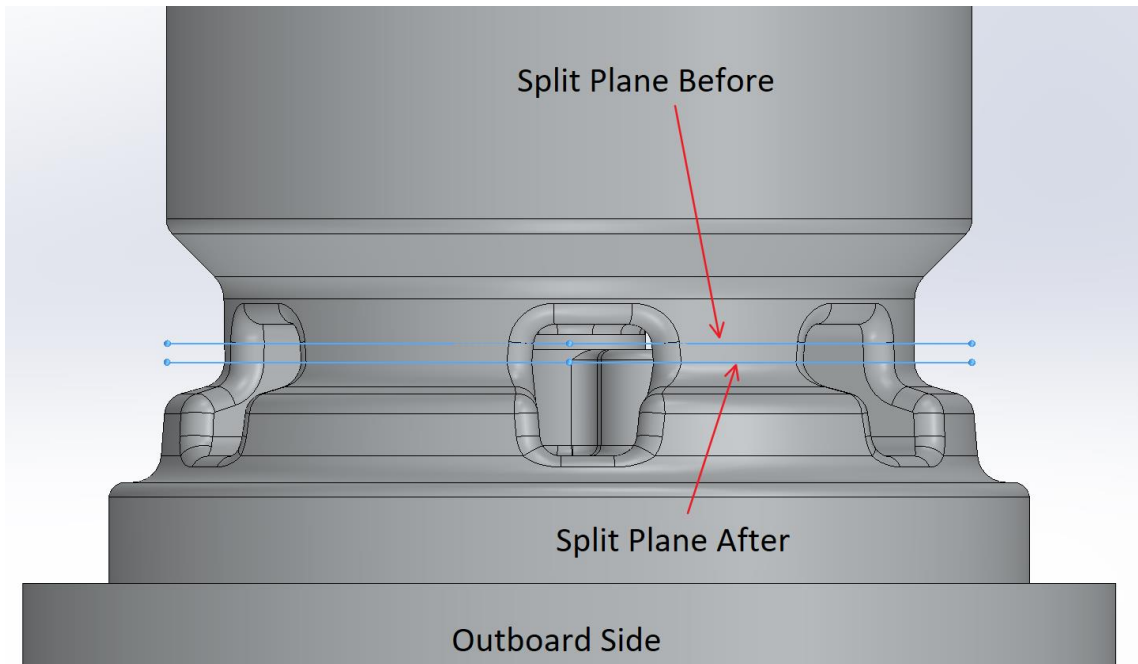


Figure 78. Split plane location change

Spoke to Barrel Transition

The transition between the spoke and barrel also had a defect: Compaction was very poor in the region where compaction switches from the silicone insert to the vacuum bag. The uneven compaction caused a sharp transition, which weakened the part. The transition between the spoke and barrel is shown in Figure 79, below.



Figure 79. Transition between spoke and barrel

The uneven compaction and sharp transition occurred because the vacuum bag could not compress the area directly adjacent to the insert. Because the insert protruded slightly from the

spoke (shown in Figure 80), the bag did not compress evenly across the surface and contour to the radius of the carbon.



Figure 80. Insert protruding from spoke

In order to improve and compaction, the insert geometry was contoured to match the barrel surface when manufacturing the wheel.

Knockout Feature Failure

With the added draft angle and knockout features, the part was removed from the mold. However, the laminate failed locally at one of the knockout features. The failure is shown in Figure 81.



Figure 81. Failure at knockout region

The failure occurred when the part became cockeyed during removal. High torque was applied to the bolt pushing out the knockout feature, and the laminate began to shear.

There were two conclusions based on the failure at the knockout region: First, the high forces required to remove the part would be reduced for the full wheel compared to the manufacturing test. Because the wheel has several spokes, each one could be pushed out evenly, which would prevent the part from becoming cockeyed during removal. Second, if the forces to remove the wheel were still too high, a removal jig could be built to pry the wheel from the mold.

Bag Surface Assessment

As mentioned previously, the mounting surfaces of the tire are determined by the vacuum bag and release films. These surfaces were inspected to determine whether the surface quality was smooth enough to mount the tire with minimal sanding, or whether a clamshell or post machining operation would be necessary (these surfaces were not inspected during the test as the issue with fiber wetting affected the surface quality). The bead seat produced during the second manufacturing test is shown.



Figure 82. Bead seat from second manufacturing test

The surface from the second manufacturing test was too rough to mount a tire without considerable sanding. Most of the wrinkles in the surface were caused by resin pooling under the FEP. Therefore, peel ply was used instead of FEP during the wheel production.

Conclusion of Second Manufacturing Test

Although there were various issues with the part produced during the manufacturing test, it proved the overall viability of producing the hollow spokes and transition to the barrel of the wheel. Figure 83 shows the part before it was sectioned in order to inspect for voids, tight radii, and fiber wetting.



Figure 83. Test part from second manufacturing test. Outboard side (Left), and inboard side (Right).

Summary of Geometry Changes

The geometry changes resulting from the manufacturing tests are shown in Figure 84.

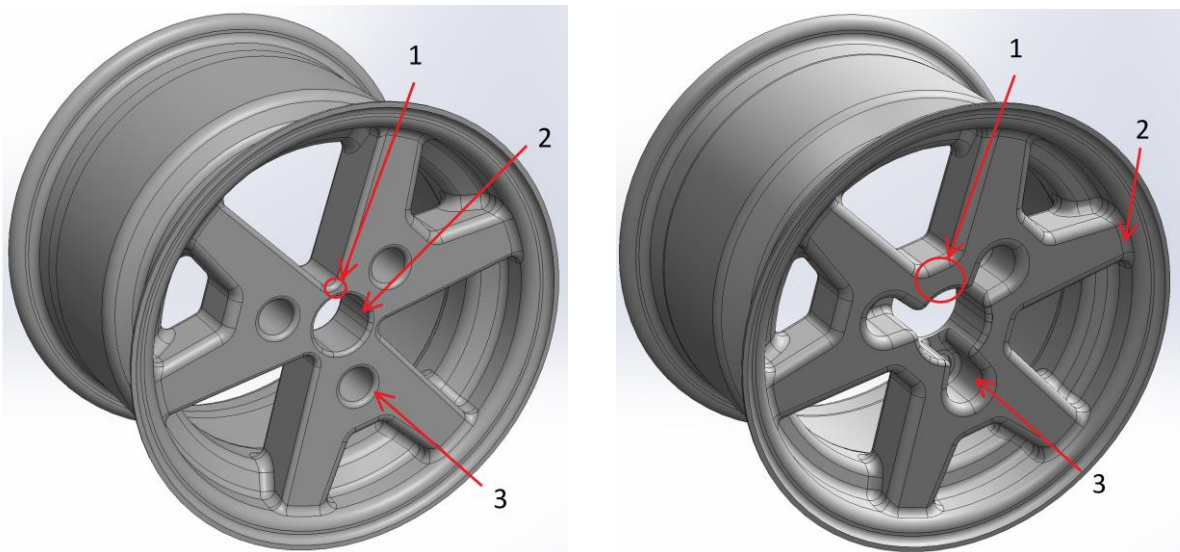


Figure 84. Wheel geometry before (Left) and after (Right) manufacturing tests

1. A minimum gap of .56" was incorporated between all vertical tool faces, increasing the gap between the wheel center and outside of the spoke.
2. The insert removal cutout in the wheel center was removed, and inserts were removed through the barrel instead.
3. The lug-boss cutout was integrated into the center bore.

Additionally, a five-degree draft angle was added to the spokes, and the split line was moved outboard. Finally, the inserts were contoured to match the local curvature of the barrel.

Wheel Manufacturing

Full Wheel Tool Detail Design

After completing the second manufacturing test, the mold design was completed. The completed 3D models for the tools are shown for reference.

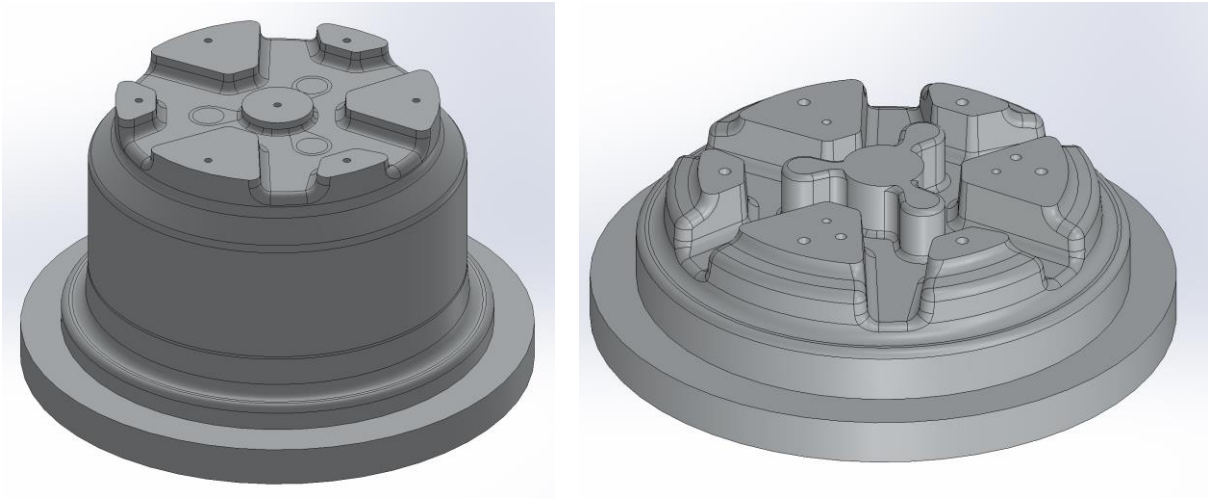


Figure 85. Completed tool design

Detailed drawings including hole sizing are located in Appendix A.

In addition to the overall tool architecture discussed earlier in the manufacturing section, several design considerations are worth noting. First, the tool geometry was scaled down from the desired size of the part in order to account for thermal expansion during cure. The equation for thermal expansion and the resulting expansion rate for aluminum are located in the Coefficient of Thermal Expansion section.

Another consideration related to thermal properties of the mold is that the mass was reduced in order to prevent the mold temperature from lagging the oven temperature. The tool was hollowed-out in order to reduce the mass. Typically, when a tool is hollowed-out it is better to keep the thickness of the tool consistent throughout various sections. This ensures that the tool heats evenly during cure. However, due to the high conductivity of aluminum, heat transfers very quickly from the thin sections (which heat up quicker) to the thick sections, so keeping the thickness completely uniform was not necessary. Therefore, to simplify the machining process a simpler cutout was designed onto the back of the tool, instead of matching the cutout to the spoke and barrel geometry. Figure 86 shows the completed tool design with a section view to make the cutouts visible.

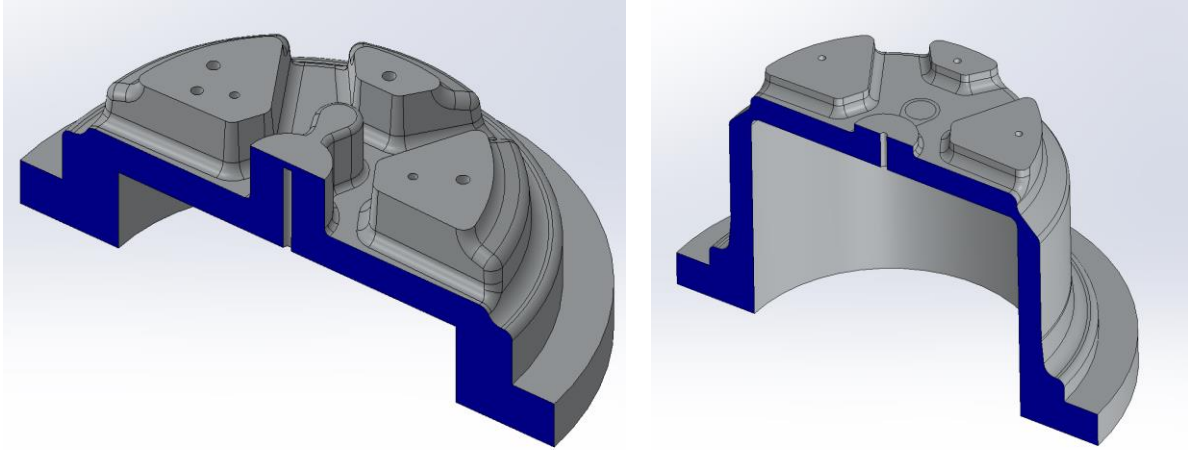


Figure 86. Section view of completed tool design. Outboard section (Left) and inboard section (Right)

Additionally, alignment pins were used to closely align the mold halves to each other. The locating pins used have diametral tolerances controlled to .001", so almost all float between two pieces mated with these locating pins is eliminated. In order to properly locate the mold pieces to each other, all six degrees of freedom must be constrained. A single mating pin prevents movement in four degrees of freedom (position in X, and Y, and rotation about X and Y axes in Figure 87) while the surfaces locate the position in one direction (Z). If a second round locating pin is used, the position in X and Y become over-constrained. Therefore, a diamond pin was used. The diamond pin is oriented so that it does not define the location of the hole, but only defines the clocking (rotation about the Z axis) of the pieces.

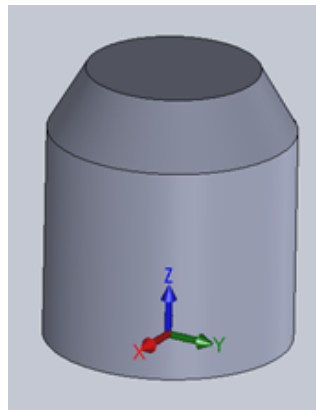
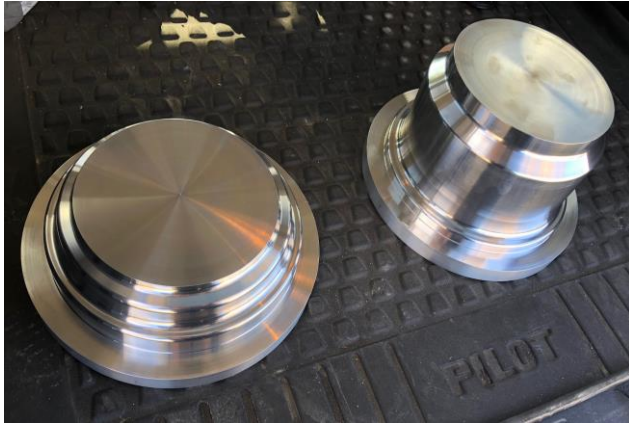


Figure 87. Degrees of freedom for locating pin

Tool Machining

The machining of the final molds was possible thanks to the generous donations of aluminum "ingot" material from Webber Metals and the CNC turning services of Custom Tube MFG. The large diameter of the molds made the turning and boring operations out of the scope of the machines available at Cal Poly, however, the milling operations could all be done in the Mustang 60 VF3SS.



88a. Mold blanks turned by custom tube MFG



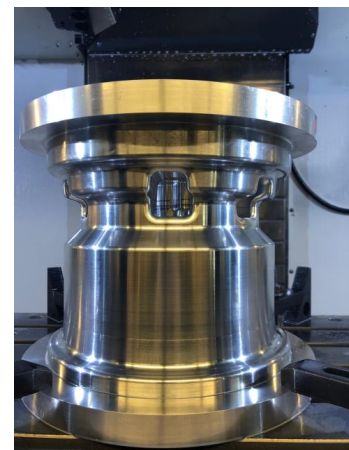
88b. Toe Clamp Fixturing in VF3SS

Figure 88. Mold machining

The large lip at the base of the molds made fixturing very simple with toe clamps positioned out of the way of the spokes. We elected to use standardized tooling rather than investing in tapered end mills which allowed us to vary the draft angle through the manufacturing trials and achieve smooth blending between the walls and floor fillets. All floor fillets were designed at radii of .25" and .125" to allow for a single cleanup pass rather than surfacing close to the floor of the spoked sections. The flat section of the spokes was designed to have a minimum clearance of 3/8" to allow for a cutter to access all the flat areas without 3d surfacing. CAD and CAM for the molds were done using SolidWorks and HSM Works respectively and can be found on the Reinventing the Wheel Google Drive as well as in the manufacturing GrabCAD. The molds were roughed with 1/2" and 3/4" corncob roughers using a 3D adaptive toolpath with a step height of .05" before being cleaned up with the 1/2" ball end mill. To minimize cusps a .02" stepover was used with a 3D contour toolpath for the tapered walls of the spokes. Some steep areas needed additional passes using the scallop toolpath. Spiral taps were used for all threaded holes to ensure proper alignment and high-quality threads.



89a. Tooling used in mold milling



89b. Assembly test fit

Figure 89. Mold machining

After the machining was complete the molds were finished up with wet sanding up to 800 grit and finished with aluminum mold polish.



Figure 90. Mold surfaces before (top) and after (bottom) polishing

Our final silicone molds were machined out of renshape tooling board in the Cal Poly Hangar on the TM1 mill, as shown in Figure 91a. After the first layup attempt we determined that the threaded holes and inserts were insufficient for separating the mold halves. To allow for fixturing in the hydraulic press a bore was machined in the short section of the mold to receive a 1" rod

and material was removed from the tall section to allow clearance for vertical supports. Photos of the modified mold can be found in Figure 91b.



89a. Silicone mold



91b. Mold modified for hydraulic press

Figure 91. Silicone mold manufacturing and wheel mold modifications for part removal

Lamination: Barrel

The first ply of the barrel was split between the bead seat and the cylindrical section. The cylindrical section was laminated using a single piece of cloth which was trimmed to form a single butt-splice along the vertical seam of the ply. The transition between the single ply used to form the cylindrical section of the barrel and the bead seat is shown.



Figure 92. Transition between bead seat and cylindrical section

Subsequent plies on the barrel were laminated in vertical strips about four inches wide. Vertical slits were cut in each laminated section in order to contour the fiber around the complex contour at the bead seat. The splices were overlapped in the fiber direction only. For the first half of the lamination process, the barrels were laminated separately. This eliminates load transfer between the barrel halves for the first half of the laminate, reducing strength and stiffness for loads normal to the hub. However, most of the plies on the barrel are in the hoop direction and would not transfer load in this direction, so the reduction in strength is not substantial. After the

mold halves were bolted together, the final plies were laid continuously across the barrel, and holes were cut around the silicone inserts to allow their removal after cure.

Lamination: Spokes

Each spoke was laminated in multiple small splices. Splices typically divided each spoke between the horizontal and near-vertical surfaces, although overlaps between sections varied between sections: In some instances, the horizontal splices extended to the near-vertical walls of the mold, and in others the near-vertical splices were extended onto the horizontal sections. This variation was used to prevent excessive buildup on either the near-vertical surfaces or the horizontal surfaces. For the first ply, the same technique was used as the barrel: Splices were trimmed to have no overlap. Figure 93 shows several steps of the spoke lamination process.



Figure 93. Spoke lamination steps: first ply (Left), unidirectional plies (Right)

For the first half of the laminate, each spoke was laminated in sequence with the corresponding ply on the barrel. However, because the spokes are thicker than the barrel, this sequence could only be followed for the first few plies. After this point, the remaining plies of the spoke were laminated consecutively. After every four plies, floral ethyl-polypropylene (FEP) was placed over the carbon, and the part was debulked. Figure 94 shows the wheel center covered with FEP before bagging.

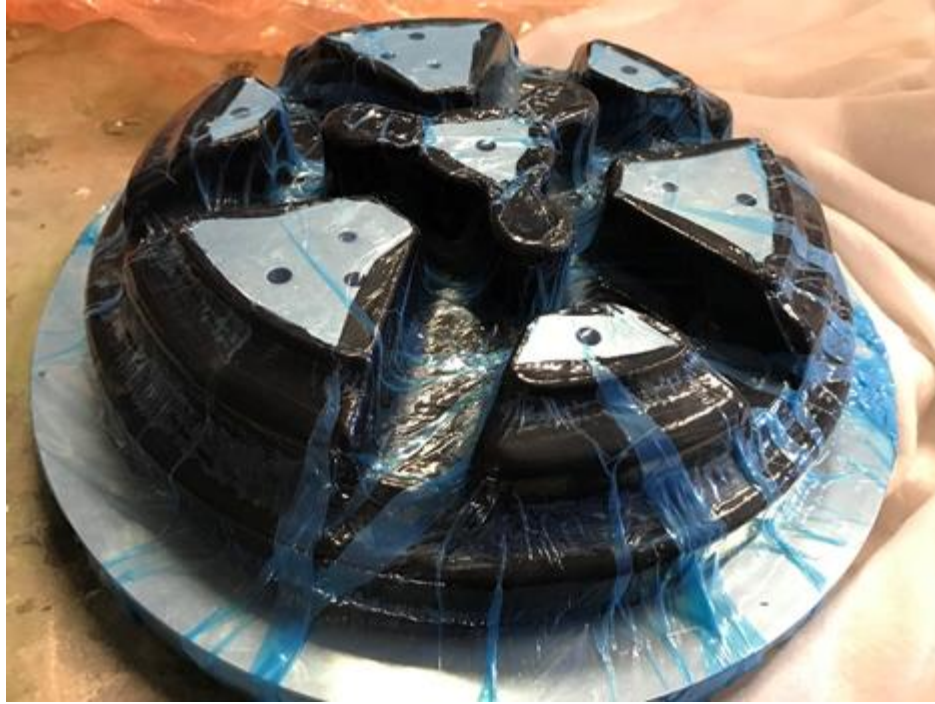


Figure 94. Wheel covered with FEP before debulk

Lamination: Flying Splice

A “flying splice” joint was used to mate the two halves of the spoke. The flying splice refers to fiber which was extended past the mold surface on one half of the barrel before the halves of the mold were bolted together. For each successive ply, the fiber was laminated to extend about .125” past the previous ply. In practice, achieving exactly .125” of extra laminate is very challenging, as plies are trimmed by hand using a razor-blade. After the final ply of the spokes was laminated, the silicone inserts were placed inside each spoke, and the flying splices were contoured over the inserts. The flying splice on the lug-boss is shown.



Figure 95. Flying splice at lug boss

Mating Process

The mold halves were bolted together using ¼-20 steel bolts. The main challenge when mating the halves was ensuring that the carbon fabric was not pinched at the mating surfaces. Pinching the fabric at the mating surfaces causes flash and very abrupt changes in fiber direction, which causes stress concentrations. The flash caused by pinching the fibers is visible in Figure 77 in the manufacturing trial section.

In order to prevent pinching the fiber between the mold halves, the fibers were pushed out of the gap between the mold halves as the mold was assembled. Popsicle sticks were used to reach in the thin gap between the mold pieces and push the fiber out of the gap. Figure 96 shows the gap between the mold halves. For future efforts, it is recommended to use a series of shims which match the profile of the mold at the mating surface in order to prevent pinching. As the mold is bolted together, one shim could be removed at a time until the halves are perfectly flush.



Figure 96. Gap between mold halves: Popsicle Stick (left), bolt (center left), and insert (right) shown

Bagging and Cure

After lamination, the part was covered with peel ply, then bagged using high-temperature vacuum bag. Following the bagging procedure, the part was cured according to the same cure cycle used for the second manufacturing trial.

Labor Time

The required labor to produce each wheel is a significant consideration for future attempts to produce a composite wheel. Therefore, lamination time for each section of the wheel was recorded during the manufacturing process. The total labor time to laminate the wheel was 100 person-hours. 4 of these are attributed to debulks and final bagging, and 70 are attributed to laminating the wheel center. Laminating the barrel took 22 person-hours, and bolting the tools together took 4 person-hours. For the lamination time, about 20% of the time was spent cutting plies, which is a significant reduction compared to the manufacturing trials: Dedicating one or two team members to cutting carbon instead of switching between tasks made it easier to keep

track of which plies were already cut. It also made the cutting process faster as they didn't not have to put down and then relocate blades. In addition to the labor time, the part was debulked for about 40 hours. Typically, the parts were debulked overnight after every four plies laminated in the wheel center.

Further improvements to the manufacturing speed are still possible, however. The manufacturing time for each ply decreased substantially after the first few steps of the process, as mistakes such as cutting plies in the wrong orientation were reduced. For the wheel center, the average time dropped from six person-hours per ply to two person-hours per ply. The average ply for a ply on the barrel dropped from three person-hours per ply to 1.5 person-hours per ply. Therefore, the predicted manufacturing time for future attempts is about 50 person-hours. To further reduce manufacturing time, an automated ply kitting machine may be used to eliminate the need for any cutting or trimming. Using a kitting machine would also produce more accurate cuts than are possible by hand, which could further reduce lamination time by producing pieces which are easier to contour.

Six people can laminate the wheel before the mold halves are bolted together (three can work on each mold half at a time). After this, only two can effectively laminate at a time, as all remaining work must be done on the barrel only. Therefore, if a team of four to eight people (growing when there is room for all eight to work at once and shrinking at the end when only four may work at a time) divide the cutting and laminating jobs as described it would be feasible to laminate a wheel in a single weekend. Laminating a wheel in a single day is possible from a labor standpoint, but it is recommended to debulk the part for at least 10 hours (four debulks of 2.5 hours each), so laminating the wheel in a single day is not recommended.

Result

After cure, the bagging material was removed, along with some of the peel ply. Several attempts were made to de-tool the part. The normal mechanism for separating the mold halves was a set of threaded holes designed for bolts to press the halves apart. However, during cure, resin flowed into the threaded holes, making it impossible to thread in the bolts. When threading the bolts in was attempted, several of the bolts snapped off as they were blocked by the resin.

Next, a press-feature was machined into the mold which allowed a hydraulic press to separate the mold halves. This was successful in separating the mold halves, however the laminate failed during the process. After the initial separation, it was clear the laminate was very dry, similar to the first manufacturing test. Figure 97 shows wheel center after attempted separation.



Figure 97. Failed wheel center

Given the severe failure and the similarities to the first manufacturing test, an improper cure cycle was the most likely cause of the fiber failure. The following sections investigate the cause of the improper cure.

Thermal Lag Issues

As discussed in the tool detail design section, thermal mass is a major consideration in the design of any prepreg lamination tool. While design measures were taken to reduce the thermal mass of the tool, the large ratio of mass to surface area caused the mold and part temperature to lag behind the set temperature of the oven (the ability of a part to absorb thermal energy is positively correlated to its surface area, while the total energy required to heat the tool to the desired temperature is a function of its volume and density). When this happens, the temperature difference drives the tool and part to follow a difference cure cycle than the set cure cycle, which often has negative results including insufficient wet out or excessive resin pooling. It was theorized that thermal lag may have caused improper curing conditions and insufficient fiber wetting, so the thermal lag of the tool was assessed.

Thermal Lag Test

In order to characterize the thermal lag of the tool surface relative to the oven-temperature, the tool was bagged again with the destroyed wheel still on the tool surface, and a thermocouple was placed on the tool surface under the edge of the part. The placement is shown in Figure 98.

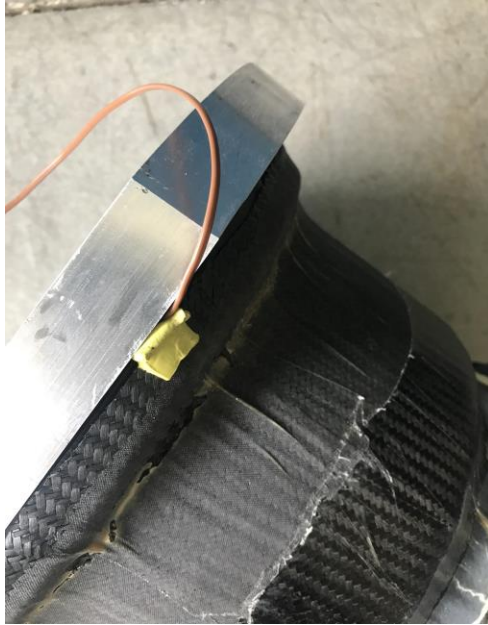


Figure 98. Thermocouple placement

After bagging the part, a second thermocouple was placed inside the oven about one foot from the tool in order to measure the ambient air temperature. The initial cure was run again, and the temperature of the tool and the ambient air were logged throughout the cure cycle. Figure 99 shows the resulting temperature profiles of the tool surface and air. The thermocouple signal was lost between 130 and 150 minutes, so there is no data for this segment of the test.

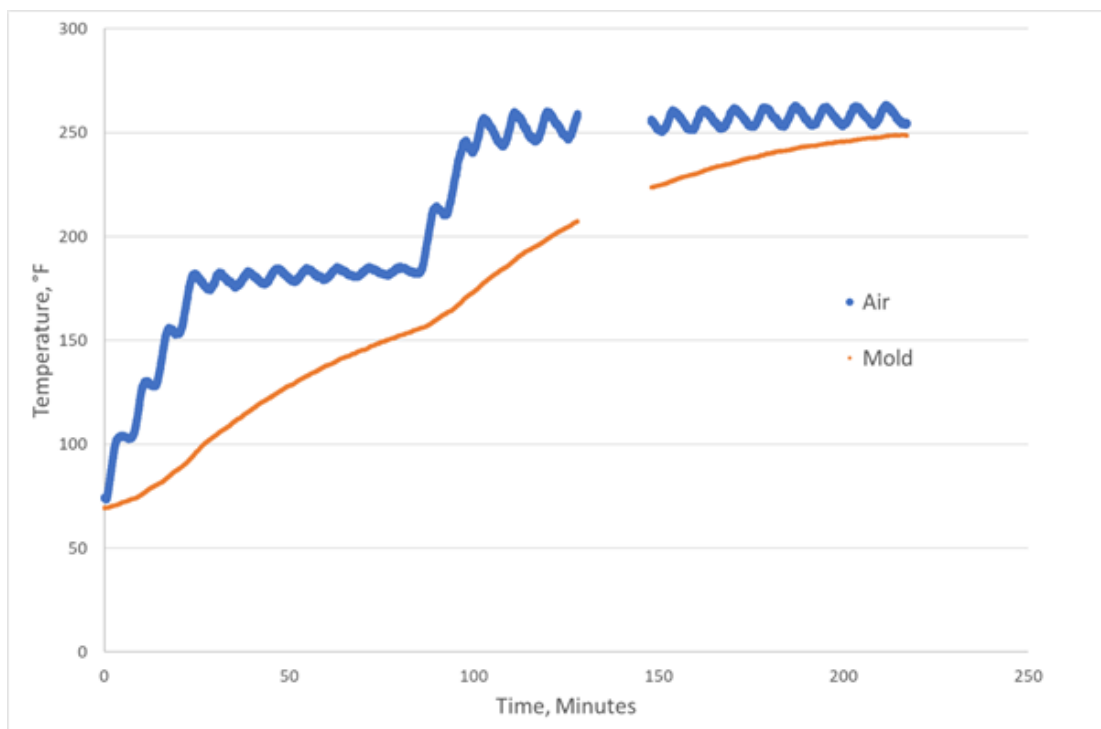


Figure 99. Tool surface temperature and air temperature

Two considerations when assessing thermal lag are particularly important: First, if the part temperature never reaches the highest set temperature, then the resin will not completely cure. In this case, the part reached the highest set temperature after about 3.75 hours. The cure cycle used also held the final cure temperature for two hours after this time, so the resin most likely did cure completely. Second, if the part temperature does not follow the ramp rates and soaks closely, then the resin may not flow into the fiber as intended, or it may not have the desired structural properties after cure. The tool profile did not follow the set ramp-rates or temperature soaks, which adversely affected the fiber wetting. Most notably, the tool didn't approach the desired soak temperature until the end of the set time for the soak. When it did, the oven temperature was already ramping up to the final cure temperature. This caused the tool temperature to pass through the soak temperature very quickly. From the previous manufacturing trial, it was apparent that reducing the time the resin spends at the low-temperature soak has a very negative effect on fiber wetting. Therefore, the temperature lag caused insufficient fiber wetting and subsequent failure when trying to remove the part from the mold.

Recommendations to Compensate for Thermal Lag

In order to prevent temperature lag on subsequent manufacturing attempts, it is recommended that the cure cycle be adjusted in order to compensate for the temperature lag. The oven should be set to skip the low-temperature hold and instead skip to the high-temperature hold. Shortly before the part reaches the low-temperature hold, the oven temperature should be lowered to match the low-temperature hold. Then, once the part is at the low-temperature hold for one hour, the oven temperature should be set above the high-temperature soak until the part approaches the high-temperature soak temperature. At this point the oven temperature should be lowered to the high-temperature soak temperature for the duration of the cure. This pattern of overshooting the desired cure temperature will result in faster ramp rates to the desired set temperature, thus compensating for the lag caused by the tool's mass. A suggested cure cycle for this process is shown in Figure 100 (along with the previous cure cycle for comparison). The resulting tool temperature should be measured for this cure cycle before laminating another part.

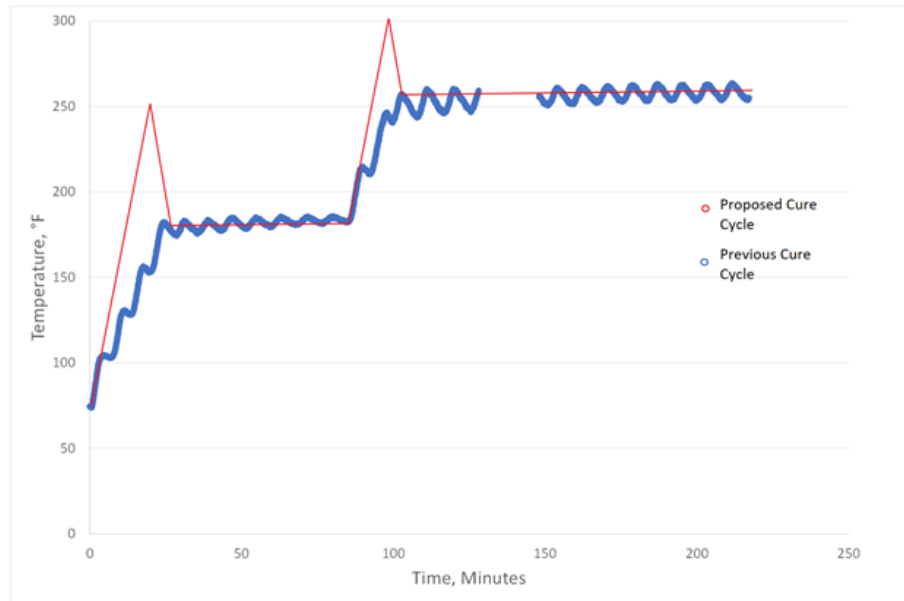


Figure 100. Recommended cure cycle to compensate for thermal lag

Silicone Change

The final issue noted was the properties of the different silicone selected for the full-scale wheel production. The silicone used was Mold Star 20 T which was much harder than the OOMOO 30; selected for the manufacturing trials (both products are produced by Smooth-On, Inc). Mold Star 20 T was selected due to its much faster cure time compared to the previously used OOMOO 30. However, the harder silicone was much more difficult to remove through the hole in the barrel due to higher friction with against the inside surfaces of the spoke. The harder silicone was also much more difficult to compress into the spokes, which made mating the mold pieces substantially more difficult.

While the difficulty compacting and removing silicone was overshadowed by the overall failure of the cure due to thermal lag, it is recommended that the softer OOMOO 30 will be used for any subsequent manufacturing attempts involving hollow geometry.

Bagging Surface Quality

One key consideration in the tooling design was whether the external clamshell tools are necessary to produce the tire mounting surface. Due to schedule constraints these tools were not produced. However, the bead seat was inspected in order to assess whether the clamshell tools should be produced for future wheel manufacturing attempts. There are, however, some limitations to inspecting the wheel which was produced: Because the resin flow was severely impaired during cure, and resin flow drastically affects the bagged surface quality, the results from this inspection are not as meaningful. However, the resin pooling at the base of the bead seat increased the radius at the bead seat, which likely makes the surface unsuitable for tire mounting, even with significant sanding. As shown in Figure 101, the surface is mostly free of wrinkles, but has substantial resin pooling.



Figure 101. Bead seat of wheel. Areas of severe resin pooling circled.

Therefore, it is recommended to use a silicone caul sheet in order to provide even compaction and reduce resin pooling. The caul sheet should be produced from a machined tool which defines the desired bead seat geometry. In the event that the caul proves ineffective at controlling the bead surface, the machined tool can be used to produce a composite clamshell.

PLANNED FUNCTIONAL AND STRUCTURAL TESTING

The following sections outline testing that was planned, but never achieved due to unsuccessful manufacturing attempts.

Pressure Decay

After the tire is mounted to the wheel, the seal between the wheel and tire is assessed: The tire is inflated to 10 psi, then the pressure and temperature is recorded every twelve hours for one week. If major leaks are detected, the bead seat geometry and manufacturing are reassessed.

Full Wheel Stiffness Test

In order to validate that the wheel meets the stiffness requirement set for the project, the wheel is placed on a test fixture which supports the outer section of the wheel. The wheel center is compressed, with force and center displacement recorded. While the results of this test do not indicate the camber stiffness of the wheel directly, it is used to verify the FEA model which does predict wheel stiffness. The full-wheel test is shown below:



Figure 102. Full wheel test

A similar wheel-only test can be performed to more accurately assess camber stiffness. The wheel is bolted to a structure with similar geometry to the hub (wheel studs and center boss) but significantly increased stiffness to minimally contribute to measured deflection (although the stiff hub structure's deflection can be measured with a dial indicator if it is a concern). With the hub structure fixed to a table, weight representing a cornering force can be hung from the wheel's edge and deflection along the spoke can be measured.

Full Wheel Cornering Strength Test

To develop full confidence in wheel strength, representative strength testing must be performed in the max cornering loading case, to 1.5x the max expected load. Such a test would be successful if no deformation, cracking, or other types of composite damage are observed. See a rough concept sketch in Figure 103.

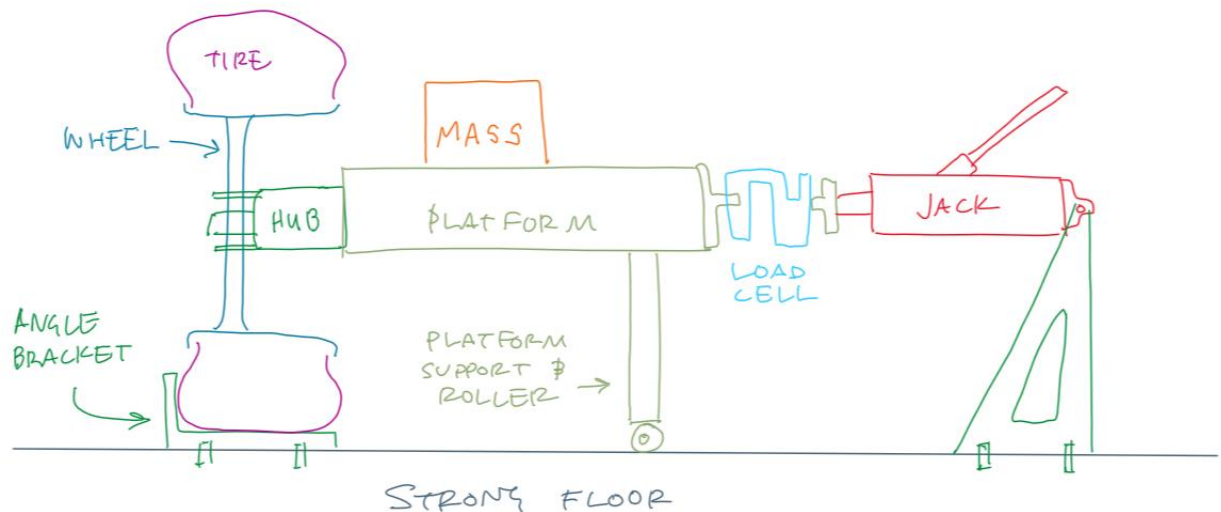


Figure 103. Sketch of full-wheel cornering strength test

The mass is sized to represent the normal load on the most heavily loaded tire in maximum cornering. The tire mounted to the wheel is positioned against an angle bracket (whose height is shorter than the sidewall) capable of supporting the test lateral load, since the tire's lateral coefficient of friction while driving exceeds what can be produced with static friction alone. The same mock hub described in the wheel-only stiffness tests can be attached to the end of a platform, in line with a load cell and hydraulic ram. The hydraulic ram can be extended gradually, applying force which can be measured by the load cell. The roller must be sized such that the platform is kept horizontal at the compressed state of the tire. The test is designed to use materials available for check out from the ME Department and be run on the composites lab strong floor.

Vehicle Test

Finally, to ensure safe use, a single wheel is run on the vehicle with the remaining three corners running the trusted aluminum wheels. The vehicle should be driven normally, with frequent inspection of the carbon wheel for cracks, deformation, and failures.

TIRE MOUNTING

The two main concerns with tire mounting are the load from holding the wheel in place and the load from manipulating the tire around the wheel, including breaking the bead. Changing a tire on a manual rig relies on contact force between a tire iron and the wheel rim. Modeling a standard 16" tire iron as a lever and the tire as a simple support, as shown in Figure 104, the contact force on the rim should be about 15 times the applied force. The unknown applied force can be bounded at a maximum of the weight of the person using the tire iron, but from experience, this force is likely much less than body weight. Half a person's body weight (say, at an average of 170 lb) average will be used as a conservative estimate. This yields a contact force of 1275 lb, or 10200 psi across a 1"x.125" contact area.

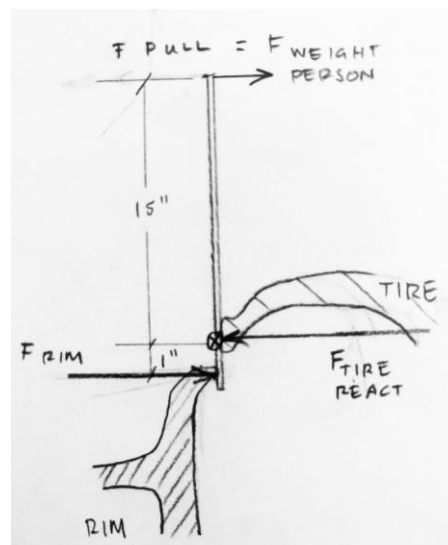


Figure 104. Tire mounting loading by a tire iron

A standard tire changing machine, like the one in Figure 105, on the other hand, has a guard on the arm that rides along the upper rim to protect the wheel from contact forces from the tire iron. As a result, the forces at the rim from tire manipulation are largely a function of the tire's own stiffness and resistance to mounting. These forces are more evenly distributed about the rim and more likely to be on the order of forces seen by the car during driving. The concern with a tire machine is, however, the way it holds the rim. A tire machine generally uses pneumatic pressure to clamp the edge of the rim at 3 or 4 points. The magnitude of these loads are currently unknown but can be assumed to be proportional to the supply air. It is possible that we could run a pressure regulator on the air line before a tire machine and reduce this load to a magnitude safe for delicate rims. Additionally, as contact force is likely the concern, soft jaws would be made to adapt the clamping feet on the machine currently used by the team to protect the integrity of the rim.



Figure 105. Tire mounting machine

CONTINGENCY PLAN

In order to protect for the risk associated with the project failing either through manufacturing issues or failure to meet our strength or stiffness goals, we designed a backup wheel. As the project did fail to deliver wheels, we made three sets of aluminum wheels, comprised of Keiser 10" shells and in-house, custom machined wheel centers. The shells cost \$110 each and the centers were machined from 6061-T651 aluminum than had already been donated to the team. The aluminum wheels used the same offset, width, and lug-bolt pattern as the designed carbon ones.

CONCLUSION

Overall, manufacturing difficulties prevented the production of a representative wheel. The following analysis and discussion gives insight into next steps a future team can take.

Full Carbon Wheel

Assuming similar manufacturing processes, a carbon center is not recommended if the team is using a lugged architecture. Lug related difficulties were anticipated at the beginning of the design stage, however a hub redesign was out of scope for the team and this project. The lug interface results in a complex and less structurally efficient center geometry. The complexity makes the center difficult to laminate, with center lamination time taking 70% of total manufacturing time for the final design of this project. The open spoke sections were straightforward to laminate; however, the lug-boss sections proved to be tricky. Senior project teams in the past have cited that center locks feature a lower specific stiffness than lugged designs for aluminum wheels. However, if center locks allow for a carbon center design with reasonable manufacturability, it is likely worth the gained specific stiffness from a carbon center. Therefore, it is advisable to only take a carbon center into serious consideration if the team pursues a center lock architecture, where a simpler and more structurally efficient center geometry can be achieved.

Lugged Architecture

If the team decides to continue with a lugged architecture, there is still benefit in a carbon wheel shell. To highlight a minimum achievable specific stiffness gain, full aluminum wheels with Keizer shells and a custom center from the 2017 season were analyzed. This analysis uses the same loads and boundary conditions discussed in previous sections. Then, the same rim laminate used in the final one-piece wheel design was substituted for the aluminum rim, with everything else kept the same. Mass and stiffness results can be seen in Table 21.

Table 21. Mass and stiffness results from comparison study

Wheel	Camber Compliance (deg/g)	Rim Weight (lb)	Center & Fastener Weight (lb)	Specific Stiffness (g/deg*lb)	Percent of Highest (%)
<i>Reinventing the Wheel</i> One Piece	0.094	1.66	1.16	3.78	100
Carbon Rim, Aluminum Center	0.38	1.9	1.2	0.83	22
Full Aluminum	0.28	4.1	1.2	0.67	18

As seen in the table above, carbon rims alone feature a 24% increase in overall specific stiffness from a full aluminum wheel. However as previously mentioned, this is a minimum projected gain. The composite material properties vary greatly from the data sheets likely due to

resin degradation or imperfect manufacturing conditions. Improving manufacturing conditions or switching to a resin infusion type process where unexpired resin is used could boost properties. This may prove difficult to achieve considering the typical materials and facilities available to the team; however, it is worth investigating.

Changing geometry could also increase composite shell gains. In the context of a student team, available resources do not support the production of a custom aluminum shell geometry (spinning, casting, and machining are all outside of our capability). Therefore, a composite wheel is the only way a team can realize more structurally efficient shell geometries. Since a conical rim for a 10" wheel is difficult for internal packaging, it is ideal to minimize the depth of the rim divot used for tire mounting in a straight barrel design. Under lateral loading, the divot sees bending in its radially directed walls, essentially bending like a plate, as shown in Figure 106. The wheel spokes (especially if hollow, as designed in the carbon center) are more structurally efficient in bending. Hence, the stiffest wheel would be one with the smallest divot as a fraction of the total wheel center radius. With a minimized divot depth, the rim will see primarily hoop and axial deformations, allowing a designer to better optimize a laminate for these directions. Some amount of divot is necessary for tire mounting. However, the Hoosier 18x10-7.5 tires chosen have reasonably compliant sidewalls and proved very easy to mount, so it is assumed that shrinking the divot would not inhibit tire mounting.

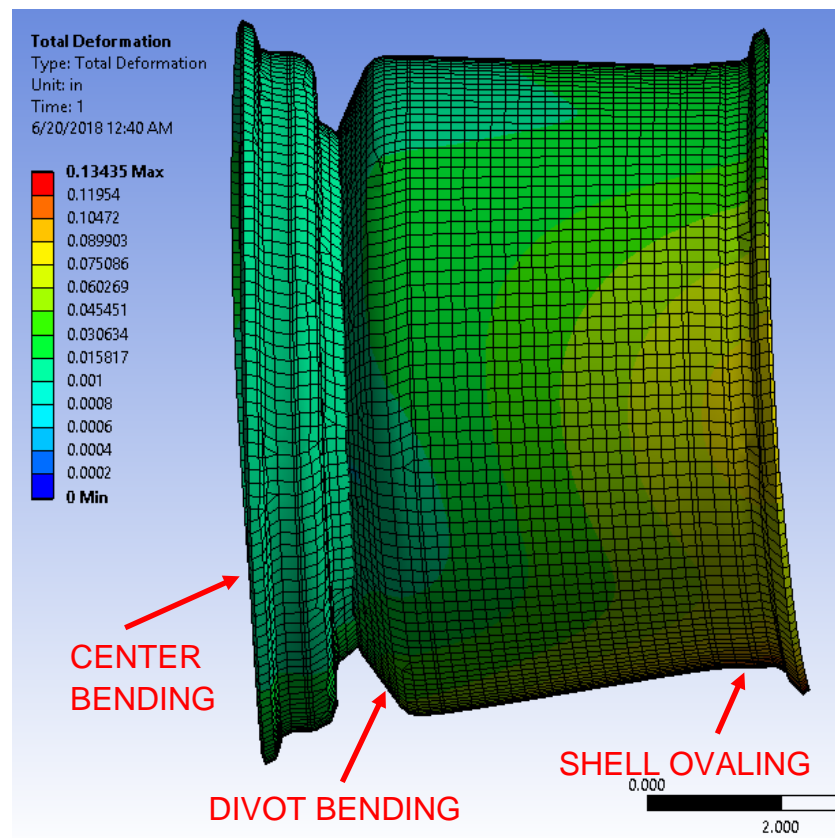


Figure 106. Deformed shape of the Keizer aluminum wheel shell under lateral loading. Three contributions to camber compliance shown: bending in the center, bending at the center-shell attachment which doubles as the tire mounting divot, and deformation of the shell

Independent of geometry, the rim would also benefit from further laminate optimization. In this project, the same laminate was used for the entire rim. However, it is likely that the divot area could use more 0-direction fiber for lateral load bending, while the straight section needs more 90's to limit hoop deformation.

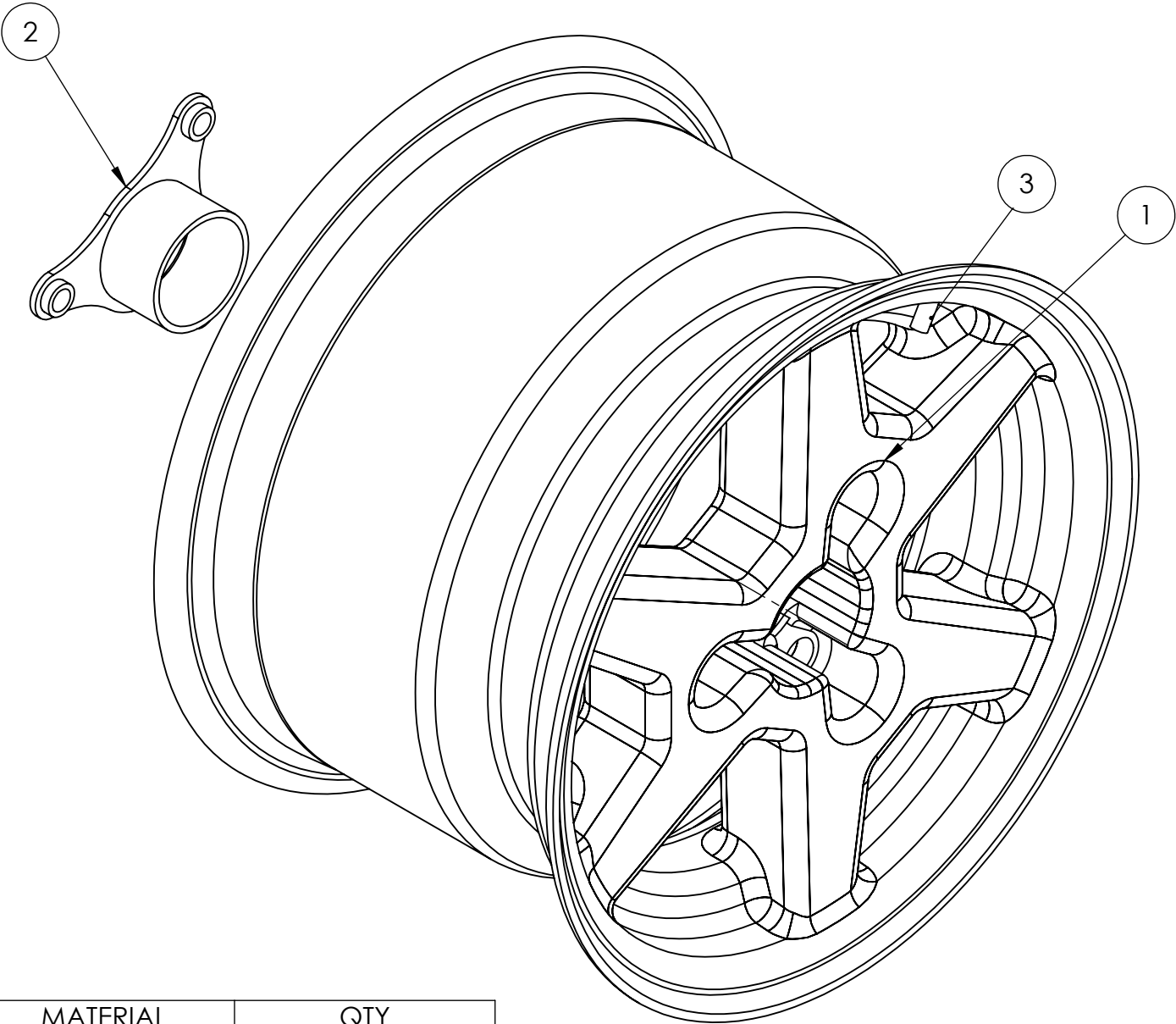
Manufacturing

If a carbon rim is pursued, an outer mold line tool is recommended to control important surfaces such as the bead seat. This would prevent the need for caul sheets, clam shells, or prediction of cured ply thickness.

For hollow geometries, it is recommended to experiment with wrapping the carbon around the inserts, then placing them in the molds. This would have been difficult to do with the complexity of the final design geometry but could be done to eliminate the need for a flying splice in a simpler design. Eliminating the flying splice would be beneficial since there would likely be less flash and better load transfer between part halves.

If a flying splice must be done, find the smallest possible insert size that provides the necessary compaction. Inserts in this project provided good compaction but made placement and mold half mating difficult.

APPENDIX A: DIMENSIONED DRAWINGS



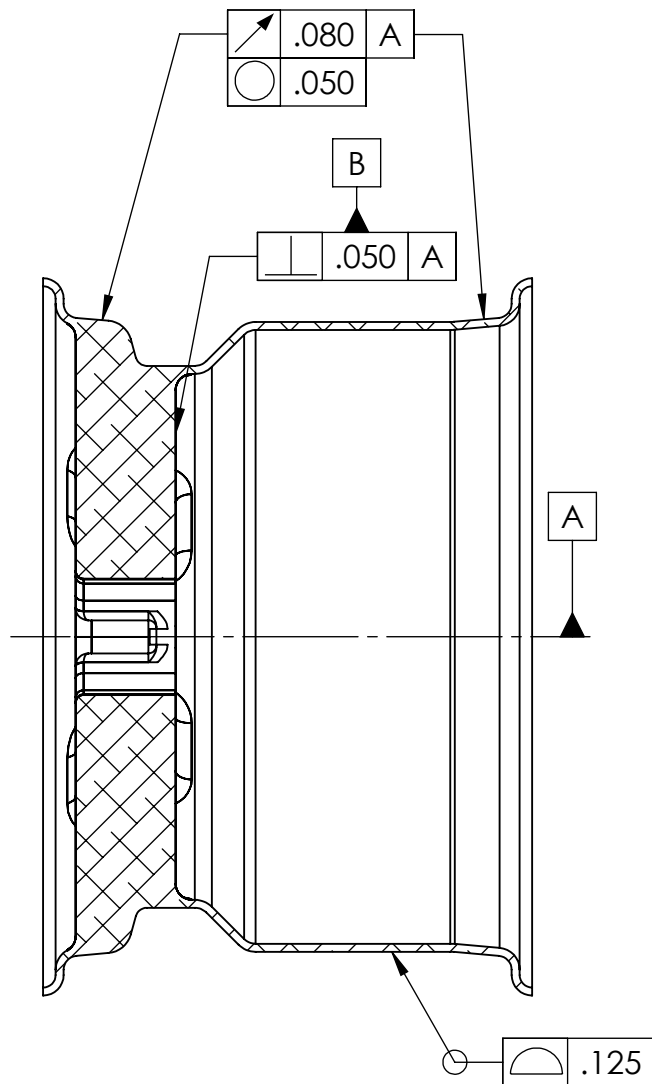
ITEM NO.	ITEM	MATERIAL	QTY
1	WHEEL	CARBON FIBER	1
2	CENTER INSERT	6061 ALUMINUM	1
3	VALVE STEM	VARIOUS	1



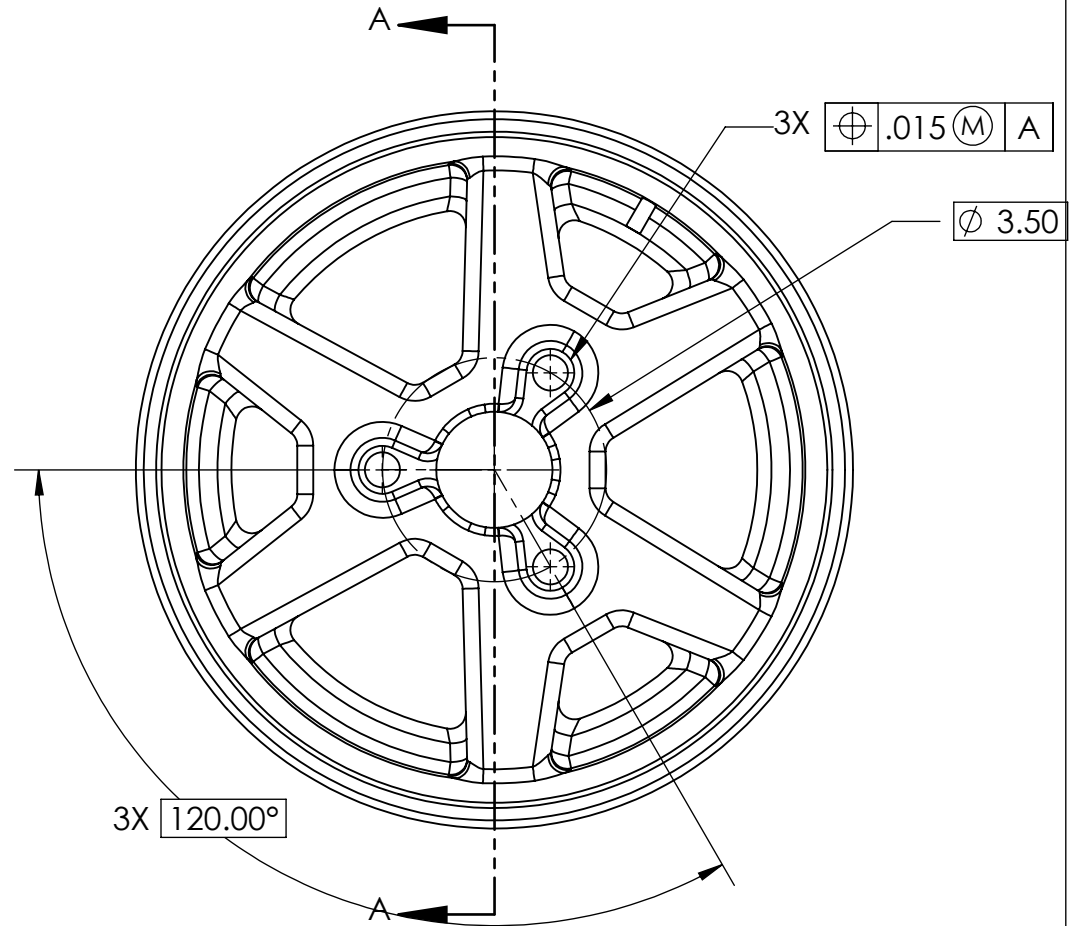
Drawn By: ADAM MENASHE

UNLESS OTHERWISE SPECIFIED:
DIMENSIONS ARE IN INCHES
TOLERANCES:
FRACTIONAL: $\pm 1/8$
ANGULAR: MACH $\pm 1^\circ$ BEND $\pm 2^\circ$
TWO PLACE DECIMAL: ± 0.05
THREE PLACE DECIMAL: ± 0.005
TOLERANCING PER: MMC

TITLE:		REV
WHEEL EXPLOADED VIEW		A
SCALE: 1:2		



SECTION A-A
SCALE 1 : 3



UNLESS OTHERWISE SPECIFIED:

DIMENSIONS ARE IN INCHES
TOLERANCES:
FRACTIONAL: $\pm 1/8$
ANGULAR: MACH $\pm 1^\circ$ BEND $\pm 2^\circ$
TWO PLACE DECIMAL: ± 0.05
THREE PLACE DECIMAL: ± 0.005
TOLERANCING PER: MMC

TITLE:

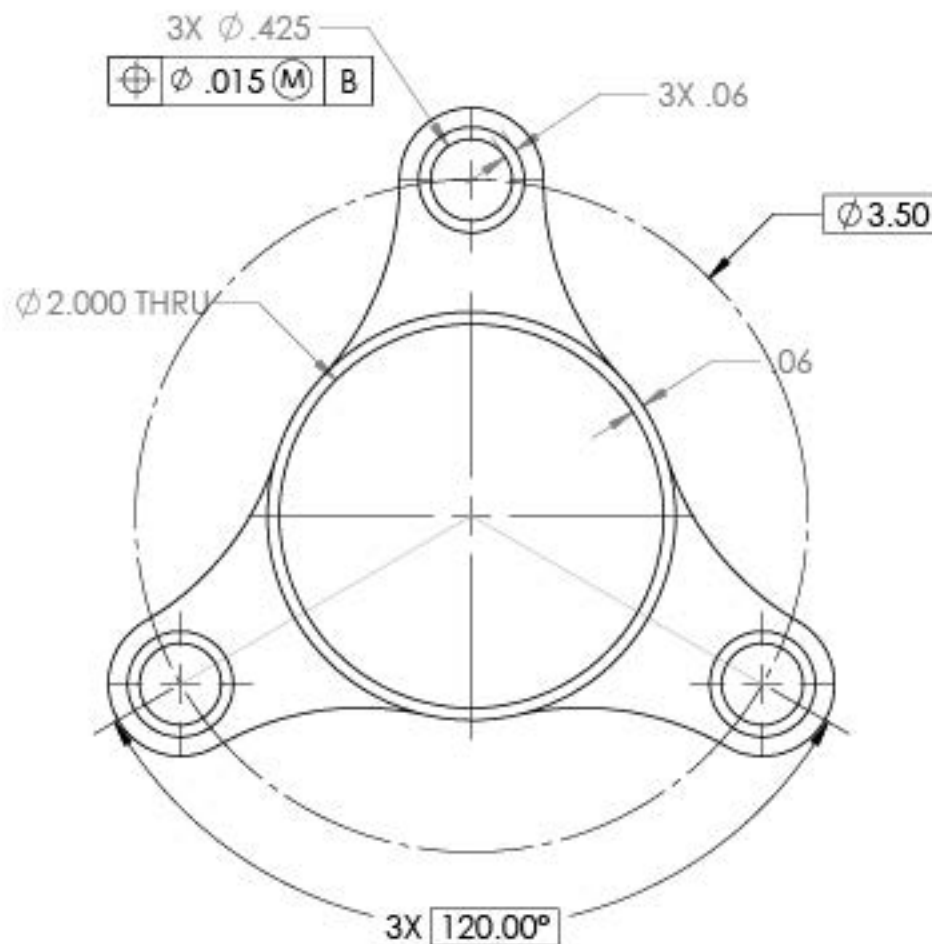
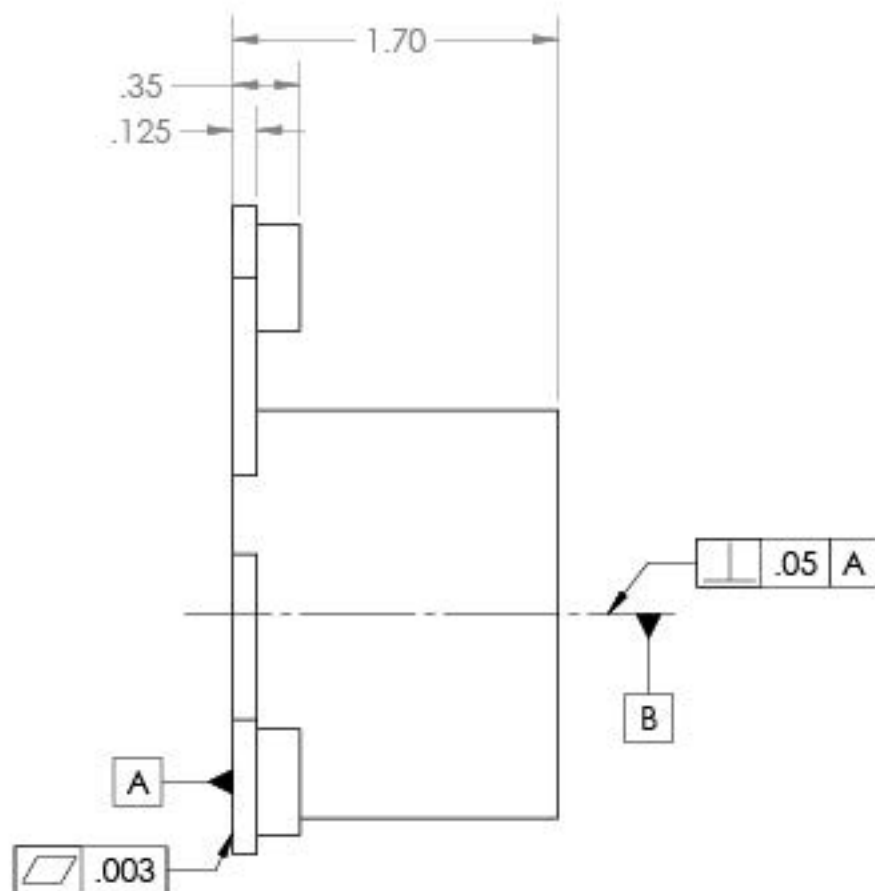
WHEEL

REV

A

SCALE: 1:3

NOTE:
ALL OTHER DIMENSIONS FROM CAD



UNLESS OTHERWISE SPECIFIED:

DIMENSIONS ARE IN INCHES

TOLERANCES:

FRACTIONAL: $\pm 1/8$

ANGULAR: MACH $\pm 1^\circ$ BEND $\pm 2^\circ$

TWO PLACE DECIMAL: ± 0.05

THREE PLACE DECIMAL: ± 0.005

TOLERANCING PER: MMC

TITLE:

CENTER RING

SCALE: 1:1

MATERIAL: 6061 AL

REV

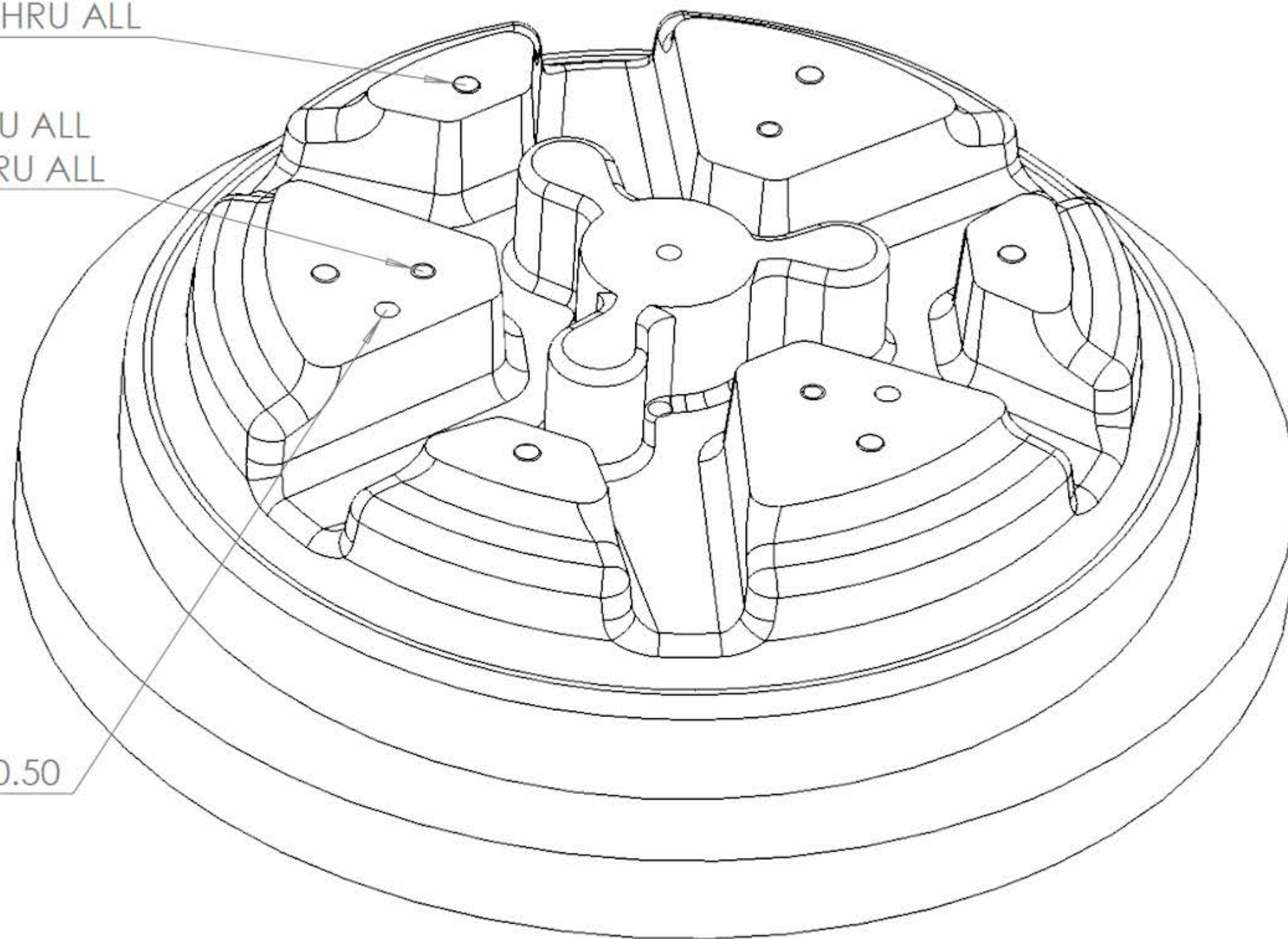
A

1 OF 1

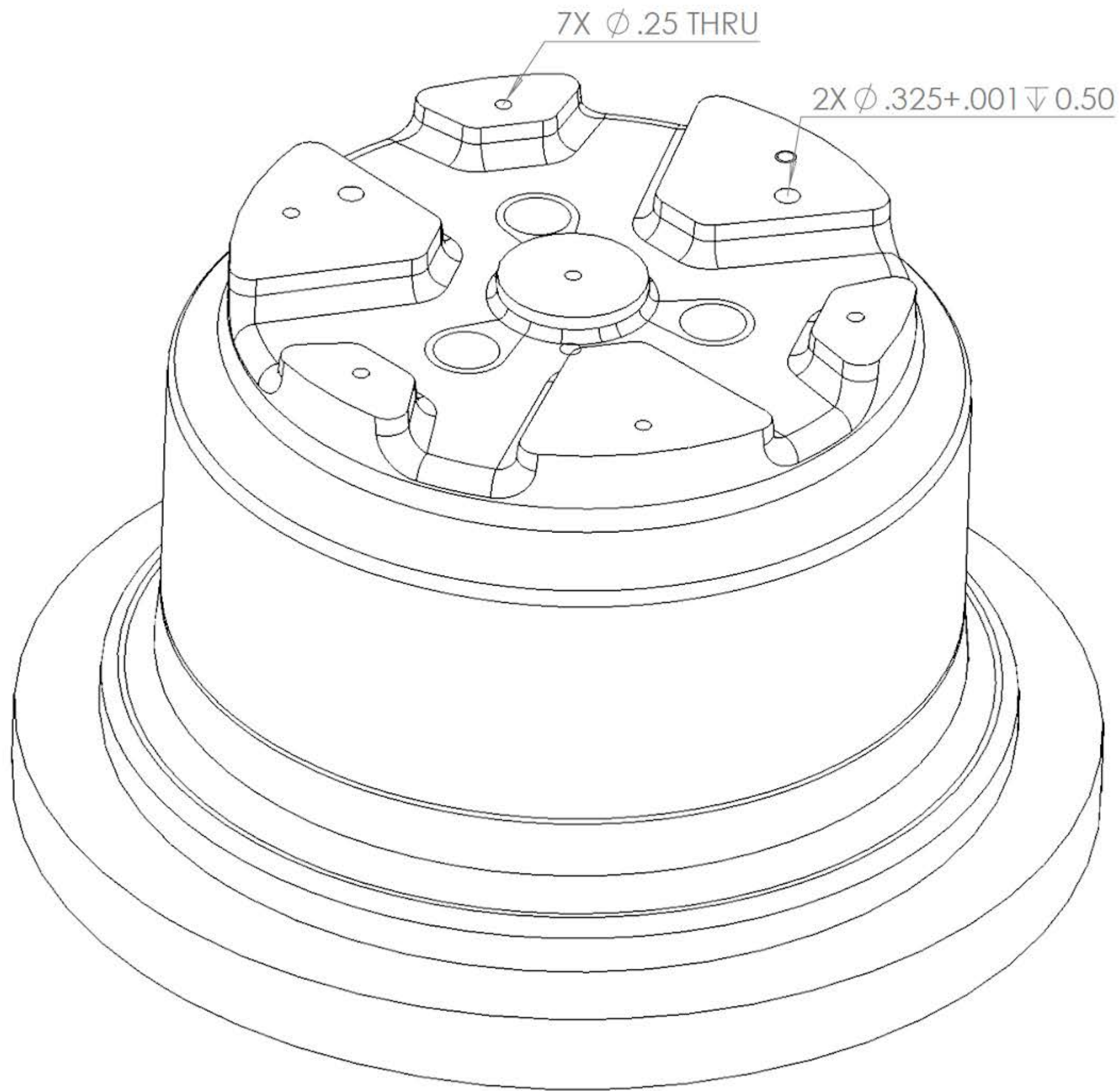
6 x ϕ 0.28 THRU ALL

4 x ϕ 0.20 THRU ALL
1/4-20 UNC THRU ALL

2X ϕ .250+ $\begin{smallmatrix} .005 \\ \nabla \end{smallmatrix}$ 0.50



SIZE	DWG. NO.	REV
A	Outboard Tool	
SCALE: 1:10	WEIGHT:	SHEET 1 OF 1



SIZE	DWG. NO.	REV
A	Inboard Tool	
SCALE: 1:10	WEIGHT:	SHEET 1 OF 1

APPENDIX B: QUALITY FUNCTION DEPLOYMENT

Reinventing the Wheel
Wheel Design

⊙ ○ △ □ ▽ ◇

Grouping	Voices	Item No.	Importance	Measures											Options				
				Weight	Rotational Inertia	Normal Load Stiffness	Lateral Stiffness	Max Pressure	Manufacturing Time	Number of Cycles to Failure	Cost	Maximum Normal Load	Maximum Longitudinal	Maximum Lateral Load	Bead Strength	Bead Stiffness	Surface Toughness	Delivery Date	
Performance	Inertia/Weight	1	5	9	9														Aluminum Center
	Stiffness	2	5			9	9												Composite
	Sealing	3	5			1	1	9							3				Keizer
	Strength	4	3									9	9	9	9				
	Life	5	3							9									
	Cost	6	3								9								
	Ease of Tire Mounting	7	1					3							9	9	9		
	Manufacturability	8	2						9									3	
Options	Total																		
	Aluminum Center				3	3	3	3	5	4	5	2	5	5	5	5	5	5	4
	Composite				5	5	5	5	4	2	3	2	5	5	5	4	4	2	2
	Keizer				3	3	3	1	5	5	5	2	5	5	5	5	5	4	5
																			708 781.25 760

Reinventing the Wheel
Number of Pieces

⊙ ○ △ □ ▽ ◇

Grouping	Voices	Item No.	Importance	Measures											Options				
				Weight	Rotational Inertia	Normal Load Stiffness	Lateral Stiffness	Max Pressure	Manufacturing Time	Number of Cycles to Failure	Cost	Maximum Normal Load	Maximum Longitudinal	Maximum Lateral Load	Bead Strength	Bead Stiffness	Surface Toughness	Delivery Date	
Performance	Inertia/Weight	1	5	9	9														One Piece
	Stiffness	2	5			9	9												Two Piece
	Sealing*	3	5			1	1	9							3				
	Strength	4	3									9	9	9	9				
	Life	5	3							9									
	Cost	6	3								9								
	Ease of Tire Mounting	7	1					3							9	9	9		
	Manufacturability	8	2						9									3	
Options	Total																		
	One Piece				5	5	5	5	4	2	3	5	5	5	5	4	4	2	1
	Two Piece				4	4	5	4	4	4	3	5	5	5	5	4	4	2	4
																			778.3 736.5

APPENDIX C: CALCULATIONS

C.1 Load Distribution

Below are sample excel tabs deploying the equations discussed in the Loads section. All sample tabs use values for max cornering, except for longitudinal loading. Longitudinal uses combined loading values. Adjust bead thickness until W (lb) is equal to the summed load check.

Tire Expansion Flange Load				
Inflated Pressure (psi)	r_tire (in)	r_flange (in)	Flange load per unit circumference (lb/in)	Total load on each flange (lb)
12.00	9.00	5.18	31.43	1022.01

Lateral Loading

r_bead (in)	r_tire (in)	t_bead (in)	theta_0	W_tire (lb)	W_flange (lb)	Pwo (psi)
4.86	9.00	0.66	0.70	-768.00	-1422.22	-502.62
Pressure Application Area (in^2)	0.22					
Pressure Distribution						
Pwo (psi)	theta_w (deg)	theta_o (deg)	Pw (psi)	Reiman Sum Pressure (psi)	Load Check (lbs)	Reiman Sum Load (lb)
-502.62	0.00	40.00	-502.62	-501.27	-54.91	-219.06
-502.62	1.00	40.00	-502.24		-54.87	0.00
-502.62	2.00	40.00	-501.07		-54.74	0.00
-502.62	3.00	40.00	-499.14		-54.53	0.00
-502.62	4.00	40.00	-496.43	-490.47	-54.24	-214.35
-502.62	5.00	40.00	-492.97		-53.86	0.00
-502.62	6.00	40.00	-488.74		-53.40	0.00
-502.62	7.00	40.00	-483.75		-52.85	0.00
-502.62	8.00	40.00	-478.02	-467.60	-52.23	-204.35
-502.62	9.00	40.00	-471.56		-51.52	0.00
-502.62	10.00	40.00	-464.36		-50.73	0.00
-502.62	11.00	40.00	-456.45		-49.87	0.00
-502.62	12.00	40.00	-447.84	-433.21	-48.93	-189.32
-502.62	13.00	40.00	-438.54		-47.91	0.00
-502.62	14.00	40.00	-428.56		-46.82	0.00
-502.62	15.00	40.00	-417.92		-45.66	0.00
-502.62	16.00	40.00	-406.63	-388.16	-44.43	-169.63
-502.62	17.00	40.00	-394.72		-43.12	0.00
-502.62	18.00	40.00	-382.20		-41.76	0.00
-502.62	19.00	40.00	-369.09		-40.32	0.00
-502.62	20.00	40.00	-355.41	-333.55	-38.83	-145.77
-502.62	21.00	40.00	-341.18		-37.28	0.00
-502.62	22.00	40.00	-326.43		-35.66	0.00
-502.62	23.00	40.00	-311.17		-34.00	0.00
-502.62	24.00	40.00	-295.43	-270.72	-32.28	-118.31
-502.62	25.00	40.00	-279.24		-30.51	0.00
-502.62	26.00	40.00	-262.62		-28.69	0.00
-502.62	27.00	40.00	-245.59		-26.83	0.00
-502.62	28.00	40.00	-228.19	-201.23	-24.93	-87.94
-502.62	29.00	40.00	-210.43		-22.99	0.00
-502.62	30.00	40.00	-192.35		-21.01	0.00
-502.62	31.00	40.00	-173.97		-19.01	0.00
-502.62	32.00	40.00	-155.32	-126.79	-16.97	-55.41
-502.62	33.00	40.00	-136.43		-14.91	0.00
-502.62	34.00	40.00	-117.34		-12.82	0.00
-502.62	35.00	40.00	-98.06		-10.71	0.00
-502.62	36.00	40.00	-78.63	-39.37	-8.59	-17.21
-502.62	37.00	40.00	-59.08		-6.45	0.00
-502.62	38.00	40.00	-39.44		-4.31	0.00
-502.62	39.00	40.00	-19.73		-2.16	0.00
-502.62	40.00	40.00	0.00		0.00	0.00
				Total Load (lbs)	-1425.65	-1421.35

Longitudinal Loading						
r bead (in)	t bead (in)	theta_0	W, One side of wheel (lb)	Pwo (psi)		
4.86	0.54	0.70	277.50	120.07		
r_tire (in)	Longitudinal load (lb)	Torque to be applied to entire bead (in*lb)				
9.00	555.00	4995.00				
Pressure Application Area (in^2)	0.18					
Pressure Distribution						
Pwo (psi)	theta_w (deg)	theta_o (deg)	Pw (psi)	Reiman Sum Pressure (psi)	Load Check (lbs)	Reiman Sum Load (lb)
120.07	0.00	40.00	120.07	119.74	10.73	42.80
120.07	1.00	40.00	119.97		10.72	0.00
120.07	2.00	40.00	119.70		10.69	0.00
120.07	3.00	40.00	119.24		10.65	0.00
120.07	4.00	40.00	118.59	117.16	10.60	41.87
120.07	5.00	40.00	117.76		10.52	0.00
120.07	6.00	40.00	116.75		10.43	0.00
120.07	7.00	40.00	115.56		10.33	0.00
120.07	8.00	40.00	114.19	111.70	10.20	39.92
120.07	9.00	40.00	112.65		10.06	0.00
120.07	10.00	40.00	110.93		9.91	0.00
120.07	11.00	40.00	109.04		9.74	0.00
120.07	12.00	40.00	106.98	103.49	9.56	36.99
120.07	13.00	40.00	104.76		9.36	0.00
120.07	14.00	40.00	102.37		9.15	0.00
120.07	15.00	40.00	99.83		8.92	0.00
120.07	16.00	40.00	97.14	92.72	8.68	33.14
120.07	17.00	40.00	94.29		8.42	0.00
120.07	18.00	40.00	91.30		8.16	0.00
120.07	19.00	40.00	88.17		7.88	0.00
120.07	20.00	40.00	84.90	79.68	7.59	28.48
120.07	21.00	40.00	81.50		7.28	0.00
120.07	22.00	40.00	77.98		6.97	0.00
120.07	23.00	40.00	74.33		6.64	0.00
120.07	24.00	40.00	70.57	64.67	6.31	23.11
120.07	25.00	40.00	66.71		5.96	0.00
120.07	26.00	40.00	62.74		5.61	0.00
120.07	27.00	40.00	58.67		5.24	0.00
120.07	28.00	40.00	54.51	48.07	4.87	17.18
120.07	29.00	40.00	50.27		4.49	0.00
120.07	30.00	40.00	45.95		4.11	0.00
120.07	31.00	40.00	41.56		3.71	0.00
120.07	32.00	40.00	37.10	30.29	3.32	10.82
120.07	33.00	40.00	32.59		2.91	0.00
120.07	34.00	40.00	28.03		2.50	0.00
120.07	35.00	40.00	23.42		2.09	0.00
120.07	36.00	40.00	18.78	9.41	1.68	3.36
120.07	37.00	40.00	14.11		1.26	0.00
120.07	38.00	40.00	9.42		0.84	0.00
120.07	39.00	40.00	4.71		0.42	0.00
120.07	40.00	40.00	0.00		0.00	0.00
				Total Load (lbs)	278.52	277.68

Normal Loading						
r_bead (in)	t_bead (in)	theta_0	W, One side of wheel (lb)	Pwo (psi)		
4.86	0.54	0.70	168.50	72.91		
Pressure Application Area (in^2)	0.18					
Pressure Distribution						
Pwo (psi)	theta_w (deg)	theta_o (deg)	Pw (psi)	Reiman Sum Pressure (psi)	Load Check (lbs)	Reiman Sum Load (lb)
72.91	0.00	40.00	72.91	72.71	6.51	25.99
72.91	1.00	40.00	72.85		6.51	0.00
72.91	2.00	40.00	72.68		6.49	0.00
72.91	3.00	40.00	72.40		6.47	0.00
72.91	4.00	40.00	72.01	71.14	6.43	25.43
72.91	5.00	40.00	71.50		6.39	0.00
72.91	6.00	40.00	70.89		6.33	0.00
72.91	7.00	40.00	70.17		6.27	0.00
72.91	8.00	40.00	69.34	67.83	6.20	24.24
72.91	9.00	40.00	68.40		6.11	0.00
72.91	10.00	40.00	67.36		6.02	0.00
72.91	11.00	40.00	66.21		5.92	0.00
72.91	12.00	40.00	64.96	62.84	5.80	22.46
72.91	13.00	40.00	63.61		5.68	0.00
72.91	14.00	40.00	62.16		5.55	0.00
72.91	15.00	40.00	60.62		5.42	0.00
72.91	16.00	40.00	58.98	56.30	5.27	20.12
72.91	17.00	40.00	57.25		5.12	0.00
72.91	18.00	40.00	55.44		4.95	0.00
72.91	19.00	40.00	53.54		4.78	0.00
72.91	20.00	40.00	51.55	48.38	4.61	17.29
72.91	21.00	40.00	49.49		4.42	0.00
72.91	22.00	40.00	47.35		4.23	0.00
72.91	23.00	40.00	45.14		4.03	0.00
72.91	24.00	40.00	42.85	39.27	3.83	14.03
72.91	25.00	40.00	40.50		3.62	0.00
72.91	26.00	40.00	38.09		3.40	0.00
72.91	27.00	40.00	35.62		3.18	0.00
72.91	28.00	40.00	33.10	29.19	2.96	10.43
72.91	29.00	40.00	30.52		2.73	0.00
72.91	30.00	40.00	27.90		2.49	0.00
72.91	31.00	40.00	25.23		2.25	0.00
72.91	32.00	40.00	22.53	18.39	2.01	6.57
72.91	33.00	40.00	19.79		1.77	0.00
72.91	34.00	40.00	17.02		1.52	0.00
72.91	35.00	40.00	14.22		1.27	0.00
72.91	36.00	40.00	11.40	5.71	1.02	2.04
72.91	37.00	40.00	8.57		0.77	0.00
72.91	38.00	40.00	5.72		0.51	0.00
72.91	39.00	40.00	2.86		0.26	0.00
72.91	40.00	40.00	0.00		0.00	0.00
				Total Load (lbs)	169.12	168.61

Table of Contents

.....	1
Section 1: Flat Plate	1
Section 2: Tapered U Channel	1
Section 3: Pipe-Section	2
Section 4: Rectangular Tube	2
Section 5: Straight U Channel	2
Stiffness Vs. Area Comparison of Geometries	2
Plotting Relationship Between Thickness "t" and Bending Area Efficiency	3

%Note: All geometries considered to be thickness "t"
% Geometries compared based on specific stiffness
% All units of length are in inches, mass in pounds-mass, stiffness in

Section 1: Flat Plate

```
t=.1; % Thickness, inches
B=1; %Channel Width, inches

AreaPlate=t*B;

IxPlate=(1/12)*B*(t^3); %Moment of Inertia, X axis
IyPlate=(1/12)*t*(B^3); %Moment of Inertia, Y axis
```

Section 2: Tapered U Channel

```
A=4; %Section Height, inches
B=8; %Channel Width, inches
Theta=45; %Theta, Degrees
TanTheta=tan(Theta*pi()/180);
C=(A-t)/cos(Theta*pi()/180); %Hypotenuse of Leg, inches
D=t*(tan(Theta*pi()/180));

AreaLegUChannel=C*t;
YLegUChannel=(A-t)/2;
AreaCenterUChannel=t*B;
YCenterUChannel=A-(t/2);
AreaTriangleUChannel=(D*t)/2;
YTriangleUChannel=A-(2*t/3);

AreaTotalUChannel=(2*(AreaLegUChannel
+AreaTriangleUChannel))+AreaCenterUChannel;
YUChannel=(( (AreaLegUChannel*YLegUChannel)+(AreaTriangleUChannel*YTriangleUChannel)
AreaTotalUChannel;

IxCenterUChannel=((1/12)*B*(t^3))+AreaCenterUChannel*((YCenterUChannel-
YUChannel)^2);
IxLegUChannel=((1/12)*D*((A-t)^3))+AreaLegUChannel*((YLegUChannel-
YUChannel)^2);
```

```

IxTriangleUChannel=((1/36)*D*(t^3))+(AreaTriangleUChannel*((YTriangleUChannel-
YUChannel)^2));

IxUChannel=IxCenterUChannel+(2*(IxLegUChannel+IxTriangleUChannel));

% IyUChannel=0

```

Section 3: Pipe-Section

```

D=1; d=1-t; IxPipe=(pi()/64)*((D^4)-(d^4)); APipe=(pi()/4)*((D^2)-(d^2));

```

Section 4: Rectangular Tube

```

LOuter=1; %Length, Outer, Rectangular tube, Inches
WOuter=1; %Width, Outer, Rectangular tube, Inches
LInner=LOuter-t; %Length, Inner, Rectangular tube, Inches
WInner=WOuter-t; %Width, Inner, Rectangular tube, Inches

IxOuter=(1/12)*WOuter*(LOuter^3); %Moment of Inertia, Outer X axis
IxInner=(1/12)*WInner*(LInner^3); %Moment of Inertia, Inner, X axis
IxRectangularTube=IxOuter-IxInner; %Moment of Inertia, Rectangular
Tube, X axis
AreaRectangularTube=(WOuter*LOuter)-(WInner*LInner);
StiffnessAreaRatioRectangularTube=IxRectangularTube/
AreaRectangularTube;

```

Section 5: Straight U Channel

```

A=1; %Height, Straight U Channel, Inches
B=1; %Width, Straight U Channel, Inches

yib=A-(t/2);
Ab=t*(B-(2*t));

yia=(A/2);
Aa=A*t;
AreaStraightUChannel=Ab+(2*Aa);
YBarStraightUChannel=((Ab*yib)+(2*(Aa*yia)))/AreaStraightUChannel;

IbxStraightUChannel=((1/12)*(B-(2*t))*(t^3))+(Ab*((yib-
YBarStraightUChannel)^2));
IaxStraightUChannel=((1/12)*(t)*(B^3))+(Aa*((yia-
YBarStraightUChannel)^2));
IxStraightUChannel=IbxStraightUChannel+(2*IaxStraightUChannel);

StiffnessAreaRatioStraightUchannel=IxStraightUChannel/
AreaStraightUChannel;

```

Stiffness Vs. Area Comparison of Geometries

```

StiffnessAreaRatioPlate=IxPlate/AreaPlate;

```

```
StiffnessAreaRatioUChannel=IxUChannel/AreaTotalUChannel;
```

Plotting Relationship Between Thickness "t" and Bending Area Efficiency

```
t=[.01:.01:.1] %thickness values [start:step:stop]

% C=zeros(length(t));
% D=zeros(length(t));
% AreaLegUChannel=zeros(length(t));
% YLegUChannel=zeros(length(t));
% AreaCenterUChannel=zeros(length(t));
% YCenterUChannel=zeros(length(t));
% AreaTriangleUChannel=zeros(length(t));
% YTriangleUChannel=zeros(length(t));

% AreaTotalUChannel=zeros(length(t));
% YUChannel=zeros(length(t));
% IxCenterUChannel=zeros(length(t));
% IxLegUChannel=zeros(length(t));
% IxTriangleUChannel=zeros(length(t));
% IxUChannel=zeros(length(t));
% AreaPlate=zeros(length(t));
% IxPlate=zeros(length(t));

StiffnessAreaRatioUChannel=zeros(length(t));
StiffnessAreaRatioPlate=zeros(length(t));
StiffnessAreaRatioPipe=zeros(length(t));
StiffnessAreaRatioRectangularTube=zeros(length(t));
StiffnessAreaRatioStraightUchannel=zeros(length(t));

for i=1:length(t)

    A=2; %Section Height, inches
    B=2; %Channel Width, inches
    Theta=45; %Theta, Degrees
    TanTheta=tan(Theta*pi()/180);
    C(i)=(A-t(i))/cos(Theta*pi()/180); %Hypotenuse of Leg, inches
    D(i)=t(i)*(tan(Theta*pi()/180));

    AreaLegUChannel=C*t(i);
    YLegUChannel=(A-t(i))/2;
    AreaCenterUChannel=t(i)*B;
    YCenterUChannel=A-(t(i)/2);
    AreaTriangleUChannel=(D*t(i))/2;
    YTriangleUChannel=A-(2*t(i)/3);

    AreaTotalUChannel=(2*(AreaLegUChannel
+AreaTriangleUChannel))+AreaCenterUChannel;

    YUChannel=(( (AreaLegUChannel*YLegUChannel)+(AreaTriangleUChannel*YTriangleUChannel))+AreaCenterUChannel);
```

```

IxCenterUChannel=((1/12)*B*(t(i)^3))+(AreaCenterUChannel*((YCenterUChannel-
YUChannel)^2));
IxLegUChannel=((1/12)*D*((A-
t(i))^3))+(AreaLegUChannel*((YLegUChannel-YUChannel)^2));

IxTriangleUChannel=((1/12)*D*(t(i)^3))+(AreaTriangleUChannel*((YTriangleUChannel-
YUChannel)^2));

IxUChannel=IxCenterUChannel+2*(IxLegUChannel+IxTriangleUChannel);

%Plate
AreaPlate=t(i)*B;

IxPlate=(1/12)*B*(t(i)^3);

%Pipe
DiameterOuterPipe=2;
DiameterInnerPipe=DiameterOuterPipe-t(i);
IxPipe=(pi()/64)*((DiameterOuterPipe^4)-(DiameterInnerPipe^4));
APipe=(pi()/4)*((DiameterOuterPipe^2)-(DiameterInnerPipe^2));

%Rectangular Tube
LOuter=2; %Length, Outer, Rectangular tube, Inches
WOuter=2; %Width, Outer, Rectangular tube, Inches
LInner=LOuter-t(i); %Length, Inner, Rectangular tube, Inches
WInner=WOuter-t(i); %Width, Inner, Rectangular tube, Inches

IxOuter=(1/12)*WOuter*(LOuter^3); %Moment of Inertia, Outer X axis
IxInner=(1/12)*WInner*(LInner^3); %Moment of Inertia, Inner, X
axis
IxRectangularTube=IxOuter-IxInner; %Moment of Inertia, Rectangular
Tube, X axis
AreaRectangularTube=(WOuter*LOuter)-(WInner*LInner); %Area,
Rectangular Tube

%Straight U Channel
yib=A-(t(i)/2);
Ab=t*(B-(2*t(i)));

yia=(A/2);
Aa=A*t(i);

AreaStraightUChannel=Ab+(2*Aa);
YBarStraightUChannel=((Ab*yib)+(2*(Aa*yia)))/AreaStraightUChannel;

IbxStraightUChannel=((1/12)*(B-(2*t(i)))*(t(i)^3))+(Ab*((yib-
YBarStraightUChannel)^2));
IaxStraightUChannel=((1/12)*(t(i))*(B^3))+(Aa*((yia-
YBarStraightUChannel)^2));
IxStraightUChannel=IbxStraightUChannel+(2*IaxStraightUChannel);

```

```

    %Ratios
    StiffnessAreaRatioPlate(i)=IxPlate/AreaPlate;
    StiffnessAreaRatioUChannel(i)=IxUChannel/AreaTotalUChannel;
    StiffnessAreaRatioPipe(i)=IxPipe/APipe;
    StiffnessAreaRatioRectangularTube(i)=IxRectangularTube/
AreaRectangularTube;
    StiffnessAreaRatioStraightUchannel(i)=IxStraightUChannel/
AreaStraightUChannel;

end

% figure
% plot(t,IxPlate(1,:));
% xlabel('thickness');
% ylabel('Moment Of Inertia, Plate');
% title('Stiffness of Plate, I');

figure

subplot(5,1,1);

% Set Figure Dimensions
x0=10;
y0=10;
width=800;
height=800;
set(gcf,'position',[x0,y0,width,height])

TStiffnessAreaRatioUChannel=transpose(StiffnessAreaRatioUChannel);
plot(t,TStiffnessAreaRatioUChannel(1,:));
xlabel('Thickness');
ylabel('Stiffness/Area');
title('Channel Stiffness Ratio');

subplot(5,1,2)
TStiffnessAreaRatioPlate=transpose(StiffnessAreaRatioPlate);
plot(t,TStiffnessAreaRatioPlate(1,:));
xlabel('Thickness');
ylabel('Stiffness/Area');
title('Plate Stiffness Ratio');

subplot(5,1,3)
TStiffnessAreaRatioPipe=transpose(StiffnessAreaRatioPipe);
plot(t,TStiffnessAreaRatioPipe(1,:));
xlabel('Thickness');
ylabel('Stiffness/Area');
title('Pipe Stiffness Ratio');

subplot(5,1,4)
TStiffnessAreaRatioRectangularTube=transpose(StiffnessAreaRatioRectangularTube);
plot(t,TStiffnessAreaRatioRectangularTube(1,:));
xlabel('Thickness');
ylabel('Stiffness/Area');

```

```
title('Rectangular Tube Ratio');

subplot(5,1,5)
TStiffnessAreaRatioStraightUchannel=transpose(StiffnessAreaRatioStraightUchannel);
plot(t,TStiffnessAreaRatioStraightUchannel(1,:));
xlabel('Thickness');
ylabel('Stiffness/Area');
title('U-Channel Ratio');
```

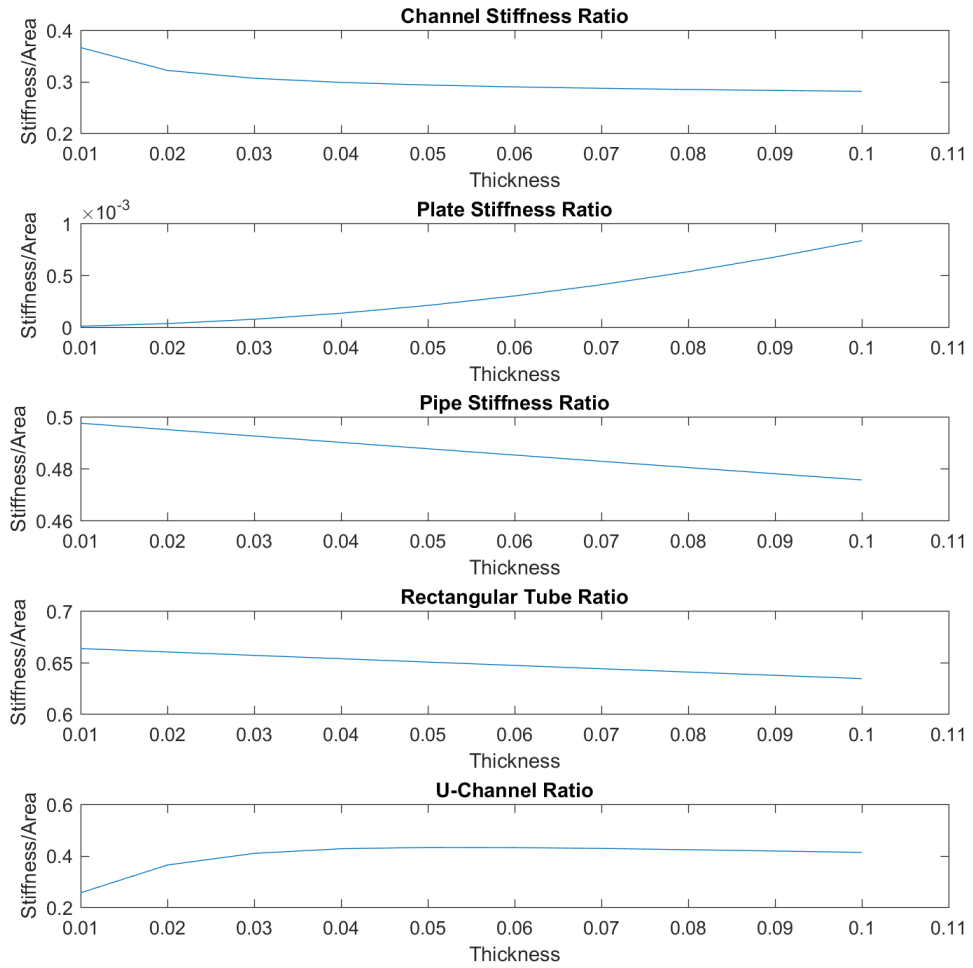
```
t =
```

```
Columns 1 through 7
```

```
0.0100    0.0200    0.0300    0.0400    0.0500    0.0600    0.0700
```

```
Columns 8 through 10
```

```
0.0800    0.0900    0.1000
```



Published with MATLAB® R2017a

ABD code, determines laminate properties

```
%Given Ply number, ply angle, thickness of each ply, output strain
matrix.
clc;
clear all;

%Unidirectional Properties M46J (from test data)
E1 = 198372.0949E6; %longitudinal modulus Pa
E2 = 5423.877867E6; %transverse modulus Pa
G12 = 3297.993533E6; %shear modulus Pa
v12 = 0.2257142857; %poissons ratio
a(1,1) = 0; %first angle
nplies = 12; %number of plies in laminate
tplies(1,1) = 0.2918E-3; %thickness of single ply

% %Cloth Properties HTS40
% E1c = 181E9; %longitudinal modulus Pa
% E2c = 10.3E9; %transverse modulus Pa
% G12c = 7.17E9; %shear modulus Pa
% v12c = .28; %poissons ratio

%quasi isotropic angle ply angle array
for i = 2:1:nplies
    % x = pi()/nplies;
    % a(1,i) = a(1,i-1)+x;
    tplies(1,i) = tplies(1,1);
end
% a = [0 60 -60 0 60 -60 -60 60 0 -60 60 0];
% a = [0 45 -45 90 0 45 -45 90 0 45 -45 90 ];
a = [0 30 -60 90 60 -30 0 30 -60 90 60 -30];
%3 Dimensional stiffness matrix for each ply (uni)
for i=1:1:nplies
    Qz(:, :, i) = Qa(E1,E2,G12,v12,a(1,i));
end
% %Cloth Stiffness matrices
% Qz(:, :, 1) = Qa(E1c,E2c,G12c,v12c,a(1,i));
% Qz(:, :, nplies) = Qa(E1c,E2c,G12c,v12c,a(1,i));

%Total thickness of laminate
t = sum(tplies);

%position of top and bottom of each lamina
h(1)=-t/2;
for i=2:1:nplies+1
    h(i)=h(i-1)+tplies(i-1);
end

%extensional, coupling, and bending stiffness matrix
A=0;
d=0;
b=0;
```

```

for i=1:1:nplies
    h1(1,i)=(h(i+1)-h(i));
    h2(1,i)=(h(i+1)^2-h(i)^2);
    h3(1,i)=(h(i+1)^3-h(i)^3);
    A=A+(Qz(:, :, i)*h1(1,i));
    b=b+(Qz(:, :, i)*h2(1,i));
    d=d+(Qz(:, :, i)*h3(1,i));
end
%Multiplication due to integration
B=.5*b;
D=(1/3)*d;

ABD = [A B; B D];
N = [1000; 1000; 0; 0; 0; 0]; %[Nx;Ny;Nxy;Mx;My;Mxy]
e = (ABD^-1)*N; %Mid plane strains and curvatures,
    [ex;ey;exy;kx;ky;kxy]
As = A^-1; %A star
Ds = D^-1; %D star

%Flexural Engineering Constants of Laminate
Ex = 0.000145038*12/((t^3)*Ds(1,1)); % psi
Ey = 0.000145038*12/((t^3)*Ds(2,2)); % psi
Gxy = 0.000145038*12/((t^3)*Ds(3,3)); % psi
vxy = -Ds(1,2)/Ds(1,1); %Poissons ratio
vyx = -Ds(1,2)/Ds(2,2); %Poissons ratio

```

Plate Analysis

```

th = 39.3701*t; %thickness conversion from (m) to (in)
a = (9.44/2); %distance to outer edge in
b = 2.6/2; %distance to inner edge in
ro = 1.97; %position of load w in
F = 1000; %total load lbs
w = F/(2*pi()*ro); %unit line load lb/in of circumference
D = Ex*(th^3)/(12*(1-vxy^2));
C1 = (((1+vxy)/2)*(b/a)*log(a/b))+(((1-vxy)/4)*((a/b)-(b/a)));
C7 = .5*(1-vxy^2)*((a/b)-(b/a));
L3 = (ro/(4*a))*((((ro/a)^2)+1)*log(a/ro))+((ro/a)^2)-1;
L9 = (ro/a)*((((1+vxy)/2)*log(a/ro))+(((1-vxy)/4)*(1-(ro/a)^2)));
ymax = -(w*(a^3)/D)*((C1*L9/C7)-L3);

rho = 0.055; %density (lbm/in^3)(taken from composites lab burnout
    test)
Area = pi()*((a^2)-(b^2));
m = rho*Area*th; %mass lbs
k = F/ymax; %Stiffness
ka = k/m; %Stiffness normalized by mass

```

Published with MATLAB® R2018a

ABD code, determines laminate properties

```
%Given Ply number, ply angle, thickness of each ply, output strain
matrix.
clc;
clear all;

%Unidirectional Properties M46J (from test data)
E1 = 198372.0949E6; %longitudinal modulus Pa
E2 = 5423.877867E6; %transverse modulus Pa
G12 = 3297.993533E6; %shear modulus Pa
v12 = 0.2257142857; %poissons ratio

%Cloth Properties HTS40
E1c = 7.515272E10; %longitudinal modulus Pa
E2c = 7.515272E10; %transverse modulus Pa
G12c = 7.17E9; %shear modulus Pa
v12c = .25; %poissons ratio

a = [0 -45 45 0 0 0 0 45 -45 0]; %array of fiber orientation of each
ply
% a = [90 0 0 0 0 0 0 0 0 0 0 90];
nplies = 10; %number of plies in laminate
tplies = [0.2555E-3 0.2918E-3 0.2918E-3 0.2918E-3 0.2918E-3 0.2918E-3
0.2918E-3 0.2918E-3 0.2918E-3 0.2555E-3]; %thickness of each ply (m)

%3 Dimensional stiffness matrix for each ply (uni)
for i=2:1:nplies-1
Qz(:, :, i) = Qa(E1, E2, G12, v12, a(1, i));
end
%Cloth Stiffness matrices
Qz(:, :, 1) = Qa(E1c, E2c, G12c, v12c, a(1, 1));
Qz(:, :, nplies) = Qa(E1c, E2c, G12c, v12c, a(1, nplies));

%Total thickness of laminate
t = sum(tplies);

%position of top and bottom of each lamina
h(1)=-t/2;
for i=2:1:nplies+1
h(i)=h(i-1)+tplies(i-1);
end

%extensional, coupling, and bending stiffness matrix
A=0;
d=0;
b=0;
for i=1:1:nplies
h1(1,i)=(h(i+1)-h(i));
h2(1,i)=(h(i+1)^2-h(i)^2);
h3(1,i)=(h(i+1)^3-h(i)^3);
A=A+(Qz(:, :, i)*h1(1,i));
```

```

        b=b+(Qz(:, :, i)*h2(1,i));
        d=d+(Qz(:, :, i)*h3(1,i));
    end
    %Multiplication due to integration
    B=.5*b;
    D=(1/3)*d;

    ABD = [A B; B D];
    N = [1000; 1000; 0; 0; 0; 0]; %[Nx;Ny;Nxy;Mx;My;Mxy]
    e = (ABD^-1)*N; %Mid plane strains and curvatures,
        [ex;ey;exy;kx;ky;kxy]
    As = A^-1; %A star
    Ds = D^-1; %D star

    %In Plane Engineering Constants of Laminate
    Ex = 0.000145038*1/(t*As(1,1)); %Effective longitudinal modulus (psi)
    Ey = 0.000145038*1/(t*As(2,2)); %Effective transverse modulus (psi)
    Gxy = 0.000145038*1/(t*As(3,3)); %Effective shear modulus (psi)
    vxy = -As(1,2)/As(1,1); %Poissons ratio
    vyx = -As(1,2)/As(2,2); %Poissons ratio

    %Flexural Engineering Constants of Laminate
    Efx = 0.000145038*12/((t^3)*Ds(1,1)); % psi
    Efy = 0.000145038*12/((t^3)*Ds(2,2)); % psi
    Gfxy = 0.000145038*12/((t^3)*Ds(3,3)); % psi
    vfx = -Ds(1,2)/Ds(1,1); %Poissons ratio
    vfy = -Ds(1,2)/Ds(2,2); %Poissons ratio

```

Beam Analysis of Spoke

```

F = 1000; %Total load (lbs)
th = 39.3701*t; %thickness conversion from (m) to (in)
rho = 0.055; %density (lbm/in^3)(taken from composites lab burnout
    test)
n(1,1) = 2; %Number of spokes
b = 1; %base of spoke (in)
h = 1; %height of spoke (in)
A = (b*h)-((b-th)*(h-th)); %spoke cross sectional area in^2
x = pi()*((2.65^2)-(1.3^2))*rho*th; %mass of remainder of wheel center
    lbm
L = 2.76; %Effective length of spoke (in)
I = ((1/12)*b*h^3)-((1/12)*(b-(2*t))*(h-(2*t))^3); %inertia of spoke
    cross section
y = 0;

%Iterating for multiple spoke numbers
for i = 2:1:10
    n(1,i) = n(1,i-1)+1; %spoke number
    R(1,i) = F/n(1,i); %Force resolved at one spoke
    y(1,i) = (R(1,i)*L^3)/(3*Efx*I); %Deflection due to bending
    k(1,i) = F/y(1,i); %Stiffness lb/in
    ms(1,i) = L*rho*n(1,i)*A*L; %mass of spokes lbm
    ka(1,i) = k(1,i)/(ms(1,i)+x); %Stiffness normalized by mass

```

end

Published with MATLAB® R2018a

C.5 Stiffness Matrix Function

```
%Stiffness matrix function

function Qb = Qa(E1,E2,G12,v12,a)

t= a*pi()/180;
c = cos(t);
s = sin(t);

T = [c.^2 s.^2 (2*s*c);...
     s.^2 c.^2 (-2*s*c);...
     (-s*c) (s*c) ((c.^2)-(s.^2))];

S = [(1/E1) (-v12/E1) 0;... %Compliance Matrix
     (-v12/E1) (1/E2) 0;...
     0 0 (1/G12)];
R = [1 0 0; 0 1 0; 0 0 2];
Sb = R*(T^(-1))*(R^(-1))*S*T;
Qb = Sb^(-1);
end

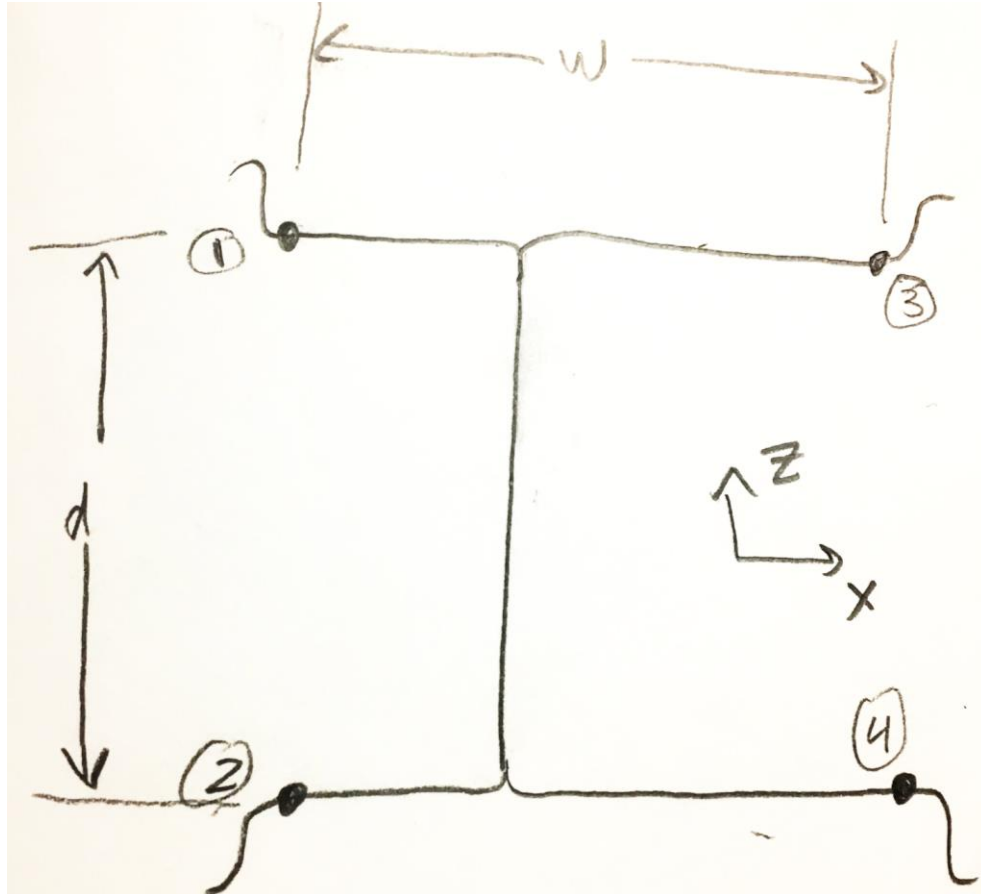
Not enough input arguments.

Error in Qa (line 5)
t= a*pi()/180;

Published with MATLAB® R2018a
```

C.6 Camber Deflection Calculation

To calculate camber deflection, two types of deflections described by the equations below are summed. A probe is used at each point in FEA to output deflections in each direction.



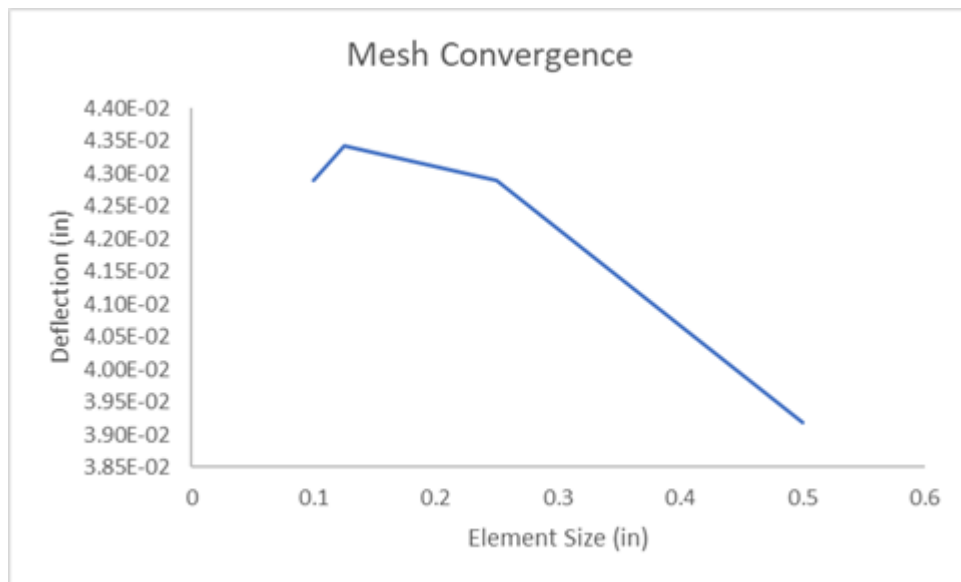
$$\text{Deflection 1} = \frac{\left| \frac{3z + 4z}{2} - \frac{1z + 2z}{2} \right|}{w} * \frac{180}{\pi}$$

$$\text{Deflection 2} = |(4x - 3x) + (2x - 1x)| * \frac{180}{2\pi d}$$

$$\text{Total Deflection} = \text{Deflection 1} + \text{Deflection 2}$$

C.7 FEA Meshing

A mesh convergence study was performed to determine an appropriate mesh resolution. A 0.125" quad element size was used due to the resulting plot below. In the FE software used, Ansys, one can define "soft" body sizing in conjunction with an auto mesh that appropriately decides element type. This means that the program attempts to assign 0.125" element sizing where possible, in a combination of primarily quad and a small percentage of triangular shell elements. For solids, tetrahedrals are used. This auto meshing strategy saves time, and was within 2-3% of the converged deflection output below. Therefore this mesh was used for all analysis.

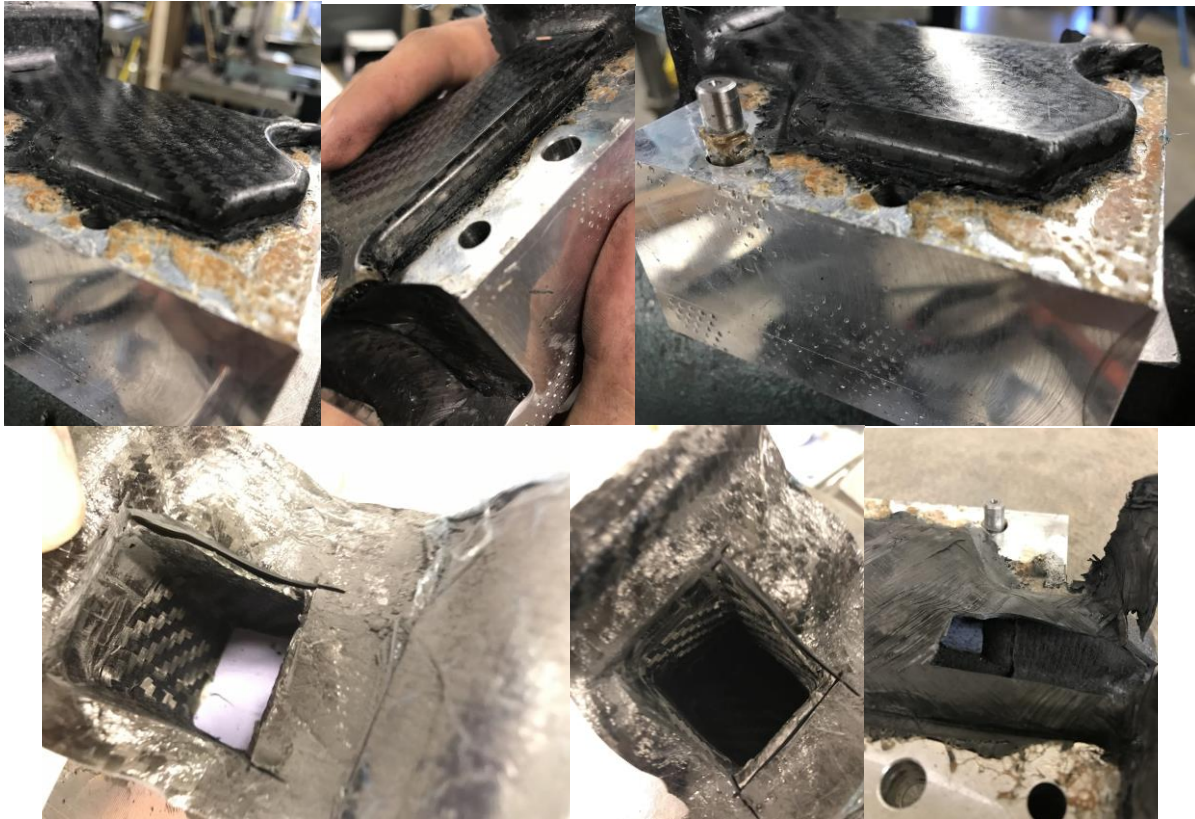


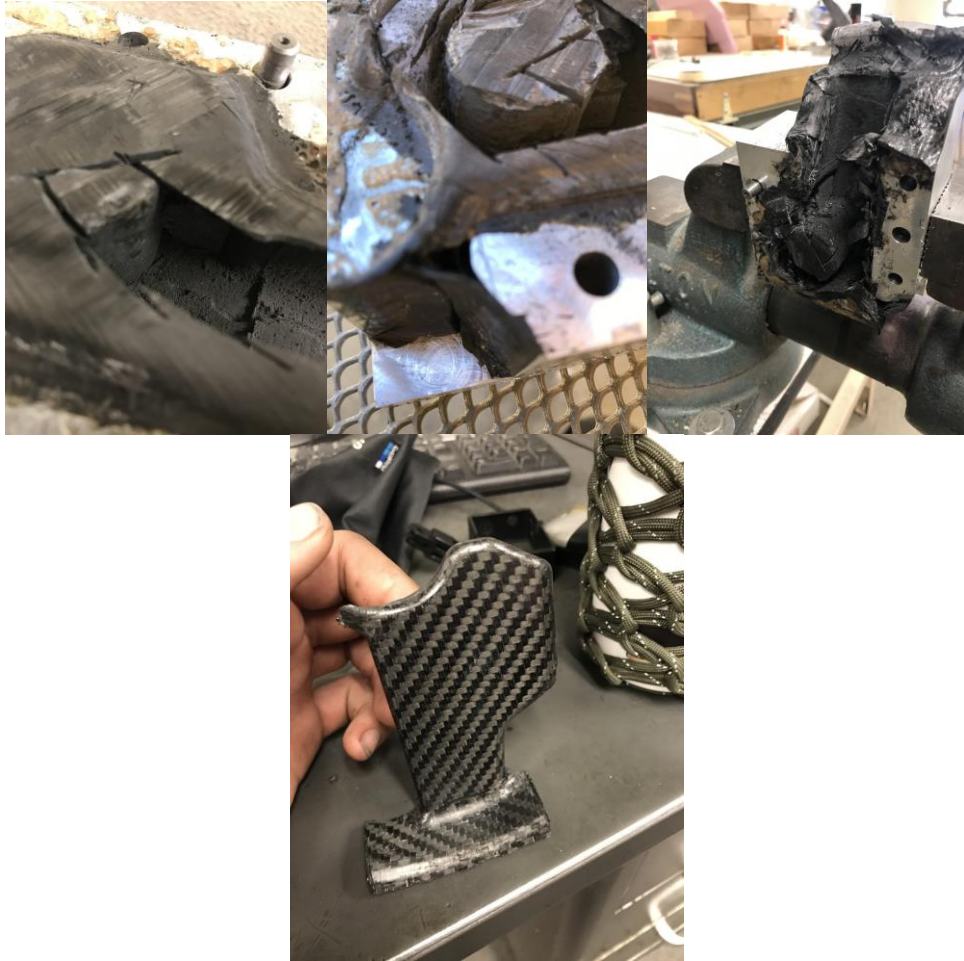
APPENDIX D: MANUFACTURING TRIAL PHOTOS

D.1 First Trial



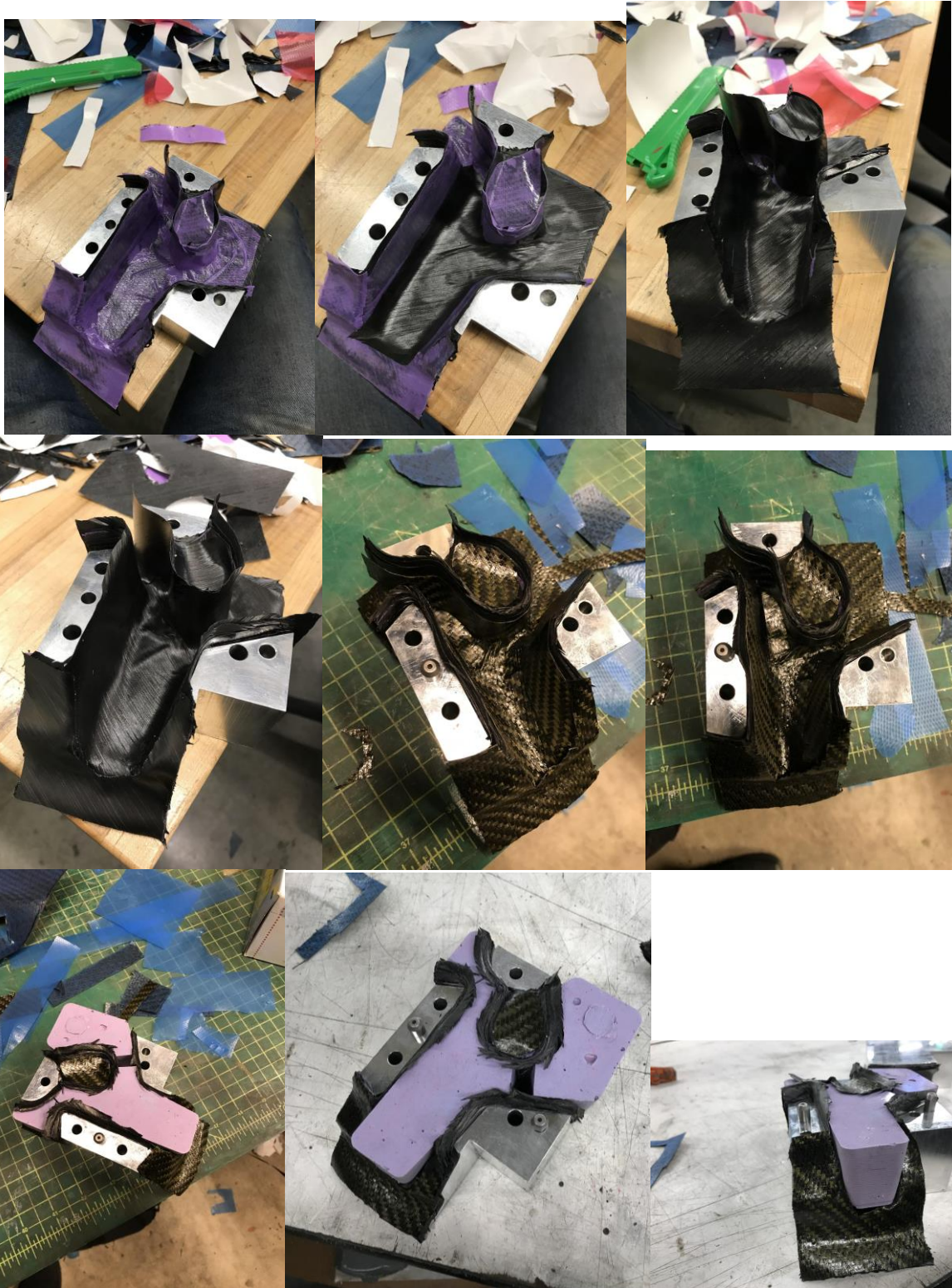


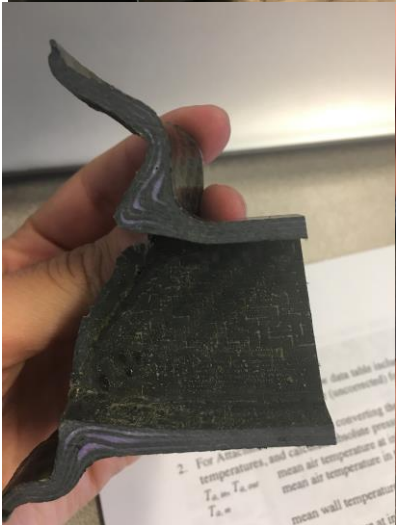




D.2 Second Trial







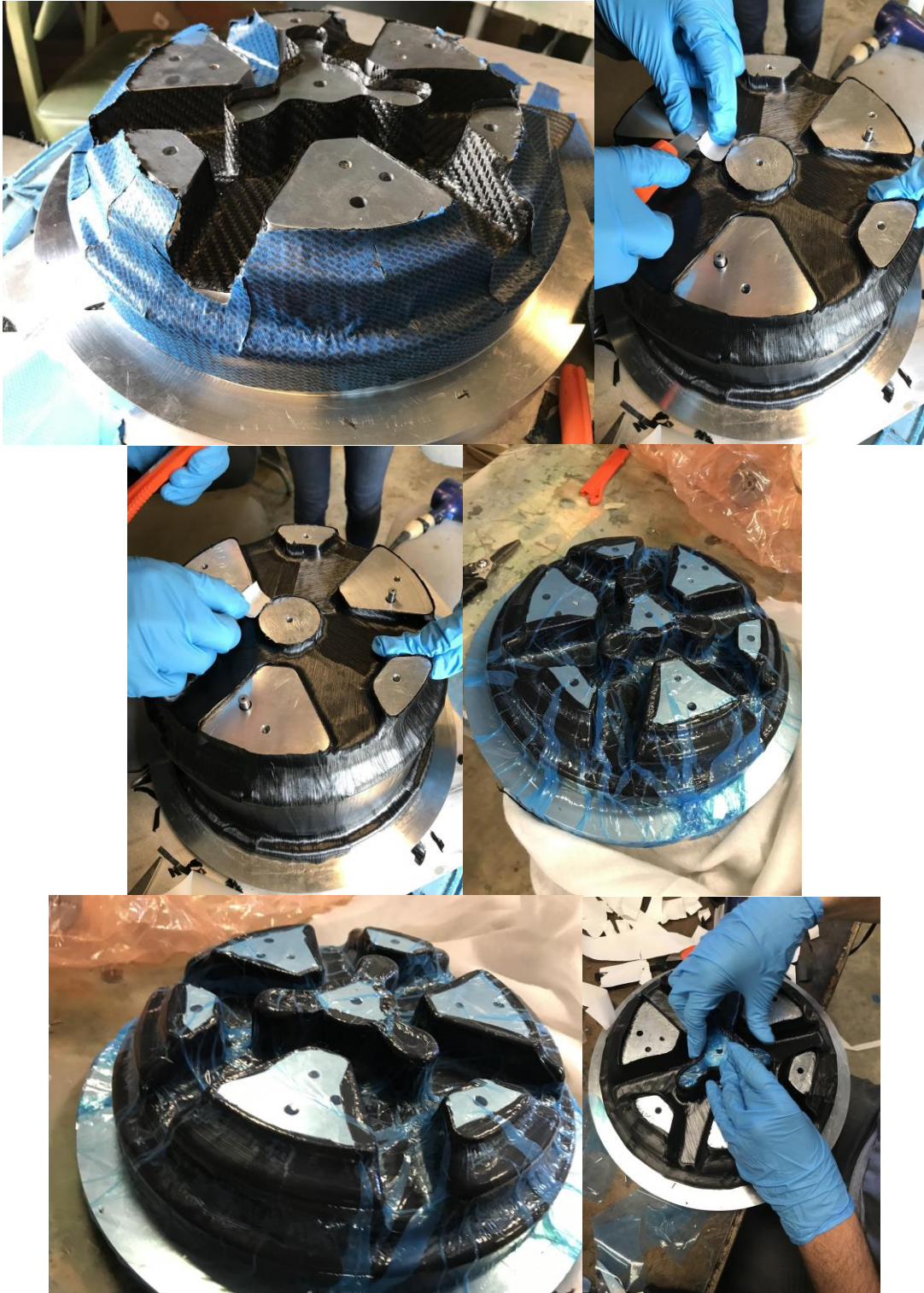
D.3 Mold Machining





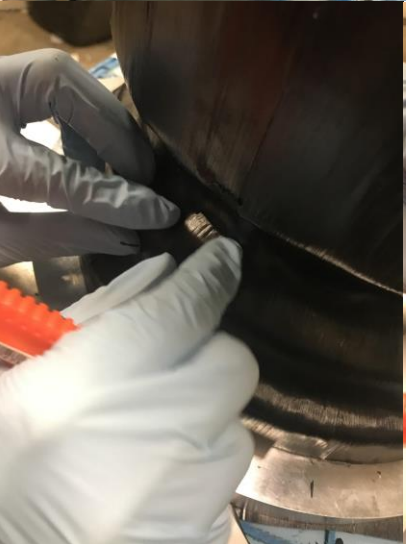
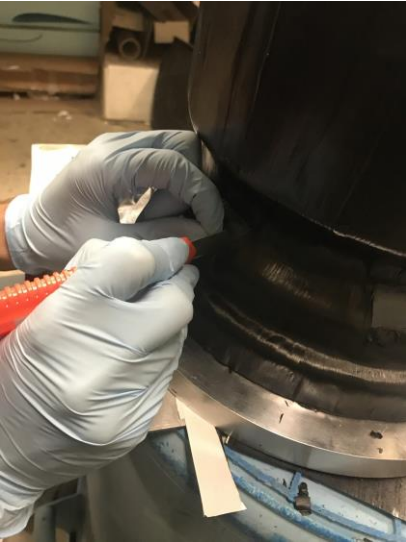
D.4 Wheel Lamination



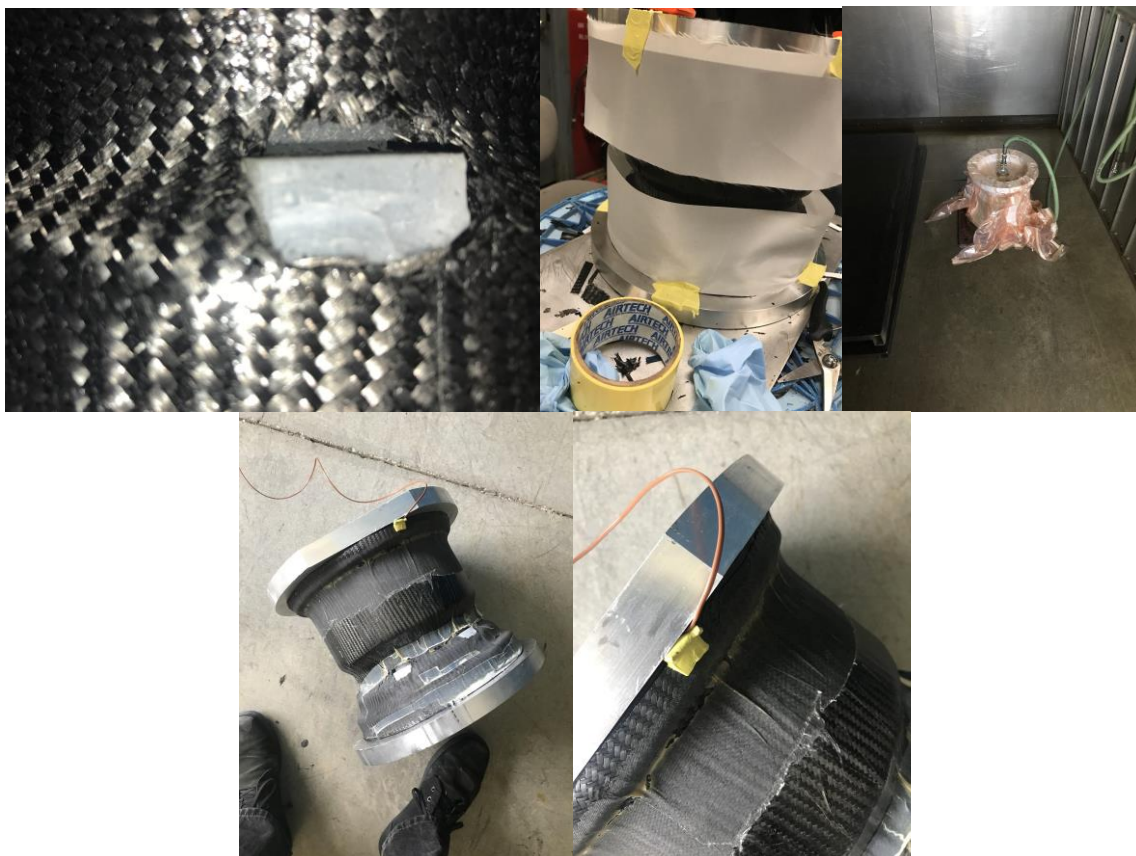












APPENDIX E: WORKS CITED

1. Caprarella, Claudio, et al. *Carbon Fiber Wheel*. California State University Northridge, 2013, pp. 1–28, *Carbon Fiber Wheel*.
2. Ressa, Aaron. *Development of a Carbon Fiber Wheel Rim*. Ohio State University, 2013, pp. 1–43, *Development of a Carbon Fiber Wheel Rim*.
3. Walther, Hans. *Development of Lightweight Laminated Composite Wheel for Formula SAE Race Vehicles*. University of Kansas, 2016, pp. 1–121, *Development of Lightweight Laminated Composite Wheel for Formula SAE Race Vehicles*.
4. TC-250 Epoxy Resin System; TenCate Advanced Composites: Morgan Hill, CA. https://www.tencatecomposites.com/media/486fa8ce-84e3-456e-a128-47208cab070d/b-vEPQ/TenCate%20Advanced%20Composites/Documents/Product%20datasheets/Thermoset/UD%20tapes%20and%20prepregs/TC250_Epoxy_PDS.pdf
5. Two-piece carbon fiber automotive wheels; Corvus Aerospace. Block A, No. 38 Beiguandu Road Wuzhong District, Suzhou, Jiangsu Province, China. <http://www.corvus-china.com/content-30-22-1.html>
6. Eiman, Ford, et al. *Carbon Fiber Monocoque Chassis for Formula SAE and Formula SAE Electric Race Cars*. California Polytechnic State University San Luis Obispo, 2017, pp. 1–259, *Carbon Fiber Monocoque Chassis for Formula SAE and Formula SAE Electric Race Cars*.